

UCLA

UCLA Electronic Theses and Dissertations

Title

Chemical Exchange Saturation Transfer (CEST): A Metabolic Imaging Technique Using Magnetic Resonance Imaging (MRI)

Permalink

<https://escholarship.org/uc/item/1j650674>

Author

Zhou, Zhengwei

Publication Date

2017

Peer reviewed|Thesis/dissertation

UNIVERSITY OF CALIFORNIA

Los Angeles

Chemical Exchange Saturation Transfer (CEST): A Metabolic Imaging Technique Using
Magnetic Resonance Imaging (MRI)

A dissertation submitted in partial satisfaction
of the requirements for the degree Doctor of Philosophy
in Bioengineering

by

Zhengwei Zhou

2017

© Copyright by

Zhengwei Zhou

2017

ABSTRACT OF THE DISSERTATION

Chemical Exchange Saturation Transfer (CEST): A Metabolic Imaging Technique Using Magnetic Resonance Imaging (MRI)

by

Zhengwei Zhou

Doctor of Philosophy in Bioengineering

University of California, Los Angeles, 2017

Professor Debiao Li, Chair

Chemical exchange saturation transfer (CEST) is an emerging MR imaging technique that is sensitive to the metabolite accumulation/loss. This technique selectively saturates the exchangeable protons in certain molecules. After exchange with water protons, the saturation can be detected by the change of water signal. Even though CEST imaging has shown great potential in some applications, it has not been utilized clinically due to practical issues related to imaging speed and reliability. The primary focus of the work in this dissertation is to make the current CEST techniques clinically translatable and address the challenges for cardiac and lumbar spine applications.

CEST imaging has been applied in the heart for creatine mapping because cardiac dysfunction was linked to loss of metabolites in the creatine kinase system. However, current limitations include: (a) long scan time, (b) residual cardiac and respiratory motion, and (c) B_0 field variations induced by respiratory motion. An optimized CEST technique was developed to address these problems. These challenges were addressed with the following improvements: (a) Images were acquired by single-shot FLASH, significantly increasing the scan efficiency. (b) All

images were registered to reduce the residual motion. (c) The acquired Z-spectrum was analyzed using 3-pool-model Lorentzian-line fitting to generate CEST signal, reducing the impact of B_0 field shifting due to respiratory motion. Validation studies were performed in chronic myocardial infarction animal model using late gadolinium enhancement as reference. It is shown that the infarct region has lower CEST signal compared to remote myocardium. Spatially, the hypointense regions in the CEST contrast maps closely match the bright areas in the LGE images. In addition, an improved cardiac CEST technique with dual-echo readout was proposed to further address the B_0 field variation issue. These data combined together suggest that cardiac CEST technique has the potential to provide information on metabolic abnormalities for cardiac diseases.

Intervertebral disc (IVD) degeneration is one of the leading causes of chronic low back pain. Current imaging modalities of the spine provide anatomical information, but are unable to differentiate non-painful from painful IVDs. Previous studies associated low pH as the leading cause of discogenic low back pain in degenerate IVDs. We proposed a quantitative CEST (qCEST) imaging protocol for pH assessment in the IVD. This technique was applied in animal model with induced disc degeneration. It is shown that the exchange rate measured from qCEST technique is correlated with the direct pH measurement using tissue pH-meter. In addition, gene analysis of harvested degenerated IVDs revealed strong positive correlation between up-regulation of pain markers and increase in qCEST signal. Collectively, these findings demonstrate that this approach can be used to measure pH in vivo within the IVD and has the potential to be used as a novel non-invasive method for the diagnosis of discogenic pain.

CEST fingerprinting framework was proposed to further improve CEST quantification. This is inspired by the magnetic resonance fingerprinting concept where the signal generated using randomized sequence parameters will be matched directly to a pre-defined dictionary instead of using a repeated, serial acquisition of data to fit to a particular equation. CEST fingerprinting utilizes CEST saturation with varying saturation power B_1 amplitude and saturation

time to create uniqueness of signal evolution for different exchange rates. Phantom studies demonstrated that CEST fingerprinting was more efficient (5x faster) compared to pulsed qCEST because there is no need for long saturation time and long TR. It is also shown that the proposed CEST fingerprinting technique can quantify exchange rate more accurately in the presence of MT effects.

In summary, with the technical improvements proposed in this dissertation, CEST imaging can be performed more efficiently and more accurately. These techniques can be potentially translated into clinical studies.

The dissertation of Zhengwei Zhou is approved.

Benjamin M. Ellingson

Daniel B. Ennis

Albert M. Thomas

Debiao Li, Committee Chair

University of California, Los Angeles

2017

Table of Contents

ABSTRACT OF THE DISSERTATION	ii
LIST OF ABBREVIATIONS	xii
LIST OF FIGURES	xv
LIST of TABLES	xviii
ACKNOWLEDGEMENTS	xix
VITA	xxi
CHAPTER 1: Introduction	1
1.1 Chemical Exchange Saturation Transfer (CEST)	1
1.2 CEST and Current Applications	3
1.2.1 Glucosaminoglycans (GAG)	4
1.2.2 Creatine	4
1.2.3 Mobile Proteins and Peptides	5
1.2.4 Glucose	6
1.2.5 X-ray Iodinated Agents	6
1.2.6 Reporter Genes	7
1.3 Current MR Metabolic Techniques	7
1.3.1 ¹ H Magnetic Resonance Spectroscopy	7
1.3.2 ³¹ P Magnetic Resonance Spectroscopy	8
1.3.3 Hyperpolarized ¹³ C	9
1.4 CEST: Advantages and Challenges	11

1.4.1 Advantages	11
1.4.2 Challenges	12
1.5 Aims	13
Aim 1: To develop a clinical translatable cardiac CEST technique for myocardial metabolic activity assessment.	14
Aim 2: To develop a quantitative CEST (qCEST) imaging protocol of intervertebral disc for pH assessment and evaluate its applicability for diagnosis of discogenic pain.	14
Aim 3: To develop CEST-fingerprinting technique for more efficient and more accurate CEST quantification.....	15
CHAPTER 2: Optimized Cardiac CEST MRI for Assessment of Metabolic Activity in the Heart	16
2.1 Significance.....	16
2.2 Background	16
2.3 Methods	18
2.3.1 Animal Preparation	18
2.3.2 MRI Protocol.....	18
2.3.3 Image Analysis	20
2.4 Results	21
2.5 Discussion.....	22
2.6 Conclusion	25
CHAPTER 3: Cardiac CEST MRI with Dual-Echo Readout for B0 Correction: A Repeatability Study.....	26

3.1 Background	26
3.2 Method	26
3.2.1 Sequence Diagram	26
3.3.2 Image Processing	27
3.2.3 MRI Protocol	27
3.3.4 Data Analysis	28
3.3 Results	29
3.4 Discussion	30
3.5 Conclusion	32
CHAPTER 4: Quantitative Chemical Exchange Saturation Transfer (qCEST) MRI of Intervertebral Disc in a Porcine Model	33
4.1 Significance	33
4.2 Background	34
4.3 Theory	35
4.4 Method	36
4.4.1 Phantom Preparation	36
4.4.2 In vitro MRI Experiments	37
4.4.3 Animal Preparation	37
4.4.4 In vivo MRI Experiments	38
4.4.5 Data Analysis	39
4.5 Results	39
4.5.1 Phantom	39

4.5.2 Animal Studies.....	40
4.6 Discussion.....	43
4.7 Conclusions.....	45
CHAPTER 5: Detection of Low Back Pain Using Novel MRI-Based Biomarker in a Porcine Model of Disc Degeneration	47
5.1 Background.....	47
5.2 Method.....	48
5.2.1 Study Design	48
5.2.2 IVD Degeneration Animal Model.....	49
5.2.3 In vivo MRI	50
5.2.4 IVD pH Measurement	51
5.2.5 Gene Expression Analysis	51
5.2.6 Histological Analysis and Immunofluorescence Imaging.....	52
5.2.7 Statistical Analysis.....	54
5.3 Results	54
5.3.1 Induction of IVD Degeneration.....	54
5.3.2 MR Signal Correlates with Intra-Discal pH in Degenerated IVDs	55
5.3.3 MR Signal Correlates with Pain-Markers in Degenerated IVDs.....	56
5.4 Discussion.....	57
CHAPTER 6: CEST-Fingerprinting: Towards Full Quantification of Exchange Rate in the Presence of Magnetization Transfer Effects	62
6.1 Background.....	62

6.2 Method	64
6.2.1 Pulse Sequence Design	64
6.2.2 Dictionary	65
6.2.3 MT Correction.....	66
6.2.4 Signal Matching	67
6.2.5 Phantom Preparation.....	68
6.2.6 MRI Acquisition.....	69
6.2.7 Data Analysis.....	70
6.3 Result.....	70
6.4 Discussion.....	73
6.4.1 CEST Fingerprinting	73
6.4.2 MT Correction.....	74
6.4.3 Potential Impacts	75
6.4.4 Moving to in vivo Studies	75
6.5 Conclusions.....	76
CHAPTER 7: Conclusions and Future Work	77
7.1 Summary of the Work.....	77
7.1.1 Cardiac CEST.....	77
7.1.2 pH Assessment in the IVD	77
7.1.3 CEST Fingerprinting	78
7.2 Future Directions	79

7.2.1 Scan Time Reduction	79
7.2.2 Clinical Validations	79
Reference	81

LIST OF ABBREVIATIONS

General

FDA	food and drug administration
IACUC	institutional animal care and use committee
CT	computerized tomography

Medicine

GAG	Glucosaminoglycans
BBB	brain-blood barrier
ATP	adenosine triphosphate
ADP	adenosine diphosphate
Cr	creatine
PCr	phosphocreatine
CK	creatine kinase
NAA	N-Acetylaspartic acid
GABA	gamma-Aminobutyric acid
MI	myocardial infarction
CVD	cardiovascular disease
IVD	intervertebral disc
PBS	phosphate buffer solution
RNA	ribonucleic acid
BDKRB1	bradykinin receptor B1
CGRP	calcitonin gene-related peptide
COMT	catechol-O-methyltransferase
BDNF	brain-derived neurotrophic factor

NGF	nerve growth factor
ASIC	acid sensing ion channel

Magnetic Resonance Imaging

MRI	magnetic resonance imaging
MRS	magnetic resonance spectroscopy
EPI	echo planar imaging
FLASH	fast low angle shot
TSE	turbo spin echo
MIRT	medical imaging registration toolbox
2D	two-dimensional
3D	three-dimensional
RF	radiofrequency
TR	repetition time
TE	echo time
TI	inversion time
FOV	field-of-view
rFOV	reduced field-of-view
ROI	region of interest
MRSI	magnetic resonance spectroscopy imaging
SNR	signal to noise ratio
LGE	late gadolinium enhancement
bSSFP	balanced steady-state free precession
MRF	magnetic resonance fingerprinting

Chemical Exchange Saturation Transfer

CEST	chemical exchange saturation transfer
------	---------------------------------------

DS	direct saturation
MT	magnetization transfer
cw	continuous-wave
APT	amide proton transfer
NOE	nuclear Overhauser enhancement
DGE	dynamic glucose enhancement
DCE	dynamic contrast enhancement
Qcest	quantitative chemical exchange saturation tra
WASSR	water saturation shift referencing
TSL	spin lock time
QUEST	quantifying exchange rates using saturation time dependencies
QUESP	quantifying exchange rates using saturation power dependencies
BM	Bloch-McConnell
CESL	chemical exchange sensitive spin-lock
bSSFPX	balanced steady-state free precession chemical exchange

LIST OF FIGURES

Figure 1.1 Principles of chemical exchange saturation transfer (CEST). (a) Equilibrium state of solute pool and water pool. (b) Solute protons are saturated after frequency selective saturation pulses. (c) After the chemical exchange, some of the saturated solute protons are transferred into water pool, causing water signal loss.	2
Figure 1.2 Measurement approach for CEST imaging.....	3
Figure 2.1 Pulse sequence diagram of the optimized cardiac CEST imaging technique.....	19
Figure 2.2 Z-spectrum of (a) scar region and (b) healthy myocardium. By using the 3-pool-model fitting, Z-spectrum (black) was separated into CEST curve (pink), MT curve (blue) and DWS curve (green). The center of DWS curve represents the resonant water frequency (B_0 field). The peak of CEST curve was defined as the CEST signal. It is clear that the healthy myocardium has higher CEST signal than scar, which suggests more Cr distribution in the healthy myocardium.....	21
Figure 2.3 (a) CEST maps and (b) corresponding LGE images of one representative subject in three slice locations. The hypointense regions (arrows) in the CEST maps match the LGE positive regions (arrows).	22
Figure 2.4 CEST signal in the scar (0.09 ± 0.04) is significantly reduced compared to healthy remote myocardium (0.16 ± 0.03), $p < 0.0001$	23
Figure 3.1 Sequence diagram of proposed cardiac CEST technique with dual-echo readout. ...	27
Figure 3.2 Image processing workflow of the proposed cardiac CEST dual-echo method.....	28
Figure 3.3 Representative images of proposed cardiac CEST method with dual-echo readout. (a-d) CEST-weighted images acquired at different saturation frequency offsets. (e) CEST contrast map. (f) B_0 map.	30
Figure 3.4 Bland-Altman plots of CEST signal for previous and proposed cardiac CEST methods. (a) Average CEST signal of the entire myocardium. (b) Average CEST signal in the lateral segment. (c) Average CEST signal in the septal segment. The dashed lines represent 95% limits of agreement.....	31
Figure 4.1 Ω -plots analysis of (a) phantoms with the same concentration (60 mM) but varying pH values (5.8, 6.1, 6.4, 6.7 and 7.0); (b) phantoms with the same pH value (7.0) but varying GAG concentration (20 mM, 40 mM, 60 mM, 80 mM and 100 mM).....	40

Figure 4.2 Quantitative results of the phantom study. (a) Pixel-wise mapping of labile proton exchange rate. (b) Pixel-wise mapping of labile proton ratio. (c) The chemical exchange rate as a function of pH. (d) The labile proton ratio as a function of GAG concentration. The error bars in (c) and (d) represent the standard deviation of all the pixels within the ROI of each tube for k_{sw} and f_r , respectively.	41
Figure 4.3 Representative images of IVDs and corresponding exchange rate maps in one mini-pig. (a) T2-weighted image in the sagittal plane. (b) Axial anatomical images of corresponding IVDs. (c) Exchange rate maps of corresponding IVDs. The IVDs with lower pH tend to have higher exchange rate.	42
Figure 4.4 (a) Ω -plots analysis of representative IVDs with varying pH values (5.0, 5.8 and 6.7). (b) The chemical exchange rate as a function of pH in the animal studies.	43
Figure 5.1 IVD degeneration timeline. Minipigs underwent annular injury in four IVD levels to induce degeneration (denoted by red color). Following degeneration, animals were randomly divided into 3 groups and scanned at 2, 6 and 10 weeks. At each time point, one of the groups was sacrificed and the pH within the injured IVDs was measured. The IVDs were harvested for gene analyses and histology.	49
Figure 5.2 IVD degeneration following intra-discal puncture.	53
Figure 5.3 pH and qCEST changes following IVD degeneration. (A) Correlation between the qCEST signal represented by the exchange rate between solute pool and water pool (k_{sw}) and the pH measured within the IVD following animal sacrifice. (B) ROC curve analysis of qCEST signaling for the detection of degenerating IVDs. (C) pH and (D) qCEST measurements within the degenerating IVDs at 2, 6 and 10 weeks after degeneration. (n=12 per experimental group; *p < 0.05, **p < 0.01, ****p = 0.0001; qCEST= quantitative chemical exchange saturation transfer).	55
Figure 5.4 Pain and inflammatory markers upregulation in degenerating IVDs. Quantitative RT-PCR analysis of (A-C) pain-related genes (CGRP, BDKRB1 and COMT), (D) IL-6 and (E) BDNF harvested from the annulus fibrosus and nucleus pulposus of degenerated IVDs at 2, 6 and 10 weeks after induction of degeneration.	56
Figure 5.5 Linear correlation between qCEST and biomarkers in degenerating IVDs. Correlation curves between qCEST signal and corresponding expression of (A) CGRP, (B) BDKRB1, (C) COMT, (D) IL-6 and (E) BDNF extracted from degenerated and healthy IVDs.	58
Figure 6.1 CEST fingerprinting sequence pattern. (a) Acquisition sequence diagram. In each subsequent acquisition block, RF irradiation power B_1 and duration of the CEST preparation	

module are varied in a pseudorandom pattern. (b, c) Examples of average RF irradiation power B1 and CEST saturation used in this study.65

Figure 6.2 Framework of MT correction. (a) Reference dictionary (solid) and reference signal (dashed) are different in presence of MT effects. (b) MT effects can be quantified comparing the reference dictionary and reference signal. (c) Dictionary is generated by simulating 2-pool Bloch-McConnell equations. (d) Corrected dictionary can be generated by adding (b) MT effects to (c) dictionary.67

Figure 6.3 Signal properties and matching results from phantom study. (a) Simulated CEST signal with different exchange rates. (b) Measured CEST signal and the corresponding dictionary match.....70

Figure 6.4 Exchange rate maps of the phantom studies.....72

Figure 6.5 Chemical exchange rate as a function of pH. The error bars represent standard deviation of the exchange rate within the ROI of each tube. The dark gray dashed line represents the fitted curve of exchange rate as a function of pH. This was compared with the exchange rates reported by Goerke et al. at 20°C shown in red dashed line (166).73

LIST of TABLES

Table 3.1	Imaging parameters for the previous and proposed cardiac CEST methods	29
Table 6.1	Composition of the Three Phantom Groups	68

ACKNOWLEDGEMENTS

I feel fortunate and grateful to have Dr. Debiao Li as my PhD advisor and mentor and I would like to thank him for his overall guidance throughout my PhD training. He has provided me with flexible and resourceful research environment at the Biomedical Imaging Research Institute (BIRI) at Cedars-Sinai Medical Center. He is always helpful and encouraging when I encounter difficulties. Not only does Dr. Li guide me on the research projects, he also shares with me his vision on bigger picture, like how to build a successful career, or the general trend in MRI field. His conversation is always inspiring and enlightening, and will surely benefit my career even after I graduated.

In addition, I would like to extend my appreciation to my thesis committee, Professor Daniel Ennis, Professor Albert Thomas, Professor Benjamin Ellingson for their help and advice whenever I sought it.

My sincerest thanks to the entire Biomedical Imaging Research Institute including but not limited to my fellow graduate students (David Chen, Yuhua Chen, Zixin Deng, Dr. Avinash Kai, Qi Liu, Sen Ma, Christopher Nguyen, Jianing Pang, Jaime Shaw, Nan Wang, Yibin Xie, and Randy Yang), faculty (Rohan Dharmakumar, Zhaoyang Fan, Wei Gao, Hui Han, Behzad Sharif, Feng Shi, Shawn Wagner, and Yi Zhang), and supporting staff (Eileen Da Vido, Ed Gill, Johanna Kim, Hernan Rios, Laura Smith and Richard Tang). In particular I want to acknowledge Dr. Qi Liu whose work set up the foundation of my CEST work, and Dr. Behzad Sharif, who guided me through my early PhD training.

I am grateful for the invaluable support and expertise provided by Siemens team members including Drs. Gerhard Laub, Xiaoming Bi and Yutaka Natsuaki. I benefited greatly from their expertise on MR physics and sequence programming.

I also want to thank my collaborators from the Heart Institute (Eduardo Marbán) and the Spine Institute (Maxim Bez, Dan Gazit, Gadi Pelled, Dmitriy Sheyn, and Wafa Tawackoli) at

Cedars-Sinai Medical Center. Their work provided a validation tool for my new techniques and these techniques can in turn help them further study the pathophysiology of the disease. I'm grateful to work with them to facilitate the clinical application of the innovations in the dissertation.

I gratefully acknowledge the Seed Grant support from the Society of Cardiac Magnetic Resonance.

Lastly, I would like to thank my parents Yonghua Zhou and Hongping Xu for supporting me spiritually throughout my PhD and my life in general. Most importantly, I'd like to thank my boyfriend Yan Zhang, whose love and accompany during my PhD is so appreciated.

VITA

EDUCATION

- MS, Bioengineering, University of California, Los Angeles (2014)
- BS, Biomedical Engineering, Tsinghua University (2012)

EXPERIENCE

- Graduate Student Researcher, Li Group, Biomedical Imaging Research Institute, Cedar-Sinai Medical Center, Los Angeles, CA (2012-Current)
- Undergraduate Research Assistant, Ying Group, Center for Biomedical Imaging Research, Tsinghua University, Beijing, China (2011-2012)
- Summer Undergraduate Research Assistant, Atkin Group, Department of Psychiatry and Behavioral Sciences, Stanford University, Palo Alto, CA, (2011)

PUBLICATIONS

- **Zhou, Z.**, Han, P., Zhou, B., Christodoulou, A., Deng, Z., Shaw, J., and Li, D. CEST fingerprinting for exchange rate quantification in the presence of magnetization transfer effects. *Magnetic Resonance in Medicine*. In submission.
- Bez, M[†], **Zhou, Z[†]**, Sheyn, D., Tawackoli, W., Giaconi, J., Shapiro, G., David, S., Gazit, Z., Pelled, G., Li, D. and Gazit, D., 2017. Detection of low back pain using novel MRI-based biomarker in a pig model of disc degeneration. *Science Translational Medicine*. In preparation.
- Deng, Z[†], Lee, S[†], Xie, Y., Fan, Z., Nguyen, C., Bi, X., **Zhou, Z.**, Shaw, J., Yang, Q., Choi, B., Kim, J., Berman, D., Li, D. and Chang, H., 2017. Noninvasive functional evaluation of coronary stenosis using MR instantaneous wave-free ratio (MR-IFR): initial patient study. *JACC: Cardiovascular Imaging*. In submission.
- **Zhou, Z.**, Nguyen, C., Chen, Y., Shaw, J., Deng, Z., Xie, Y., Dawkins, J., Marban, E., and Li, D., 2017. Optimized cardiac CEST MRI for assessment of metabolic activity in the heart. *Journal of Cardiovascular Magnetic Resonance*. In revision.
- **Zhou, Z[†]**, Bez, M[†], Tawackoli, W., Giaconi, J., Sheyn, D., de Mel, S., Maya, M.M., Pressman, B.D., Gazit, Z., Pelled, G., Gazit, D. and Li, D., 2016. Quantitative chemical exchange saturation transfer MRI of intervertebral disc in a porcine model. *Magnetic Resonance in Medicine*, 76(6), pp.1677-1683.

- **Zhou, Z.**, Bi, X., Wei, J., Yang, H.J., Dharmakumar, R., Arsanjani, R., Merz, B., Noel, C., Li, D. and Sharif, B., 2016. First-pass myocardial perfusion MRI with reduced subendocardial dark-rim artifact using optimized Cartesian sampling. *Journal of Magnetic Resonance Imaging*.
- Chen, A.C., Oathes, D.J., Chang, C., Bradley, T., **Zhou, Z.**, Williams, L.M., Glover, G.H., Deisseroth, K. and Etkin, A., 2013. Causal interactions between fronto-parietal central executive and default-mode networks in humans. *Proceedings of the National Academy of Sciences*, 110(49), pp.19944-19949.

SELECTED CONFERENCE PROCEEDINGS

- **Zhou, Z.** (2017, April). CEST Fingerprinting: A Novel Approach for Exchange Rate Quantification. Oral presentation at: 25th ISMRM; Honolulu, USA.
- **Zhou, Z.** (2017, April). pH Measurement of Intervertebral Disc in the Process of Disc Degeneration Using Quantitative Chemical Exchange Saturation Transfer (qCEST). Oral presentation at: 25th ISMRM; Honolulu, USA.
- **Zhou, Z.** (2017, January). Cardiac CEST MRI with Dual-Echo Readout for B₀ Correction: A Preliminary Reproducibility Study for Assessment of Metabolic Activity in the Heart. Oral presentation at: 20th SCMR; Washington D.C., USA.
- **Zhou, Z.** (2016, May). Optimized Cardiac CEST MRI for Assessment of Metabolic Activity in the Heart. Oral presentation at: 24th ISMRM; Singapore.

AWARDS

- International Society of Magnetic Resonance in Medicine (ISMRM) Summa Cum Laude Award (2017).
- Seed Grant Award, Society of Cardiac Magnetic Resonance (SCMR) (2016).

PATENT

- Gazit, D., Li, D., Pelled, G., Gazit, Z., Zhou, Z. 2016. Non-invasive pH-dependent imaging using quantitative chemical exchange saturation transfer (qCEST). U.S. Patent Application 62/347,509, filed June 8, 2016. Patent Pending.

CHAPTER 1: Introduction

1.1 Chemical Exchange Saturation Transfer (CEST)

Chemical exchange saturation transfer (CEST) is an emerging metabolic imaging technique using magnetic resonance imaging (MRI) (1,2). This method has been applied in different organs for various purposes (3).

The underlying principles of CEST are illustrated in Fig. 1.1. The existence of solute protons that resonate at a different frequency from water protons can be indirectly detected if the solute protons have a reasonable chemical exchange rate with water protons. The solute protons can be saturated using frequency selective saturation pulses. Some of these saturated protons will be transferred into water pool, causing water signal loss. The amount of the water signal loss normally indicates the solute proton concentration and the exchange rate.

The measurement approach of CEST imaging is to acquire images with different saturation frequency offsets across the spectrum (Fig. 1.2). Z-spectrum was generated by combining these images together after normalization using an image acquired without any saturation pulses.

In general, CEST imaging sequences consist of two parts, CEST preparation module and readout module. CEST preparation module is where the saturation pulses are applied to indirectly lead to water signal loss. On small animal scanners, a rectangular pulse with constant B_1 amplitude is normally used. This is the most simple and efficient CEST saturation pulse. It is commonly known as continuous-wave (cw) saturation pulses. However, due to the hardware limits and SAR issues, these pulses

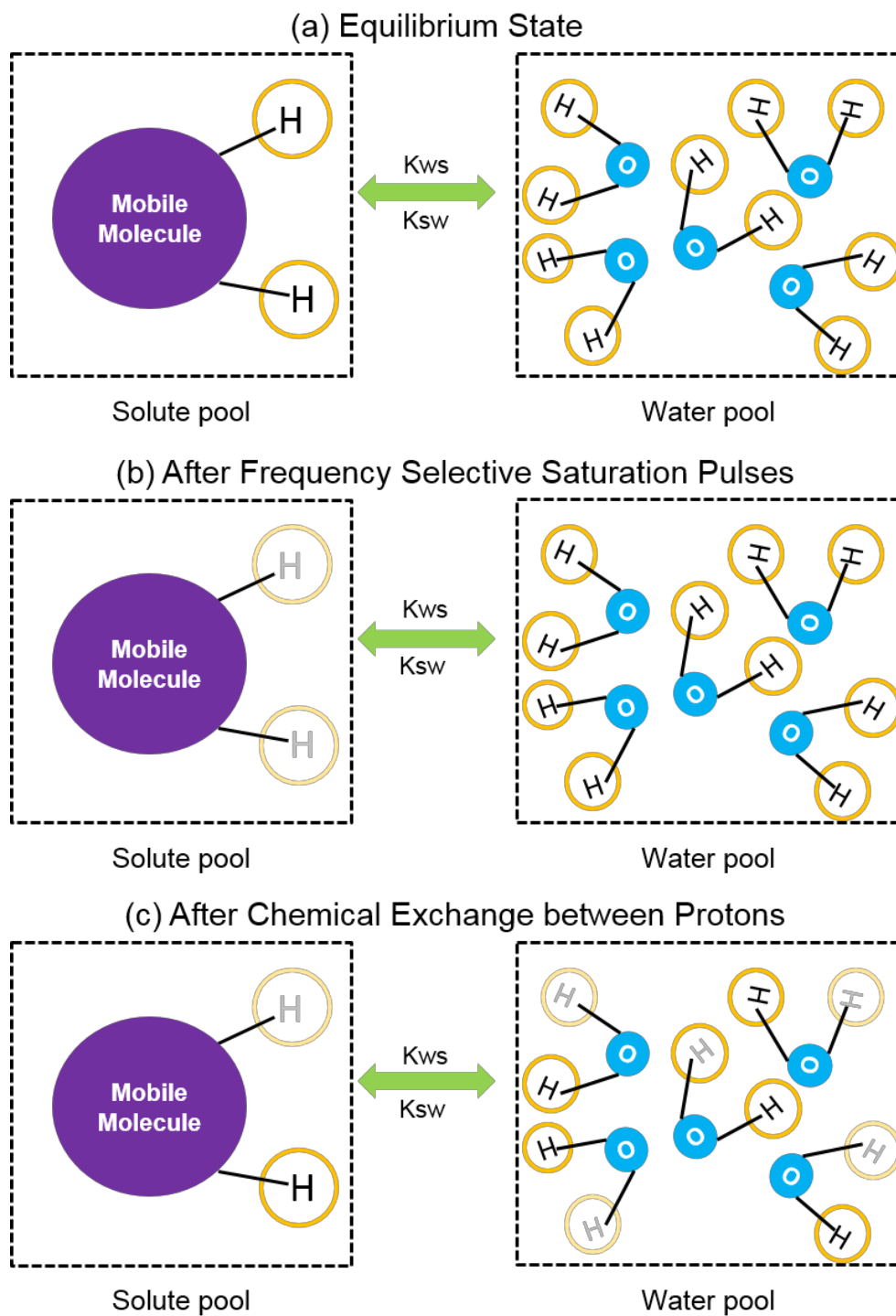


Figure 1.1 Principles of chemical exchange saturation transfer (CEST). (a) Equilibrium state of solute pool and water pool. (b) Solute protons are saturated after frequency selective saturation pulses. (c) After the chemical exchange, some of the saturated solute protons are transferred into water pool, causing water signal loss.

cannot be implemented on clinical scanners. Instead, Gaussian-shaped pulse trains are used to achieve similar saturation effects. Common readout for CEST sequences include FLASH, EPI and TSE. The readout is normally chosen for the balance of scan time and SNR.

CEST effect normally happens together with direct saturation (DS) effect, which is symmetric with respect to the resonant water frequency (assigned as 0 ppm for reference). In order to separate CEST effect from DS effect, asymmetry analysis was performed by subtracting the reference side ($-\Delta\omega$) and the label side ($+\Delta\omega$), in which $\Delta\omega$ is the resonant frequency of the solute protons.

$$\text{MTR}_{\text{asym}}(\Delta\omega) = S(-\Delta\omega)/S_0 - S(+\Delta\omega)/S_0$$

It should be noted that magnetization transfer (MT) is another common competing effect in CEST experiments. It will be discussed in the following chapters on how to minimize contamination from MT effects in CEST signal.

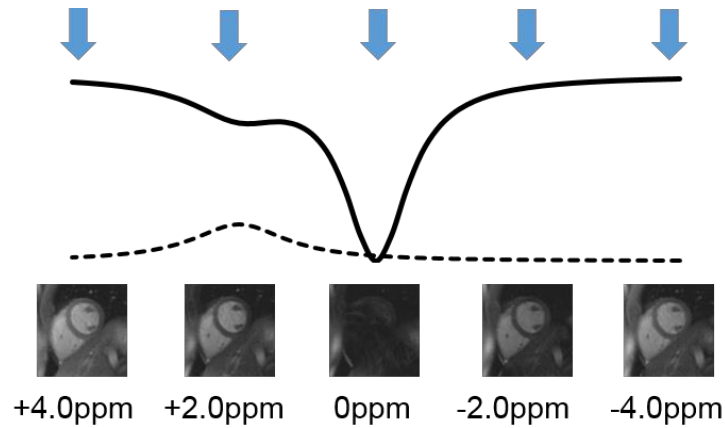


Figure 1.2 Measurement approach for CEST imaging.

1.2 CEST and Current Applications

CEST can detect many endogenous and exogenous agents. These CEST agents can provide powerful contrast for different applications. The CEST contrast is mostly affected by the solute proton concentration (determining how many saturated protons can be transferred into water pool) and the exchange rate (determining how fast the saturated protons can be transferred

into water pool), together with other minor contributing factors. Most CEST applications focus on detecting the CEST agent concentration change or the pH environment change, which can be indicated from the exchange rate.

In this section, we will discuss some endogenous and exogenous CEST agents and their applications.

1.2.1 Glucosaminoglycans (GAG)

GAG is a critical component in the intervertebral disc and cartilage. The labile hydroxyl protons (-OH) on GAG can be detected using CEST at +1.0 ppm. gagCEST allows the detection of GAG-deficiency in tissue, as is the case in osteoarthritis. This technique has been used in human knees (4,5) and spine (6,7). gagCEST can also be used to detect pH change in intervertebral disc to assess discogenic lower back pain (8,9).

1.2.2 Creatine

Creatine is one important substrate in the creatine kinase system. It is closely related to the ATP resynthesis process. The creatine level indicates the ATP activity level in the tissue. The amine protons (-NH₂) of creatine can be detected using CEST at +1.8 ppm. This technique has been applied in the calf to detect the creatine change during and after exercise (10,11). The dynamic change of creatine can be captured because the temporal resolution is up to 24 s and can be further improved with advanced fast imaging techniques. This technique has also been applied to the heart to detect myocardial metabolic abnormalities (12). However, this technique is still at early stage and further developments is still needed for clinical translation.

Because creatine has a moderate exchange rate with water, it is commonly used in pH-varied phantoms to validate new quantitative CEST methods.

1.2.3 Mobile Proteins and Peptides

One of the earliest CEST application is to detect the amide protons of mobile proteins and peptides. The resonant frequency of the amide protons is at +3.5 ppm. This technique is more commonly known as amide proton transfer (APT) (13).

APT imaging has been applied in cancer imaging because of the abnormal expression of mobile proteins in the tumor environment (14-17). Multiple studies have shown that APT imaging can differentiate between high grade and low grade tumors and provide unique information in therapy response (18-21).

APT imaging can also detect acute ischemic tissue acidosis. It has been shown that ATP contrast differs in normal region and ischemic region in animal models and stroke patients (22-25). However, it should be noted that APT contrast is complex with multiple experimental and physiological considerations.

In addition to the competition from DS effects and MT effects, APT signal may also be affected by fat signal (resonant frequency around +3.5 ppm) and nuclear Overhauser enhancement (NOE) effects (resonant frequency around -3.5 ppm). Therefore, fat suppression is an important component in APT scans to eliminate lipid artifacts (26). NOE effects are normally seen to create a negative background from Z-spectrum asymmetry analysis since NOE effects can't be easily eliminated. In a recent study, a new metric was proposed to separate APT signal from NOE signal (27).

APT, especially the application of brain tumor, is so far the most robust CEST technique. The current technique is ready for clinical translation. Patient studies are underway to validate the technique and demonstrate the potential clinical impact.

1.2.4 Glucose

Glucose is the primary energy source in most organs. Abnormalities in glucose uptake is associated with a range of pathological conditions. Comparing to other exogenous MRI agents, natural D-glucose is biodegradable. It has been FDA-approved for non-imaging purposes.

The labile hydroxyl protons (-OH) on glucose can be detected using CEST at +1.0 ppm. Initial studies used CEST to show the glucose enhancement before and after the infusion (28,29). In recent studies, the concept of dynamic glucose enhancement (DGE) was introduced, where CEST scans were performed repeatedly to track the dynamic change after D-glucose infusion (30,31). The signal change is caused by the glucose uptake and is related to the kinetics of delivery, transport and metabolism of D-glucose. One major difference between DGE and dynamic contrast enhancement (DCE) is that glucose can transport across blood-brain barrier (BBB) while Gadolinium-based contrast agent enhancement will be disrupted by BBB.

Glucose CEST is among the most eye-catching CEST applications because this technique is non-radioactive and the contrast agent is biodegradable. This technique is still in early stages of development, but technical improvements with optimized MRI acquisitions can be expected for clinical translation. It should be noted though, all current studies were performed on high-field scanners.

1.2.5 X-ray Iodinated Agents

While CEST can be used for pH imaging, it requires CEST agent to provide contrast in different pH environment. However, in some body parts, there is no endogenous CEST agent or the endogenous CEST agent can't provide enough signal.

Iodinated agents like Iopamidol, Iohexol and Ioversol and Iodixanol are routinely used as X-ray and CT agents in clinic. These agents contain amide protons and they can be detected using CEST (32). The resonant frequency of the amide protons in the iodinated agents are quite

far from the resonant water frequency, which means the CEST signal will not be as sensitive to DS effects as other endogenous CEST agents.

These iodinated agents demonstrate a very high safety profile. They can be potentially used for pH imaging (33) or serve as an alternative for MRI perfusion agents (34,35).

1.2.6 Reporter Genes

In molecular biology, a reporter gene is a gene that is attached to a sequence of gene of interest. The purpose of reporter genes is to indicate whether the gene of interest has been expressed properly. Generally, reporter gene expresses molecules that can be seen by imaging modalities like MRI. A type of MRI reporter gene expresses proteins that can be imaged using CEST (36-38). Compared to other MRI reporter genes, this type of reporter gene is biodegradable and nonmetallic, and it provides positive contrast instead of negative contrast.

1.3 Current MR Metabolic Techniques

The current MR metabolic techniques mostly include ^1H magnetic resonance spectroscopy (MRS), ^{31}P MRS and hyperpolarized ^{13}C MRS. Among different nuclei, ^1H MRS is most commonly used in clinical studies because hydrogen is main element in human body and ^1H MRS does not require additional hardware. ^{31}P MRS and hyperpolarized ^{13}C MRS can also detect some essential metabolites in the body. These techniques have shown promising results in clinical and preclinical studies. However, they are still limited by some technique challenges. Some limitations are common in all MRS techniques, such as low spatial resolution and long scan time, while some issues need to be addressed separately for different techniques. This will be discussed in detail in the following sections.

1.3.1 ^1H Magnetic Resonance Spectroscopy

^1H MRS is based on the fact that the protons of different metabolites have different resonant frequencies, which means they show as multiple peaks on the spectrum. In addition to

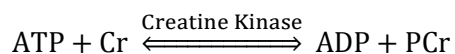
the spatial dimension, MRS has an additional spectral dimension, where protons with different resonant frequencies will be encoded (39). Common metabolites studied in ^1H MRS include choline, creatine, NAA, lactate, lipids, glutamine and glutamate.

The clinical interpretation of ^1H MRS is mainly based on checking the elevation or absence of certain metabolites. In tumor imaging, there is a wide list of metabolites elevated including NAA, choline, creatine, lipids, lactate and myoinositol. This information is routinely used in combination with perfusion and diffusion for tumor evaluation and treatment follow-up (39,40). ^1H MRS has also been applied to study the metabolic mechanisms of heart failure by quantifying the myocardial lipid accumulation and myocardial creatine level (41). Please note that in ^1H MRS studies, creatine refers to the total amount of creatine and phosphocreatine because the two substrates show as the same peak on the proton spectrum. ^1H MRS can also be used to detect the neurotransmitters glutamate and GABA. This is especially useful in studying psychiatric diseases (42,43) and Alzheimer's disease (44).

As mentioned before, MRS techniques are normally limited by low spatial resolution and long scan time, due to the additional spectral dimension. Advanced fast imaging techniques including parallel imaging and compressed sensing have been applied to accelerate the acquisition process. With these technical improvements, magnetic resonance spectroscopy imaging (MRSI) is now feasible and have been applied in some clinical studies. It has been recently shown that ^1H -MRSI with high spatial resolution and high SNR can be achieved in practical experiments with subspace-based spectroscopic imaging framework (45,46).

1.3.2 ^{31}P Magnetic Resonance Spectroscopy

^{31}P MRS can provide non-invasive measurements of phosphocreatine (PCr), ATP and ADP. These metabolites contain valuable information about cellular metabolism because they are important substrates of the creatine kinase (CK) system, an essential way for ATP regeneration.



CK system is the fastest way to regenerate ATP after exercise. When ATP is running out, PCr will be depleted to maintain ATP supply. When there is sufficient ATP supply, PCr serves as the reservoir of cellular energy.

Two major applications of ^{31}P MRS are skeletal muscle and myocardium. In skeletal muscle, ^{31}P MRS was performed before and after exercise to assess the metabolic capacity of skeletal muscle to support large mechanical work. More specifically, post-exercise recovery of PCr, ATP and ADP was measured to study the pathology of metabolic diseases (47). Multiple cardiovascular diseases have also been associated with metabolic impairment using ^{31}P MRS (48-51).

^{31}P MRS has more challenges compared to ^1H MRS. Due to the limited concentration of ^{31}P nuclei in the body, the sensitivity is a bigger issue for ^{31}P MRS techniques. When applying ^{31}P MRS to the heart, cardiac and respiratory motion needs to be addressed to avoid potential errors. The current techniques have long scan time and normally require experienced MR technicians because of the complicated protocol. In addition, non-proton MRS techniques require specially designed hardware. This equipment is fairly expensive and is only available in a few research sites. This greatly limits the clinical translation of ^{31}P MRS.

1.3.3 Hyperpolarized ^{13}C

While the sensitivity of endogenous C-nuclei is too low for imaging, the signal can be increased as much as 100,000 times by injecting hyperpolarized ^{13}C -labeled substrates(52). The fact that many important metabolic substrates including pyruvate and lactate can be labeled using hyperpolarized ^{13}C has attracted a lot of attention and opened the door for a new diagnostic platform. In addition, the hyperpolarized ^{13}C -nuclei can be transferred during the main steps of oxidative metabolism, and different substrates show as multiple peaks on the ^{13}C spectrum, which means it is possible to track the kinetics of the metabolic fates of labelled substrates (53).

Hyperpolarized ^{13}C has been applied in multiple preclinical studies for different purposes. In tumor imaging, by injecting $[1-^{13}\text{C}]$ pyruvate, pyruvate-lactate exchange can be measured. It has been shown that pyruvate-lactate exchange can be used to identify tumor grade and serve as an early response marker for treatment, particularly in oncology (53). In cardiac imaging, hyperpolarized ^{13}C , combined with $[1-^{13}\text{C}]$ and $[2-^{13}\text{C}]$ pyruvate, enables real time imaging of myocardial metabolism in vivo. This helps understanding of pyruvate downstream metabolic cycles in the normal and diseased heart (54). Hyperpolarized ^{13}C can also be used to provide intracellular pH measurement from the ratio of signal intensities of hyperpolarized bicarbonate ($\text{H}^{13}\text{CO}_3^-$) and $^{13}\text{CO}_2$ following intravenous injection of hyperpolarized $\text{H}^{13}\text{CO}_3^-$ (55).

Hyperpolarized ^{13}C has shown promising results in preclinical studies. However, it still poses technical challenges and practical issues to move into clinical studies. Similar as ^1H and ^{31}P , the additional spectral dimension imposes more challenges to reach the balance of spatial resolution, SNR and scan time. In addition to that, there is a natural decay of the hyperpolarized signal, and the longitudinal signal will not recover after the RF pulses of imaging sequences. This means the acquisition window needs to be finished within a restricted time window (normally a few minutes) (52). EPI or spiral trajectory, combined with parallel imaging and compressed sensing is used to perform efficient imaging of rapidly decaying ^{13}C -labeled substrates (56,57).

Currently, hyperpolarized ^{13}C is only available in a few research sites due to the complicated process of hyperpolarizing ^{13}C -labelled agents, transporting the agents and injecting the agents. This process needs to be done in a very efficient way because of the natural decay of hyperpolarized signal. Normally, one preclinical hyperpolarized ^{13}C experiment involves a group of experienced personnel to take care of the hyperpolarization, MRI acquisition and animal care. The hyperpolarization equipment is also very expensive, which adds another hurdle for the clinical translation of this technique.

1.4 CEST: Advantages and Challenges

1.4.1 Advantages

Compared to the MR metabolic techniques discussed above, CEST has the following advantages:

a) CEST can achieve high spatial resolution image in a more efficient way. The readout of CEST sequences is the same as conventional MRI sequences. There is no need to encode the spectral dimension like MRS techniques. Therefore, there is more flexibility in selecting the frequency range to be acquired. The practical CEST protocols only acquire images with the frequency offsets of interest rather than the entire spectrum. Since CEST is still a new technique relatively, the potential of accelerating CEST imaging has not been fully explored yet. With the recent technical developments on compressed sensing and low rank reconstruction, CEST acquisition can be further accelerated.

b) CEST has higher sensitivity compared to the MRS techniques. CEST signal is indirectly detected via water protons. Due to the natural redundancy of water protons in the body, CEST is expected to have enhanced sensitivity. This has been shown in studies comparing Cr CEST with ^1H and ^{31}P MRS (11,12).

c) Compared to MRS techniques, especially non-proton MRS techniques, it is easier for CEST imaging to be translated. Since CEST imaging is a proton-based imaging technique, there is no additional hardware requirement. In addition, the image acquisition part of CEST sequences is the same as conventional MRI sequences. It is not too difficult for the MR technicians to get used to CEST protocol, prescribe the correct spatial location and run the sequence.

d) CEST has an additional dimension of exchange rate to differentiate among multiple molecules. The chemical exchange between water protons and solute protons can be separated into three different categories based on the exchange rate k_{sw} and chemical shift $\Delta\omega$, fast exchange regime ($k_{sw} \gg \Delta\omega$), intermediate exchange regime and slow exchange regime ($k_{sw} \ll \Delta\omega$). Only protons that fall into the intermediate and slow exchange regime can be detected by

CEST imaging. When the exchange rate is too fast, the two protons start to merge as one peak on the Z-spectrum. However, if the exchange rate is too slow, the saturated solute protons can hardly be transferred into water pool and no water signal loss can be detected.

Here is an example of how exchange rate serve as additional dimension in CEST imaging. The amine protons ($-NH_2$) in Cr and PCr have the same chemical shift. That's why they show as one peak on the 1H MRS spectrum. However, only Cr protons have the moderate exchange rate with water. Therefore, Cr can be separated from PCr in CEST imaging. This allows CEST imaging to study the kinetics of Cr and PCr.

1.4.2 Challenges

However, CEST is still a relatively new technique, and a lot of challenges remain to be addressed.

a) Nearly half of the CEST studies were performed on high field scanners (4.7 T or above). This is because CEST signal is related to the field strength. The sensitivity can be improved on high field scanners. In addition, the chemical shift between water protons and solute protons is also dependent on the field strength. For example, the chemical shift between glucose protons and water protons is 1.2 ppm, 147.6 Hz on 3T scanners and 344.4 Hz on 7T scanners. As discussed before, if the chemical shift is a lot smaller than the exchange rate, the solute proton will fall in the fast exchange regime, which means the solute proton peak will merge with the water peak. In general, fast exchange protons will have better performance on high field scanners because there is a better separation between the water peak and solute proton peak.

b) CEST contrast is normally complicated because it involves multiple confounding factors. When performing in vivo CEST experiments, there are also other competing effects like direct saturation effects and MT effects. There are also competing NOE effects (resonant frequency - 3.5 ppm) if asymmetry analysis is used in APT imaging (amide protons resonant frequency +3.5 ppm). CEST contrast is also dependent on water relaxation parameters T_1 and T_2 . While most

people believe that the CEST signal change is mostly caused by the solute proton concentration and the exchange rate, the complexity of CEST signal should always be kept in mind.

c) CEST contrast is complicated not just because of the confounding factors from the tissue properties, but also because it can be affected by external factors including the field strength, the parameters of CEST preparation module (saturation time and RF irradiation power B_1) and the data analysis. Therefore, it needs careful consideration to compare the CEST results from different scanners. This adds difficulty to perform multi-center trials.

d) Quantifying the concentration and exchange rate from other CEST contributing factors can potentially address the above issues. However, this is difficult because CEST mechanism is based on the complicated Bloch-McConnell equation. There is no explicit analytical solution to the equation. All current methods are based on approximated analytical solution (58-60). This becomes especially challenging when the Gaussian-shaped saturation pulses are used on clinical scanners because this adds a constant-varying input B_1 to the equation. These methods repeat CEST experiments multiple times with different CEST saturation modules to fit for the concentration and exchange rate and would normally require long scan time. Therefore, these methods have only been used in phantoms or preclinical models so far.

1.5 Aims

The broad, long term goal of this dissertation project is to develop CEST techniques for better clinical translation. More specifically, the goal is to apply the techniques on 3T clinical scanner and address the challenges for different applications. In this work, the major applications are the heart and the spine. For cardiac CEST, the primary focus is to improve the speed and robustness of the technique. For application in the spine, the primary focus is to improve quantitative CEST and apply it to in vivo studies.

Aim 1: To develop a clinical translatable cardiac CEST technique for myocardial metabolic activity assessment.

Aim 1.1: To develop a practical and translatable cardiac CEST approach and test in chronic myocardial infarction animal model.

Chapter 2 presents an optimized cardiac CEST method with more efficient data acquisition scheme, advanced motion correction methods and improved CEST signal analysis to achieve a clinically affordable scan time. Preliminary validation studies will be performed in chronic myocardial infarction animal model. The choice of this animal model is because previous studies have shown that the scar has reduced metabolism compared to remote myocardium. Established and validated late gadolinium enhancement (LGE) will serve as an in vivo reference for the characterization of scar.

Aim 1.2: To develop an improved cardiac CEST technique with dual-echo readout to address B_0 field variation issue.

In Chapter 3, an improved cardiac CEST technique with dual-echo readout was proposed to allow simultaneous acquisition of CEST-weighted images and B_0 maps. This technique was developed to address the B_0 field variation within navigator acceptance window. Repeatability studies will be performed to compare between the previous and proposed cardiac CEST methods.

Aim 2: To develop a quantitative CEST (qCEST) imaging protocol of intervertebral disc for pH assessment and evaluate its applicability for diagnosis of discogenic pain.

Aim 2.1: To develop a quantitative CEST (qCEST) imaging protocol of intervertebral disc for pH assessment and validate in a porcine model.

Chapter 4 presents the qCEST imaging protocol of intervertebral disc for pH assessment. It is based on the observation that CEST effect can be represented as a linear function of $1/B_1^2$. Multiple CEST experiments with varying B_1 amplitudes will be performed for omega plot analysis to quantify the exchange rate, which is dependent on pH. Validation studies will be performed in a porcine model on a 3T MR scanner. Na-Lactate will be injected into the IVDs to induce various pH values within the discs ranging from 5-7. The exchange rates measured from qCEST will be

compared with the pH values measured directly using tissue pH-meter to evaluate whether qCEST can provide accurate pH measurements.

Aim 2.2: To preclinically test and validate the hypothesis that the proposed qCEST imaging protocol can detect pH changes in the intervertebral discs in the process of disc degeneration.

Chapter 5 applies the qCEST imaging protocol validated in Chapter 4 in a pre-clinical animal model. MRI scans will be performed 2, 6 and 10 weeks after IVD degeneration was induced. pH will be directly measured inside the IVD using tissue pH-meter to serve as a reference. Pain, nerve- and inflammatory-related markers will be analyzed from the harvested degenerated IVDs. Direct comparison will be performed between qCEST signal and pain markers to evaluate if qCEST can potentially serve as a non-invasive method for the diagnosis of discogenic pain.

Aim 3: To develop CEST-fingerprinting technique for more efficient and more accurate CEST quantification.

Chapter 6 presents the CEST fingerprinting framework for more efficient and more accurate CEST quantification. This is inspired by the magnetic resonance fingerprinting concept where the signal generated using randomized sequence parameters will be matched directly to a pre-defined dictionary instead of using a repeated, serial acquisition of data to fit to a particular equation. CEST fingerprinting utilizes CEST saturation with varying saturation power B_1 amplitude and saturation time to create uniqueness of signal evolution for different exchange rates. Preliminary validation studies were performed in phantoms.

CHAPTER 2: Optimized Cardiac CEST MRI for Assessment of Metabolic Activity in the Heart

2.1 Significance

Adenosine triphosphate (ATP) is an essential energy source that governs myocardial contraction. In the heart, the synthesis of ATP mostly involves the conversion from phosphocreatine (PCr) to creatine (Cr) catalyzed by creatine kinase (CK) where PCr serves as the energy reservoir(61). During ischemia, PCr will be quickly depleted to maintain ATP supply. In the persistent occlusion, the CK system, including ATP, Cr and PCr will all be depleted(62,63). It has been previously reported that reduced ATP, Cr and PCr is associated with chronic MI(12,49,64) and heart failure(48,61,65). At this stage, the energy reserve of myocardium has reached its edge, which means the heart is at high risk of acute mechanical failure at a sudden increase in cardiac workload. Thus, the capacity of CK/PCr/Cr system can serve as a great indicator of the myocardial metabolic level, and to further assess myocardial contractility and cardiac function.

Cardiovascular disease (CVD), as the leading cause of death in the United States, causes nearly 600,000 deaths every year(66,67). More than 1 in 3 US adults live with one or more types of CVD(68). As discussed before, it has been previously shown that myocardial metabolic activity is closely correlated with cardiac mechanical performance(69-71). This topic has attracted a lot of attention because of the potential to improve cardiac performance by myocardial metabolic therapy (72-74). Therefore, assessment of myocardial metabolism might have a significant impact on improving prognosis of patients and enhancing the understanding in CVD.

2.2 Background

ATP is an essential energy source that governs myocardial contraction (75). The CK system plays a vital role in the synthesis of myocardial ATP. ATP is generated from the conversion of PCr and adenosine diphosphate (ADP) to Cr catalyzed by CK. Previous studies have linked

cardiac dysfunction to the loss of metabolites in the CK system (76-78). The measurement of Cr or PCr can serve as a biomarker to investigate the metabolic change in the myocardium (48,50,65,79,80).

Chemical exchange saturation transfer (CEST) is an emerging MRI technique for metabolic imaging (1). By saturating the solute protons, water signal will also drop because of the constant exchange between solute protons and water protons (3). It has been shown that CEST can be used to map Cr distribution because of chemical transfer between its amine protons ($-NH_2$) and water protons. CEST can detect Cr separately from other CK metabolites because Cr protons alone have an intermediate transfer rate with water protons (10,11,81). Compared to MR spectroscopy techniques, CEST yields better spatial resolution and higher sensitivity because of indirect detection via water protons (11,13).

CEST has been applied in the heart for in vivo endogenous Cr imaging in animal studies (12,82-84). Haris et al. was the first to show the feasibility of high-spatial-resolution mapping of Cr using cardiac CEST. However, the method poses some technical challenges which could potentially hinder the clinical translation of the cardiac CEST technique: (a) long scan time (~50 min per slice), (b) residual cardiac and respiratory motion, and (c) B_0 field variations mostly induced by respiratory motion.

In this study, we developed a clinically translatable cardiac CEST technique with significantly reduced scan time (~5 min), improved motion registration and CEST signal analysis to address the aforementioned challenges. The proposed technique was then validated in chronic myocardial infarction porcine model using late gadolinium enhancement (LGE) as a reference. This animal model was chosen because it has been clearly shown that scar regions have reduced metabolic activity level compared to remote myocardium (85).

2.3 Methods

2.3.1 Animal Preparation

All animal-related procedures were approved by the Institutional Animal Care and Use Committee (IACUC) at Cedars-Sinai Medical Center. Myocardial infarction was induced in 15 Yucatan minipigs following the procedure described in a previous study (86). Specifically, animals were sedated by intramuscular ketamine 20 mg/kg, acepromazine 0.25 mg/kg and atropine 0.05 mg/kg, followed by 10 mL intravenous thiopental. Endotracheal intubation was then performed, and anesthesia maintained by ventilation with 1% to 2% isoflurane. Catheters were inserted through the left carotid artery. Coronary X-ray angiography was performed to visualize the coronary arteries and identify the site for occlusion. An anteroseptal myocardial infarction was induced by inflation of an angioplasty balloon in the mid-left anterior descending artery to cause coronary occlusion for 2.5 hours. Finally, the animals were taken to the post-op recovery room. All imaging was performed eight weeks after the infarction.

2.3.2 MRI Protocol

Animal studies (N = 15) were performed on a 3 Tesla clinical scanner (Magnetom Verio; Siemens Healthcare, Erlangen, Germany) using a 12-channel phase array coil for data acquisition. Throughout the imaging procedures, anesthesia was maintained with isoflurane (1-3.5%).

The imaging protocol included bSSFP CINE, cardiac CEST and LGE. bSSFP CINE was performed to localize the quiescent period of the cardiac cycle ($1.4 \times 1.4 \times 6 \text{ mm}^3$; 35 cardiac phases, TR/TE = 3.2/1.6 ms; flip angle 50°). LGE imaging was completed 15 minutes after the contrast agent injection (0.1 mmol/kg, gadobutrol, Gadovist, Bayer Inc.) using phase sensitive inversion recovery FLASH ($1.3 \times 1.3 \times 6 \text{ mm}^3$; TR/TE/TI = 362/1.5/335 ms; flip angle 20°). All imaging was performed in the short axis plane at three mid-ventricular slice locations of the left ventricle. Breath hold was controlled by a ventilator in CINE imaging and LGE imaging.

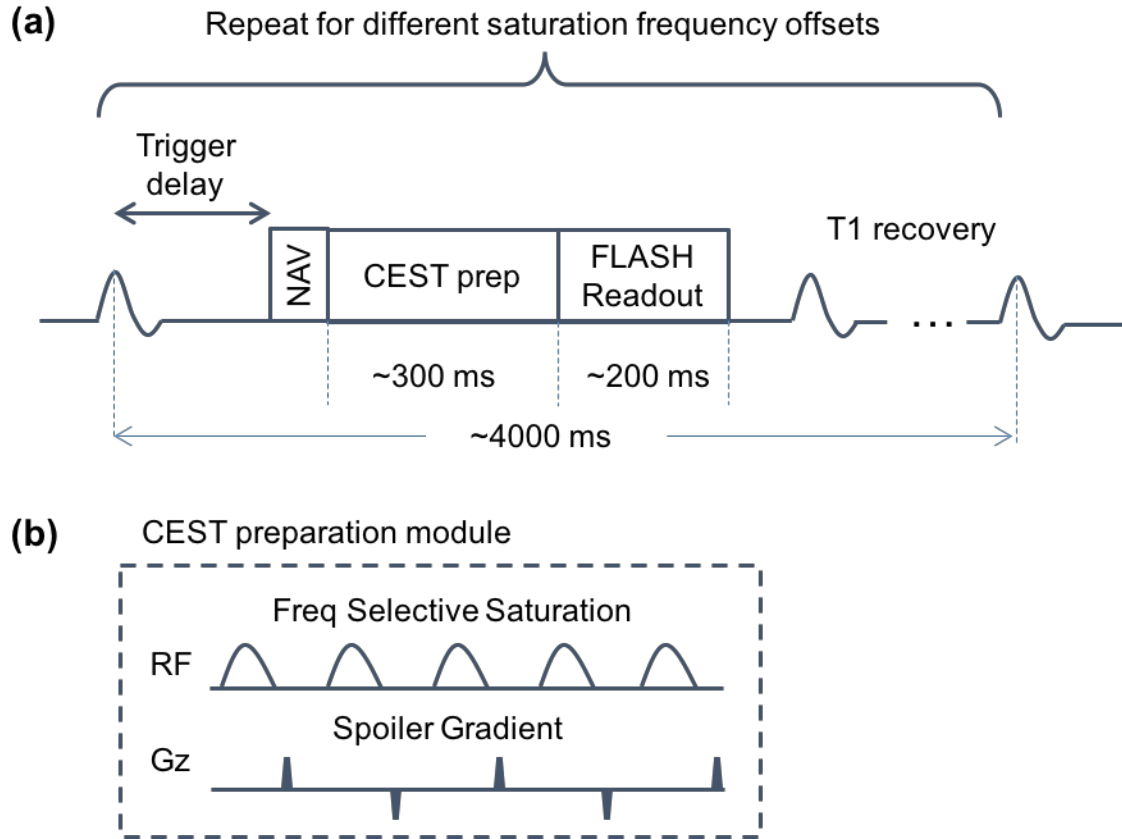


Figure 2.1 Pulse sequence diagram of the optimized cardiac CEST imaging technique.

Cardiac CEST scans were performed before the contrast injection using FLASH readout (resolution $2.1 \times 2.1 \text{ mm}^2$; slice thickness 6-8 mm; TR/TE = 4000/1.5 ms; flip angle 12°). Fig. 1 shows the pulse sequence diagram of the proposed cardiac CEST technique. ECG triggering and navigator gating were used to reduce the effects of cardiac and respiratory motion. Each image was acquired by single-shot FLASH (~200 ms readout block placed in quiescent period). Thirty-three images were collected at different saturation frequency offsets ranging from -4.8 ppm to 4.8 ppm with a step size of 0.3 ppm. The CEST preparation module consists of five Gaussian-shaped pulses with 2700° flip angle and 30 ms duration at a duty cycle of 50% (the equivalent B_1 power is 3.76 μT). The spoiler gradient was altered in different directions to crush the residual transverse magnetization. An additional image was acquired without CEST saturation for normalization

reference. The scan time for each slice was approximately 5 minutes with 40% navigator efficiency.

Cardiac CEST imaging technique was optimized in the following aspects: (a) Images were acquired by single-shot FLASH instead of segmented acquisition, significantly increasing the scan efficiency. (b) All images were registered to reduce the residual left ventricle wall motion (up to 4 mm myocardial displacement) using Medical Imaging Registration Toolbox (MIRT) (87). (c) The acquired Z-spectrum was fitted to the Lorentzian-shaped 3-pool-model to increase the reliability of the generated CEST contrast map by reducing the impact of signal fluctuation from B_0 field shifting introduced by respiratory motion.

2.3.3 Image Analysis

Post processing was performed with custom-written programs in Matlab (The Mathworks, Natick, MA, USA). For each pixel, the Z-spectrum was generated as the signal intensity of each image acquired at different saturation frequency offsets normalized by the reference image. The Z-spectrum was fitted to the following equation.

$$Z(\Delta\omega) = 1 - \left(\sum_{i=1}^3 L_i(\Delta\omega) - \sum_{i=1, j>i}^3 (L_i(\Delta\omega) \times L_j(\Delta\omega)) + \prod_{i=1}^3 L_i(\Delta\omega) \right) \quad [2.1]$$

$i = \text{CEST, MT or DWS}$

$$L_{\text{CEST}} = A_0 \frac{(\Gamma_0/4)^2}{(\Gamma_0/4)^2 + (x - \delta_0)^2}$$

$$L_{\text{MT}} = A_1 \frac{(\Gamma_1/4)^2}{(\Gamma_1/4)^2 + (x - \delta_1)^2}$$

$$L_{\text{DWS}} = A_1 \frac{(\Gamma_1/4)^2}{(\Gamma_1/4)^2 + (x - \delta_1)^2}$$

This could separate the acquired Z-spectrum into CEST, direct saturation (DS), and conventional magnetization transfer (MT), three major effects in saturation experiments with aqueous solutions (12,88). The center of the DS curve is the central water frequency, which

represents B_0 field information. The distance between the center of the CEST curve and DS curve is constantly +1.8 ppm, which is the resonant frequency of amine protons. CEST signal is defined as the amplitude of the fitted CEST curve.

CEST maps were generated using pixel-by-pixel Z-spectrum fitting in the myocardium. Regions of interest (ROIs) were placed in the center of scar region and the healthy remote myocardium using LGE as reference and avoiding the border zone. The average CEST signal was determined in scar and healthy remote myocardium. Comparisons were performed using Wilcoxon rank-sum test in GraphPad Prism 6 (GraphPad Software, La Jolla, California, USA). A two-tailed value of $p < 0.05$ was considered to be statistically significant.

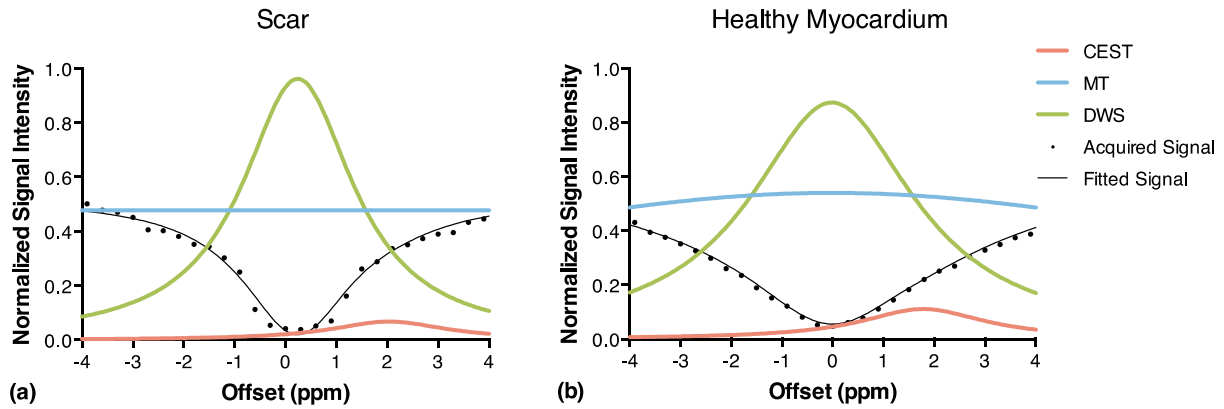


Figure 2.2 Z-spectrum of (a) scar region and (b) healthy myocardium. By using the 3-pool-model fitting, Z-spectrum (black) was separated into CEST curve (pink), MT curve (blue) and DWS curve (green). The center of DWS curve represents the resonant water frequency (B_0 field). The peak of CEST curve was defined as the CEST signal. It is clear that the healthy myocardium has higher CEST signal than scar, which suggests more Cr distribution in the healthy myocardium.

2.4 Results

To separate the CEST signal from MT and DS effects, we used 3-pool-model fitting to analyze the Z-spectrum (Fig. 2). The peak of the CEST curve is defined as CEST signal, which is used in the following quantitative analysis. Comparing the Z-spectrum analysis curves in the scar with those in the healthy myocardium, it is clear that CEST signal is lower in the scar region.

Fig. 3 shows typical CEST contrast maps and corresponding LGE images in three slice locations. The infarcted regions have lower CEST signal than healthy remote myocardium. Spatially, the hypointense regions in the CEST contrast maps closely match the bright areas in LGE images.

In all animals, infarct CEST signal (0.09 ± 0.04) is significantly reduced compared to the CEST signal found in the healthy remote myocardium (0.16 ± 0.03), $p < 0.0001$, as shown in Fig.

4.

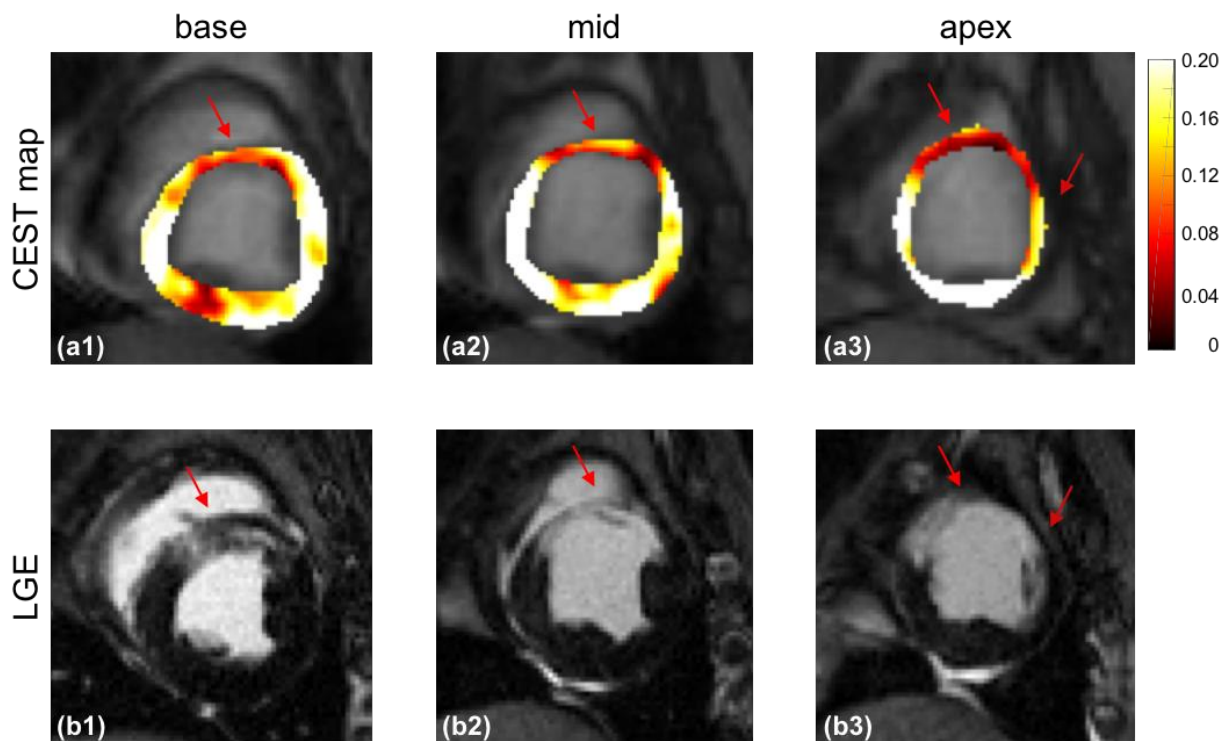


Figure 2.3 (a) CEST maps and (b) corresponding LGE images of one representative subject in three slice locations. The hypointense regions (arrows) in the CEST maps match the LGE positive regions (arrows).

2.5 Discussion

In this work, we developed a cardiac CEST technique with significantly reduced scan time (~5 min), improved motion registration and CEST signal analysis to show the feasibility of the proposed technique in detecting Cr distribution in the myocardium in a clinically feasible scan time.

This feasibility study in a porcine model showed decreased CEST signal in infarcted region compared to remote myocardium. The results suggest a lower Cr distribution in the infarcted region, which is consistent with previous findings (85).

As CK metabolites are essential in providing energy for myocardial contraction, cardiac metabolic impairment is now considered as a cause, rather than a result of cardiac diseases (71). Detection of CK metabolites such as creatine can potentially help the clinical diagnosis and treatment of cardiac diseases. It can be used to further understand the underlying mechanisms of metabolic change processes in cardiac diseases as well as to evaluate therapy efficiency and guide therapy optimization.

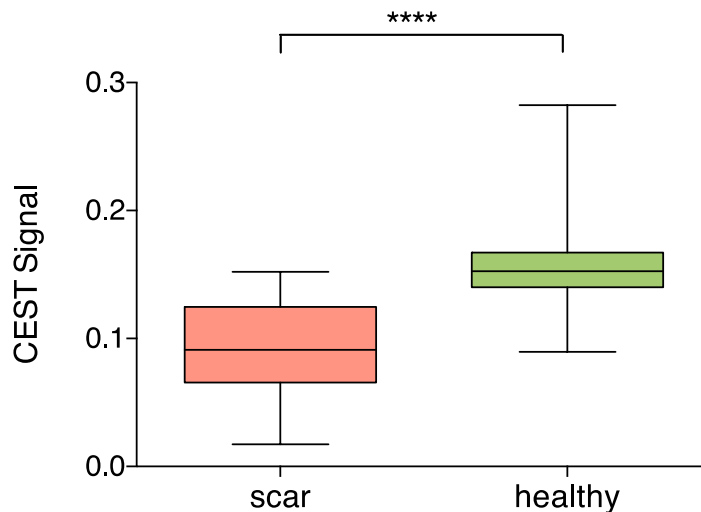


Figure 2.4 CEST signal in the scar (0.09 ± 0.04) is significantly reduced compared to healthy remote myocardium (0.16 ± 0.03), $p < 0.0001$.

Cardiac MR Spectroscopy (MRS) is also capable of detecting the activity of CK metabolites in the myocardium. PCr and ATP can be detected as two peaks in ^{31}P spectrum. The ratio of PCr over ATP can serve as an indicator of myocardial energy metabolism (51,79). In ^1H spectrum, Cr and PCr have the same chemical shift and only their combined total amount can be measured (65,89). However, these techniques have not gained common application over the years because of limitations such as low spatial resolution, lengthy scan time, and complicated

acquisition protocol. ^{31}P MRS also requires additional hardware, which limits its availability. All of these issues hinder the clinical translation of cardiac MRS approaches. However, they can be potentially addressed by cardiac CEST techniques. In this study, we have shown the feasibility of cardiac CEST imaging with typical cardiac MRI spatial resolution and clinically acceptable scan time. Cardiac CEST is also more sensitive compared to MRS techniques because the signal is indirectly detected from the water pool. Without any special requirement for hardware or technician training, this technique can be easily translated into clinical studies.

The cardiac CEST sequence we proposed in this study is significantly faster than the previous technique(12). One of the major reasons is that we used single-shot FLASH readout instead of segmented readout. In addition to its contribution to speed acceleration, single-shot readout also minimizes the respiratory motion within the acquisition of each CEST-weighted image at different saturation frequency offsets. This reduces the motion artifacts and B_0 field changes within the acquisition of each single image. It should be noted, though, when the subject has a relatively high heart rate and short quiescent period, the image acquired using single-shot readout will be blurrier. More advanced image reconstruction methods can be used in the future to shorten the acquisition period.

It is known that the heart is one of the most difficult organs for imaging because of constant cardiac motion and respiratory motion. In cardiac CEST imaging, in addition to the motion within the acquisition of one image that leads to blurriness and the misregistration between different images that causes error in pixel-by-pixel mapping, we are also facing B_0 field variations caused by residual motion. Respiratory phase mismatch, even within the navigator acceptance window, leads to B_0 field variations in the myocardium for images acquired with different saturation frequency offsets. This is because the relative position of heart (tissue) and lung (air) is changing. It is especially worse in the lateral wall region, because this is the interface between heart and lung and B_0 field is changing rapidly in this region. In this study, 3-pool-model fitting is used to generate CEST signal so the B_0 field variations can be treated as noise. However, this method

can address this issue only to certain extent. Therefore, sometimes inhomogeneity is observed in the CEST map (Fig. 3), especially in the lateral wall region. This issue can be potentially addressed using advanced shimming coil design so the B_0 field over the myocardium can be more homogeneous.

This study shows the feasibility of cardiac CEST technique in a pre-clinical setting. However, more studies are needed for further investigation. The animal model used in this study only yielded transmural infarcts. Non-transmural infarcts are typically smaller in size and may be more difficult to detect. Whether the spatial resolution and sensitivity of the current technique is enough for non-transmural infarcts requires more studies. The results show that the infarct region has about 50% drop in CEST signal compared to healthy remote myocardium. In some mild cardiac dysfunctions, the difference could be smaller. Further investigation is needed to evaluate whether cardiac CEST technique has the reproducibility and sensitivity to detect cardiac dysfunctions with mild metabolic abnormalities. Histopathology studies are also needed to demonstrate the CEST signal change is correlated to creatine distribution in the myocardium.

2.6 Conclusion

We developed a clinically feasible cardiac CEST technique that is significantly faster than the previous approach. In a chronic myocardial infarction pig model, we demonstrated the proposed CEST technique can discern differences in the CEST signal between infarct and remote myocardium. This technique has the potential to provide information on metabolic abnormalities for cardiac diseases.

CHAPTER 3: Cardiac CEST MRI with Dual-Echo Readout for B₀ Correction: A Repeatability Study

3.1 Background

ATP is the most important energy source in the myocardium. It governs the myocardial contraction. Creatine kinase (CK) system is essential in resynthesizing ATP and the capacity of substrates involved in this system, like Cr, can serve as a great indicator of the myocardial metabolic level.

Previous studies have shown the feasibility of cardiac CEST technique to detect creatine loss in chronic myocardial infarction. This suggests that cardiac CEST has the potential to provide information on metabolic abnormalities for cardiac diseases. However, B₀ field variations, mostly caused by respiratory motion within the acceptance window in a navigator-gated acquisition, especially on the edge of heart-lung interface, can induce errors of the CEST signal. In addition, the reproducibility of cardiac CEST technique has not been assessed. Whether this technique can be used to detect mild myocardial metabolic impairment still needs further investigation.

In this work, we developed a cardiac CEST dual-echo technique which not only acquires CEST-weighted image, but also enables acquisition of B₀ map for each saturation frequency offset. CEST reproducibility with the technique was assessed.

3.2 Method

3.2.1 Sequence Diagram

Fig. 3.1 shows the sequence of the proposed cardiac CEST dual-echo technique. The structure is similar as the sequence that has been presented in Chapter 2. The major difference is that dual-echo readout was used for image acquisition to allow simultaneous acquisition of B₀ map and CEST-weighted images.

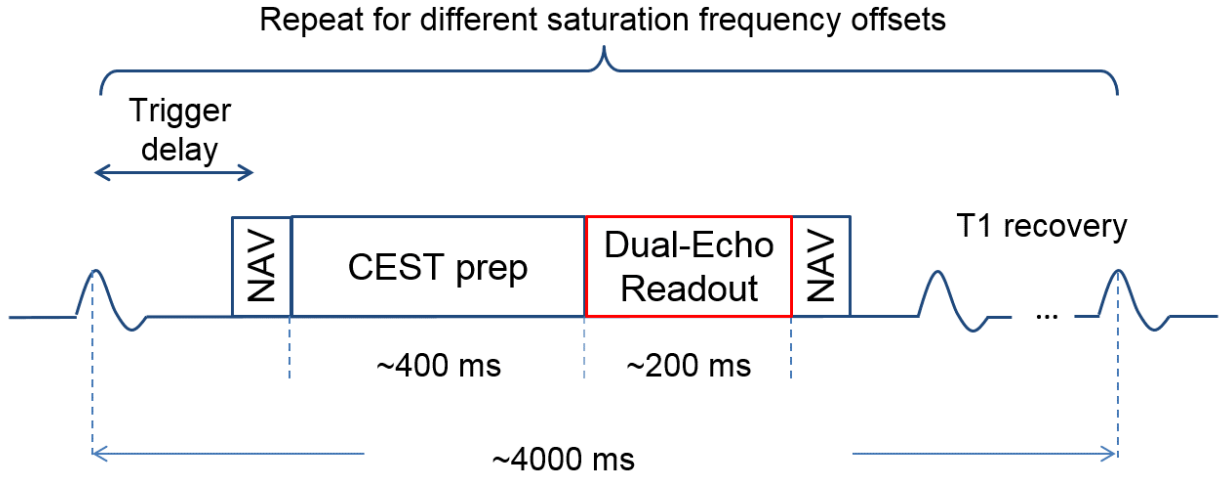


Figure 3.1 Sequence diagram of proposed cardiac CEST technique with dual-echo readout.

3.3.2 Image Processing

Figure 3.2 shows the analysis of images acquired at each CEST saturation frequency offset. For each echo, both magnitude images and phase images were reconstructed. Two phase images were used to calculate the B_0 map according to the following equation.

$$\Delta B_0 = \frac{\text{phase1} - \text{phase2}}{\gamma(\text{TE1} - \text{TE2})} \quad [3.1]$$

Two magnitude images were averaged to generate the CEST-weighted images. With known B_0 maps for each frequency offset, the acquired Z-spectrum was fitted to Eq. 2.1 with one fewer unknown variable. CEST signal is defined as the amplitude of fitted CEST curve. CEST contrast map was generated using pixel-by-pixel Z-spectrum fitting in the myocardium.

3.2.3 MRI Protocol

Healthy volunteer studies (N = 14) were performed on a 3T clinical scanner (Magnetom Verio; Siemens Healthcare, Erlangen, Germany) using a 32-channel phase array coil for data acquisition.

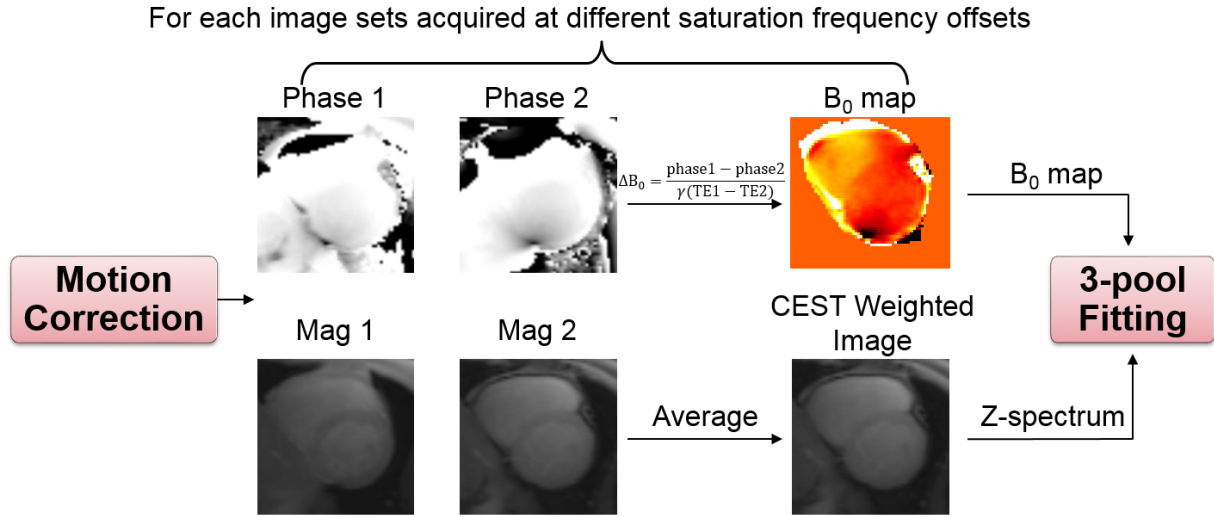


Figure 3.2 Image processing workflow of the proposed cardiac CEST dual-echo method.

Repeatability was evaluated in two mid-ventricular slices for both the previous and proposed methods. The sequence parameters were shown in Table 3.1. The two methods used the same CEST preparation parameters. 3 Gaussian-shaped pulses with flip angle of 2700° and pulse duration of 80 ms were used in the CEST preparation module. The interpulse delay was 80 ms. Equivalent RF irradiation power is 1.90 μT . CEST saturation frequency offsets range from -3.6 ppm to 3.6 ppm with a step size 0.3 ppm. Both methods used single-shot flash readout (FOV: $350 \times 280 \text{ mm}^2$; spatial resolution: $2.7 \times 2.2 \times 8.0 \text{ mm}^3$; matrix size: 160×104 ; iPAT: 2; flip angle: 12°). For the previous method, $\text{TR}/\text{TE} = 4000/1.5 \text{ ms}$. For the dual-echo method, the same TR was maintained, while the TE1 is 0.97 ms and TE2 is 2.44 ms. Partial Fourier 6/8 was used to maintain the same acquisition window without inducing too much cardiac motion for the dual-echo method. The scan time is approximately 5 min for both methods.

3.3.4 Data Analysis

The myocardium was segmented according to the standard American Heart Association model (90). The repeatability of CEST signal was compared globally and segmentally for both

previous and proposed methods. Comparisons were performed using Bland-Altman plot in GraphPad Prism 6 (GraphPad Software, La Jolla, California, USA).

Table 3.1 Imaging parameters for the previous and proposed cardiac CEST methods

	Previous Method	Proposed Method
FOV	350 mm x 280 mm	
spatial resolution	2.7 mm x 2.2 mm	
parallel imaging	R = 2	
Image matrix size	160 x 104	
Flip angle	12°	
TE	1.45 ms	0.97/2.44 ms
TR (echo spacing)	2.4 ms	3.9 ms
Acquisition window for each slice	163 ms	194 ms
Partial Fourier	N/A	6/8
slice positions	2 mid-ventricular slices (8 mm thickness)	
CEST preparation module	3 Gaussian-shaped pulses with flip angle of 2700° and pulse duration of 80 ms at duty cycle of 50%	

3.3 Results

Fig. 3.3 shows the representative images of the proposed cardiac CEST method with dual-echo readout. Fig. 3.3a-d represents the CEST-weighted images acquired at different saturation frequency offsets. Fig. 3.3e shows the CEST map. The homogeneity across the myocardium can be appreciated.

The Bland-Altman plots of CEST signal were shown in Fig. 3.4. As shown in Fig. 3.4a, the repeatability of the average CEST signal of the entire myocardium using proposed method is improved compared to the previous method. Fig. 3.4b and c represent the Bland-Altman plots of average CEST signal in the lateral segment and septal segment, respectively. It can be seen that

most of the improvement comes from the lateral wall segment. This is because there is more B_0 variations in this region.

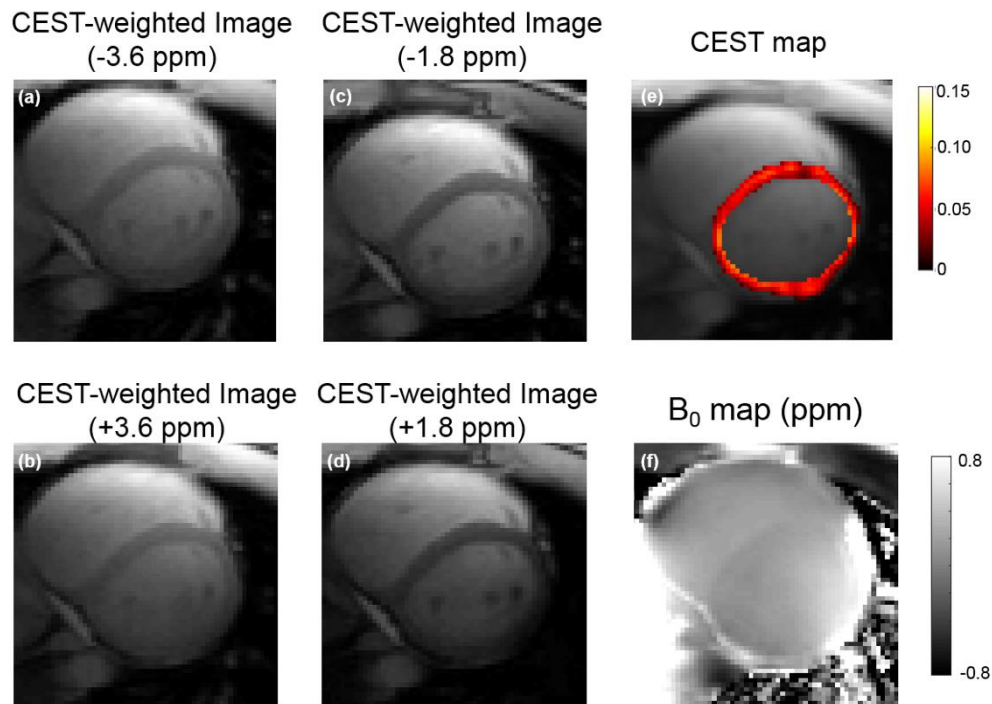


Figure 3.3 Representative images of proposed cardiac CEST method with dual-echo readout. (a-d) CEST-weighted images acquired at different saturation frequency offsets. **(e)** CEST contrast map. **(f)** B_0 map.

3.4 Discussion

In this study, we developed a new cardiac CEST method with dual-echo readout. This technique allows simultaneous acquisition of B_0 map and CEST-weighted images. In the healthy volunteer studies, it is shown that the proposed technique has improved repeatability compared to the previous method.

As shown in Fig. 3.4, the repeatability of the proposed method is significantly improved in the lateral wall segment, while the improvement of the repeatability in the septal segment is not as obvious. The lateral wall segment is on the edge of heart-lung interface. The B_0 field in this area is more sensitive to relative location change of heart and lung induced by respiratory motion.

However, CEST imaging is also very sensitive to B_0 field inaccuracy, especially for the protons whose resonant frequency is very close to water. Therefore, with addition B_0 field correction instead of treating it as an unknown in the fitting equation could improve the repeatability if cardiac CEST.

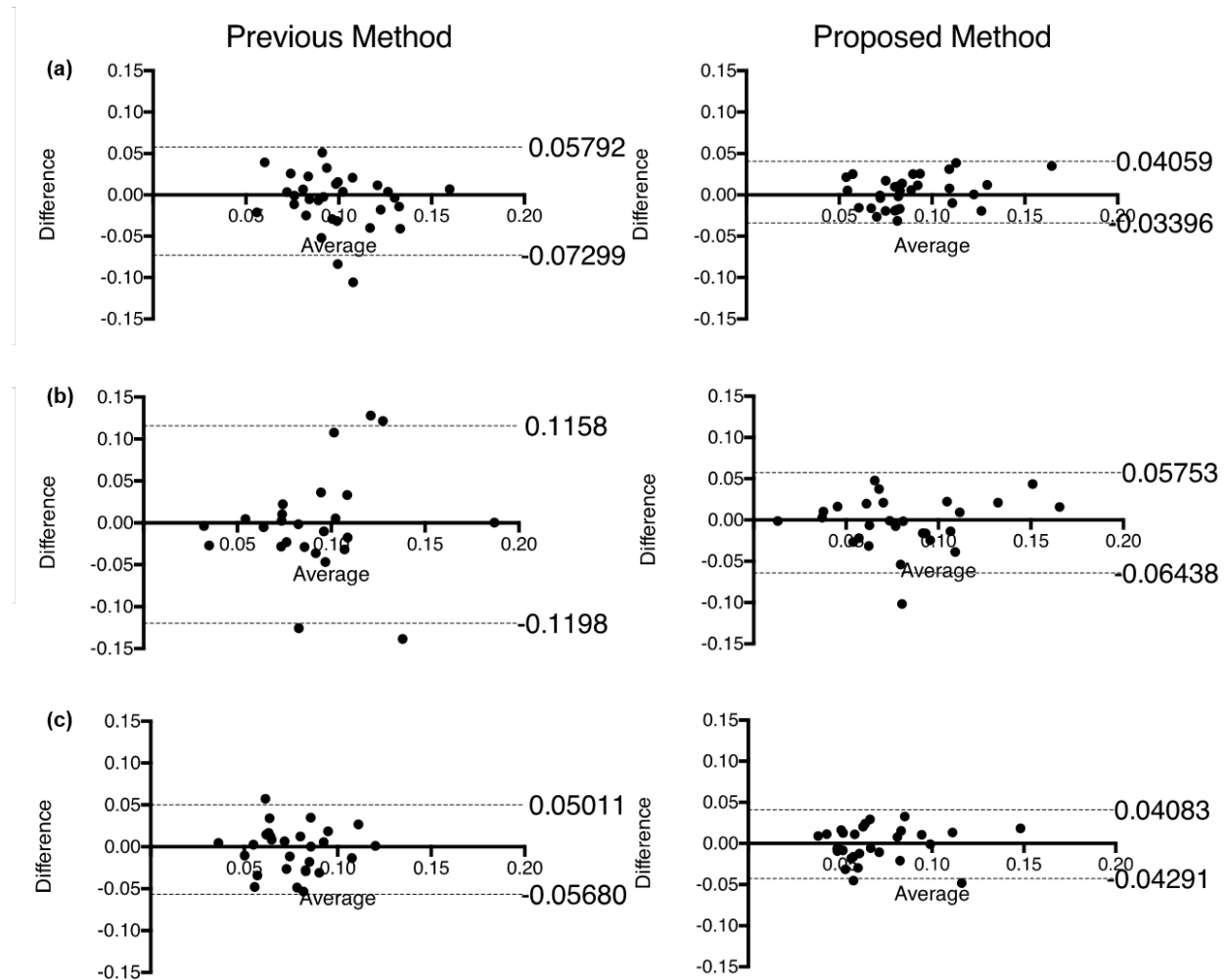


Figure 3.4 Bland-Altman plots of CEST signal for previous and proposed cardiac CEST methods. (a) Average CEST signal of the entire myocardium. **(b)** Average CEST signal in the lateral segment. **(c)** Average CEST signal in the septal segment. The dashed lines represent 95% limits of agreement.

In this study, the proposed cardiac CEST method was applied in healthy subjects. However, further investigation is needed to evaluate whether the proposed technique can detect mild metabolic impairment in diabetic patients, coronary microvascular patients or tako-tsubo

patients (50,91). These patient groups have been shown to have reduced myocardial metabolic activity. In addition, cardiac CEST could also serve as additional information to evaluate whether the myocardial treatment is effective.

3.5 Conclusion

In this study, a cardiac CEST dual-echo method was developed for simultaneous acquisition of B_0 maps and CEST-weighted images. The proposed technique is shown to have improved repeatability compared to the previous method.

CHAPTER 4: Quantitative Chemical Exchange Saturation Transfer (qCEST) MRI of Intervertebral Disc in a Porcine Model

4.1 Significance

Lower back pain is a major medical condition estimated to affect up to 85% of the US population (92). It is the leading cause of disability globally (93). It has posed large economic burden to the society. The annual direct medical costs of lower back pain in US ranged from \$12 billion to \$90 billion, while the annual indirect costs ranged from \$7 billion to \$28 billion (94). The major categories of indirect costs are sick leave and early retirement. There is no significant gender difference (95).

The common causes of lower back pain include intervertebral disc (IVD) degeneration, injury or overuse of muscle, herniation, osteoarthritis, spinal stenosis, etc. Among these causes, disc degeneration is a significant portion (at least 40%), leading to the term “discogenic pain” (96). Although degenerated discs can be identified using MRI, they do not always cause pain. Therefore, if a patient with lower back pain has several degenerate discs, further examination is required to determine which disc is the source of the pain, prior to a decision of surgical intervention. Standard procedures include discography, during which the suspected discs are pressurized in order to provoke pain. This is a painful procedure that is also known to further accelerate disc degeneration, disc herniation, and loss of disc height and affect the adjacent endplates (97). It is also subjective to variations of the placement of the needle, pressure exerted, and anesthesia.

Recent studies have associated low pH with discogenic pain (98,99). pH could potentially serve as a new metabolic biomarker for discogenic back pain (100).

4.2 Background

Chemical exchange saturation transfer (CEST) is an emerging MR technique to measure pH-dependent signal changes (13,101-103). This technique exploits the constant chemical exchange, which is pH-sensitive, between water protons and solute protons in certain molecules. The chemical exchange rate is dependent on pH values. The solute protons are first magnetization-saturated with a series of frequency selective radiofrequency (RF) pulses, and after exchanging with water protons, the saturation is indirectly detected in the water signal (1,3).

Glycosaminoglycan (GAG) is a critical component to support the function in the IVD. It has been reported that GAG can be detected by CEST imaging because of its exchangeable hydroxyl protons (4,6). Previous studies have applied gagCEST to detect pH change in the IVD in animal models and patients with degenerative disc disease (8,9). However, CEST contrast is a rather complicated effect. It involves multiple confounding factors, including but not limited to: (a) exchange rate between water and GAG protons, which is dependent on the pH; (b) labile proton ratio, which is linearly correlated with GAG concentration; (c) water relaxation parameters T_1 and T_2 ; and (d) the RF irradiation power of the CEST saturation module.

Multiple studies have focused on separating the exchange rate or the labile proton ratio from other confounding factors in the CEST experiments (59,60,104-107). Among these methods, quantitative CEST (qCEST) allows for simultaneous measurements of the exchange rate and labile proton ratio. It was developed based on the observation that the CEST effect can be represented as a linear function of $1/B_1^2$ (108). Multiple CEST experiments were performed with varying B_1 amplitudes for omega plot analysis (108).

Simultaneous measurements of pH value and concentration using qCEST have been shown in creatine phantom studies (60,106,107). Creatine protons have a slow to intermediate exchange rate with water protons (81). However, for GAG protons which undergo relatively faster chemical exchange, whether this technique can detect pH changes has not been investigated. In addition, most of the studies were performed on a preclinical scanner using continuous-wave (cw)

saturation pulse (60,107). No in vivo validation has been performed and potential clinical application is not yet clear.

In this work, we propose an in vivo pH-dependent imaging technique in the IVD using qCEST on a 3T clinical scanner. We tested the technique in GAG phantoms and validated it in vivo in a porcine model using measurement from the tissue pH probe as reference.

4.3 Theory

Previous studies have studied the two-pool exchange model using Bloch-McConnell equations, describing the proton exchange between pool 'w' (water pool) and pool 's' (solute pool). In this two-pool system, f_r refers to the labile proton ratio M_{0s}/M_{0w} and k_{sw} the exchange rate between solute pool and water pool. R_{1w} , R_{2w} , R_{1s} and R_{2s} are longitudinal and transverse relaxation rates for water protons and solute protons, respectively.

The conventional CEST asymmetry analysis takes direct difference between the label scan (at the resonant frequency of the solute pool) and reference scan (at the opposite frequency with respect to water). It can be defined as $CESTR = Z_{\text{label}} - Z_{\text{ref}}$, where Z_{label} and Z_{ref} are the normalized signal intensity or Z-spectrum for the label scan and reference scan. However, this analysis has its limits when it comes to quantitative imaging, because its expression is rather complicated and involves multiple confounding factors.

In recent studies, the inverse CEST difference ($CESTR_{\text{ind}}$) was proposed because of its simplified expression (60)

$$\frac{1}{CESTR_{\text{ind}}} = \frac{1}{\frac{1}{Z_{\text{label}}} - \frac{1}{Z_{\text{ref}}}} \approx \frac{R_{1w}}{f_r \cdot k_{sw}} + \frac{k_{sw} \cdot (R_{2s} + k_{sw}) \cdot R_{1w}}{f_r \cdot k_{sw}} \frac{1}{\omega_1^2} \quad [4.1]$$

where ω_1 is the RF irradiation amplitude.

Eq. [4.1] is only valid for cw CEST saturation. When pulsed saturation is applied in CEST experiments, Eq. [4.1] can be written as (106)

$$\frac{1}{\text{CESTR}_{\text{ind}}} \approx \frac{R_{1w}}{\text{DC} \cdot f_r \cdot k_{sw} \cdot c_1} + \frac{k_{sw} \cdot (R_{2s} + k_{sw}) \cdot R_{1w} \cdot c_2^2}{\text{DC} \cdot f_r \cdot k_{sw} \cdot c_1} \frac{1}{\omega_1^2} \quad [4.2]$$

where DC stands for duty cycle; c_1 and c_2 describe the shape of Gaussian saturation pulses ($c_1 = \sigma\sqrt{2\pi}/t_p$, $c_2 = c_1\sqrt{\sqrt{2}}$; σ and t_p are the width and length of the Gaussian pulse). Note ω_1 here is defined as the average RF irradiation amplitude of one Gaussian pulse, i.e., $\omega_1 = \text{flip angle/pulse duration}$.

In this expression, $1/\text{CESTR}_{\text{ind}}$ is described as a linear function of $1/\omega_1^2$. By measuring $\text{CESTR}_{\text{ind}}$ with different RF irradiation amplitude, we can calculate the slope m and intercept n , and eventually estimate k_{sw} and f_r .

$$k_{sw} = \frac{\sqrt{R_{2s}^2 + \frac{4m}{n \cdot c_2^2}} - R_{2s}}{2} \quad [4.3]$$

$$f_r = \frac{R_{1w}}{k_{sw} \cdot n \cdot c_1 \cdot \text{DC}} \quad [4.4]$$

R_{1w} can be measured using T_1 mapping techniques. R_{2s} of GAG is approximately 200 s^{-1} (109).

Note Eq. [4.1] is a simplified expression that describes the steady state signal of CEST imaging. When performing qCEST experiments, RF saturation pulses need to be long enough to ensure the steady state is reached. The simplification only holds for dilute CEST agents undergoing slow and intermediate chemical exchange.

4.4 Method

4.4.1 Phantom Preparation

Two sets of phantoms containing GAG prepared from chondroitin sulphate A (Aldrich-Sigma, St. Louis, MO) and phosphate buffer solution (PBS) with varying pH values and concentrations were prepared. For the pH set, the GAG concentration was fixed at 60 mM and pH was titrated to 5.8, 6.1, 6.4, 6.7 and 7.0. For the concentration phantom, we used various GAG

concentrations (100 mM, 80 mM, 60 mM, 40 mM and 20 mM) and titrated the pH to 7.0. The solution was then transferred to 15 mL tubes. These ten tubes were put in a phantom holder filled with water.

4.4.2 In vitro MRI Experiments

Imaging experiments were performed at room temperature on a 3.0 Tesla clinical scanner (Magnetom Verio; Siemens Healthcare, Erlangen, Germany). All images were acquired with a slice thickness of 8 mm, field of view of 160 x 160 mm² and imaging matrix of 128 x 128.

CEST MRI was performed with pulsed RF saturation turbo spin echo (TSE) sequence (TR/TE = 16000/12 ms; 2 averages). CEST saturation module consists of 39 Gaussian-shaped pulses, with a duration $t_p = 80$ ms for each pulse and an interpulse delay $t_d = 80$ ms (duty cycle=50%, total saturation time $T_{\text{sat}} = 6240$ ms) at saturation flip angle 900°, 1500°, 2100° and 3000° (B_1 amplitudes = flip angle/ $(\gamma t_p) = 0.73\mu\text{T}$, $1.22\mu\text{T}$, $1.71\mu\text{T}$ and $2.45\mu\text{T}$; Gaussian saturation pulse parameters $c_1 = 0.50$, $c_2 = 0.59$). Z-spectrum was acquired with ten different saturation frequencies at ± 1.6 ppm, ± 1.3 ppm, ± 1.0 ppm, ± 0.7 ppm and ± 0.4 ppm. B_0 field was corrected using a water saturation shift referencing (WASSR) map (110).

T_1 -weighted MR images were acquired by an inversion recovery TSE sequence with 10 different inversion delays (TI = 50, 150, 350, 700, 1050, 1400, 2000, 2500, 3000 and 4000 ms; TR/TE = 6000/12 ms). T_2 -weighted MR images were acquired by a TSE sequence with varying echo delays (TE = 12, 24, 48, 97, 205 and 399 ms; TR = 6000 ms).

4.4.3 Animal Preparation

All animal-related procedures were approved by the Institutional Animal Care and Use Committee (IACUC) at Cedars-Sinai Medical Center. A total of four female Yucatan minipigs (S&S Farms) were used. Following an 18-hour preoperative fast, each pig was sedated with intramuscular drugs (acepromazine 0.25mg/kg, ketamine 20mg/kg, and atropine 0.02–0.05mg/kg), following which the animal was injected intravenously with propofol (2mg/kg) to

induce full anesthesia. After this had been achieved, the trachea was intubated and anesthesia was maintained using 1–3.5% isoflurane inhaled via the tracheal tube for the duration of the procedure. Following anesthesia, under fluoroscopic guidance three MR-compatible 14G coaxial needles (Invivo, Gainesville, FL) were inserted into the mid substance of lumbar discs L1/L2, L3/L4 and L5/L6. These lumbar discs were injected with different concentrations of Na-Lactate (Sigma Aldrich, St. Louis, MO) in order to induce a gradient of pH values within the discs ranging from 5 – 7, as described by Melkus et al (9), and in accordance with pH values measured within patients' pathological discs (111). Following intra-discal injection, exact pH values inside the discs were measured using a custom-made needle-shaped tissue pH probe (Warner Instruments, LLC, Hamden, CT) which was inserted through the MR-compatible needle, shortly before the MR scan. Lumbar disc L2/L3 was also scanned as the control disc. Its pH value was measured immediately after the animal was euthanized.

4.4.4 In vivo MRI Experiments

Imaging experiments were performed on a 3.0 Tesla clinical scanner (Magnetom Verio; Siemens Healthcare, Erlangen, Germany). Animal was placed in right decubitus position with body array coils wrapped centered on posterior aspect spinous process. Throughout the imaging procedures, anesthesia was maintained with isoflurane (1-3.5%).

CEST MRI was performed using a two-dimension (2D) reduced field-of-view (rFOV) TSE CEST sequence (TR/TE = 10500/10ms, 2 averages, single shot). rFOV can effectively suppress bowel motion artifacts and increase scan efficiency (112). For each IVD, images were acquired in the axial plane with a slice thickness of 3 mm, field of view of 100 x 40 mm² and spatial resolution of 0.8 x 0.8 mm². CEST saturation module consists of 39 Gaussian-shaped pulses, with a duration $t_p = 80$ ms for each pulse and an interpulse delay $t_d = 80$ ms (duty cycle=50%, total saturation duration $T_s = 6240$ ms) at saturation flip angle 900°, 1500°, 2100° and 3000° (B_1 amplitudes = flip angle/ $(\gamma t_p) = 0.73\mu\text{T}$, $1.22\mu\text{T}$, $1.71\mu\text{T}$ and $2.45\mu\text{T}$; Gaussian saturation pulse

parameters $c_1 = 0.50$, $c_2 = 0.59$). Z-spectrum was acquired with ten different saturation frequencies at ± 1.6 ppm, ± 1.3 ppm, ± 1.0 ppm, ± 0.7 ppm and ± 0.4 ppm. Scan time of the CEST experiment for each RF irradiation amplitude is ~ 6 min. B_0 field was corrected using WASSR.

T_1 -weighted MR images were acquired by an inversion recovery TSE sequence with 7 varying TI (50ms, 150 ms, 350 ms, 700 ms, 1050 ms, 1400 ms and 2000 ms). Images were acquired at the same slice position as the CEST MRI sequence (TR/TE = 6000/12 ms; 1 average; FOV = 200 x 200 mm²; spatial resolution = 0.8 x 0.8 x 3 mm³; scan time = ~ 2.5 min).

4.4.5 Data Analysis

Post processing was performed with custom-written programs in Matlab (The Mathworks, Natick, MA, USA). $CESTR_{ind}$ was calculated according to Eq. [4.1] after B_0 correction at 1.0 ppm ($Z_{lab} = Z(+1.0 \text{ ppm})$, $Z_{ref} = Z(-1.0 \text{ ppm})$). Linear regression was used to perform Ω -plot analysis between $1/CESTR_{ind}$ and $1/\omega_1^2$ to obtain the slope and intercept. The exchange rate k_{sw} and labile proton ratio f_r were calculated afterwards following Eqs. [4.3] and [4.4]. These calculations were performed pixel-by-pixel and by region of interest (ROI). The T_1 maps were obtained by pixel-by-pixel least-squares fitting of the signal equation $I = I_0[1 - (1 + \eta) \cdot \exp(-TI/T_1)]$ where I is the signal intensity, TI is the inversion time and η is the inversion efficiency. The T_2 maps were obtained by fitting the signal equation $I = I_0 \cdot \exp(-TE/T_2)$ where I is the signal intensity and TE is the echo time.

4.5 Results

4.5.1 Phantom

In Fig. 1, we evaluated the relationship between $1/CESTR_{ind}$ and $1/\omega_1^2$ in tubes with varying GAG concentration and pH values. $1/CESTR_{ind}$ is the average signal within the region-of-interest (ROI) of each tube. In all tubes, $1/CESTR_{ind}$ can be represented as a linear function of $1/\omega_1^2$. This experimental finding is consistent with Eq. [4.2]. The r^2 values of the linear regression for all tubes shown in Fig. 1 are all bigger than 0.97.

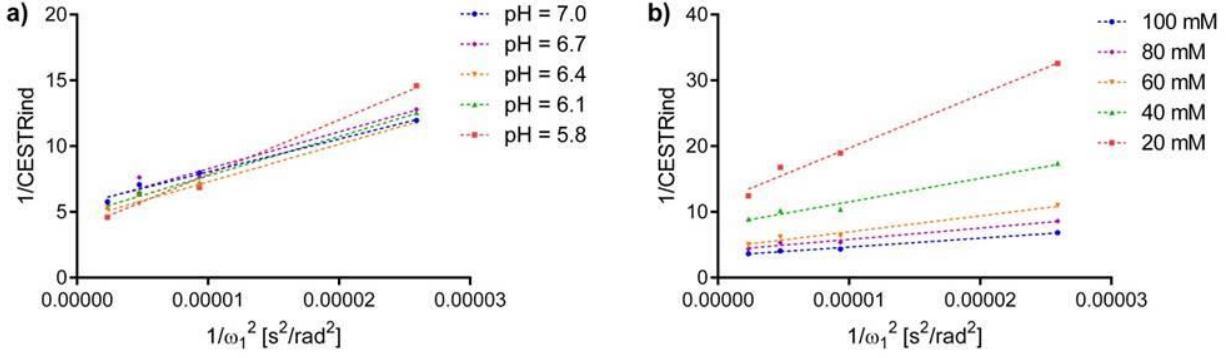


Figure 4.1 Ω -plots analysis of **(a)** phantoms with the same concentration (60 mM) but varying pH values (5.8, 6.1, 6.4, 6.7 and 7.0); **(b)** phantoms with the same pH value (7.0) but varying GAG concentration (20 mM, 40 mM, 60 mM, 80 mM and 100 mM).

In addition, pixel-wise mapping of chemical exchange rate k_{sw} and labile proton ratio f_r were reconstructed, shown in Fig. 2. One can appreciate the dependence of chemical exchange rate on pH (Fig. 2a) and labile proton ratio on GAG concentrations (Fig. 2b). Quantitatively, the chemical exchange rate can be described as $k_{sw} = 1.5e8 \times 10^{-pH} + 252.0$, $R^2 = 0.9508$ (Fig. 2c). This follows an acid catalyzed chemical exchange formula (113). The labile proton ratio is linearly correlated with GAG concentration (Fig. 2d). It can be represented as $f_r = 4.6 \times 10^{-5}[\text{GAG}] - 4.4 \times 10^{-5}$ ($R^2 = 0.9869$), where [GAG] is the GAG concentration in mM. The error bars in Fig. 2c and 2d represent the standard deviation of all the pixels within the ROI of each tube for k_{sw} and f_r , respectively. These experimental results encouraged in vivo application of qCEST technique.

4.5.2 Animal Studies

16 IVDs were studied in this work, 3 of which were excluded because the needle went through both sides of the IVD and caused morphological damage. The pH values of the studied IVDs after Na-Lactate injection ranged from 5.0 to 7.2.

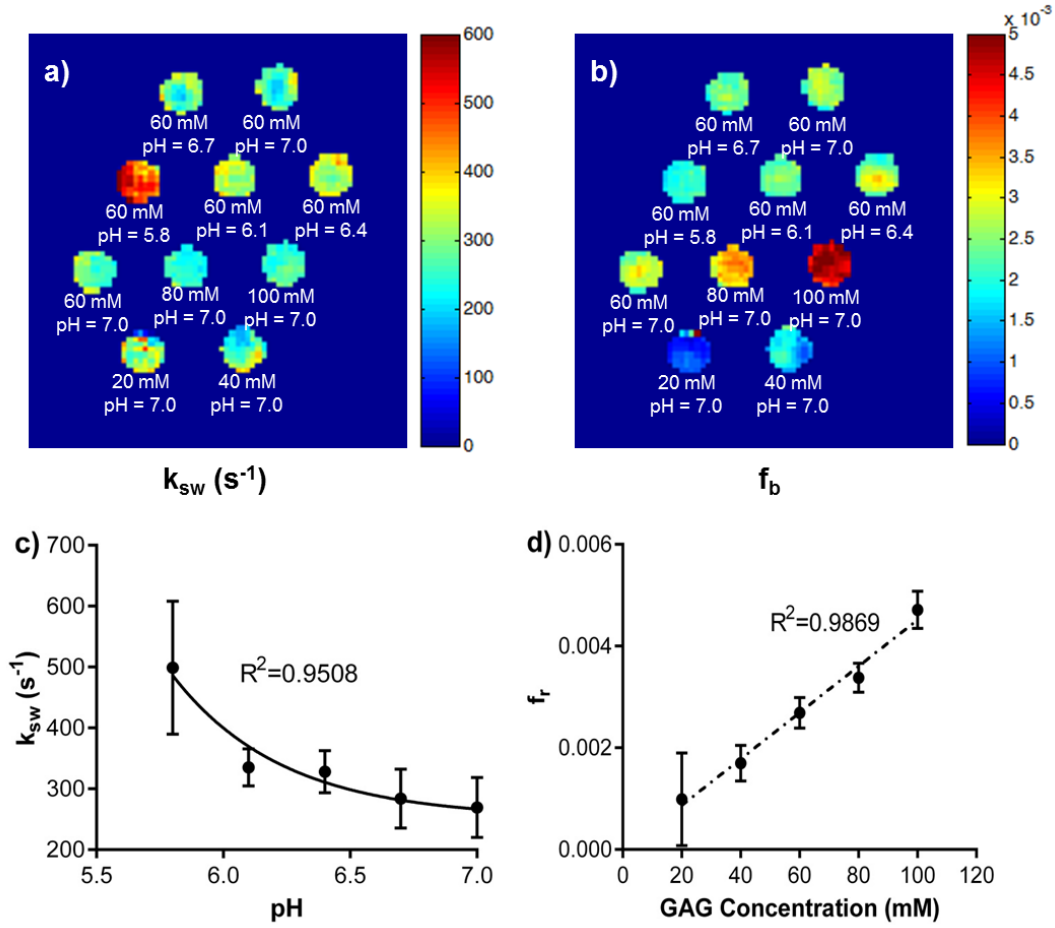


Figure 4.2 Quantitative results of the phantom study. (a) Pixel-wise mapping of labile proton exchange rate. (b) Pixel-wise mapping of labile proton ratio. (c) The chemical exchange rate as a function of pH. (d) The labile proton ratio as a function of GAG concentration. The error bars in (c) and (d) represent the standard deviation of all the pixels within the ROI of each tube for k_{sw} and f_r , respectively.

Fig. 3 shows the anatomical images of one representative mini-pig's lumbar IVDs and the corresponding exchange rate maps. As shown in the figure, the exchange rate was higher in the IVDs with lower pH values. Within each disc, there was some inhomogeneity in the exchange rate map. This is partially because the current SNR we have cannot guarantee accurate measurement for a signal pixel. However, the average value within the ROI of each IVD will provide more reliable measurement. This is because SNR will increase after averaging all pixels that are in the similar pH environment.

In Fig. 4a, we evaluated the relationship between $1/\text{CESTR}_{\text{ind}}$ and $1/\omega_1^2$ in representative IVDs with different pH values (5.0, 5.8 and 6.7). Similar as shown in phantom studies, $1/\text{CESTR}_{\text{ind}}$ can be represented as a linear function of $1/\omega_1^2$. In Fig. 4b, we took the average exchange rate of each disc, and evaluated its relationship with the corresponding pH value, which was obtained by directly measuring the intra-discal pH value using a pH probe. The exchange rate can be described by an acid catalyzed chemical exchange formula, $k_{sw} = 9.2e6 \times 10^{-\text{pH}} + 196.9$, $R^2 = 0.7883$. However, because of the difficulty to determine the location of the pH probe, there could be some uncertainty of the pH values measured by the tissue pH probe.

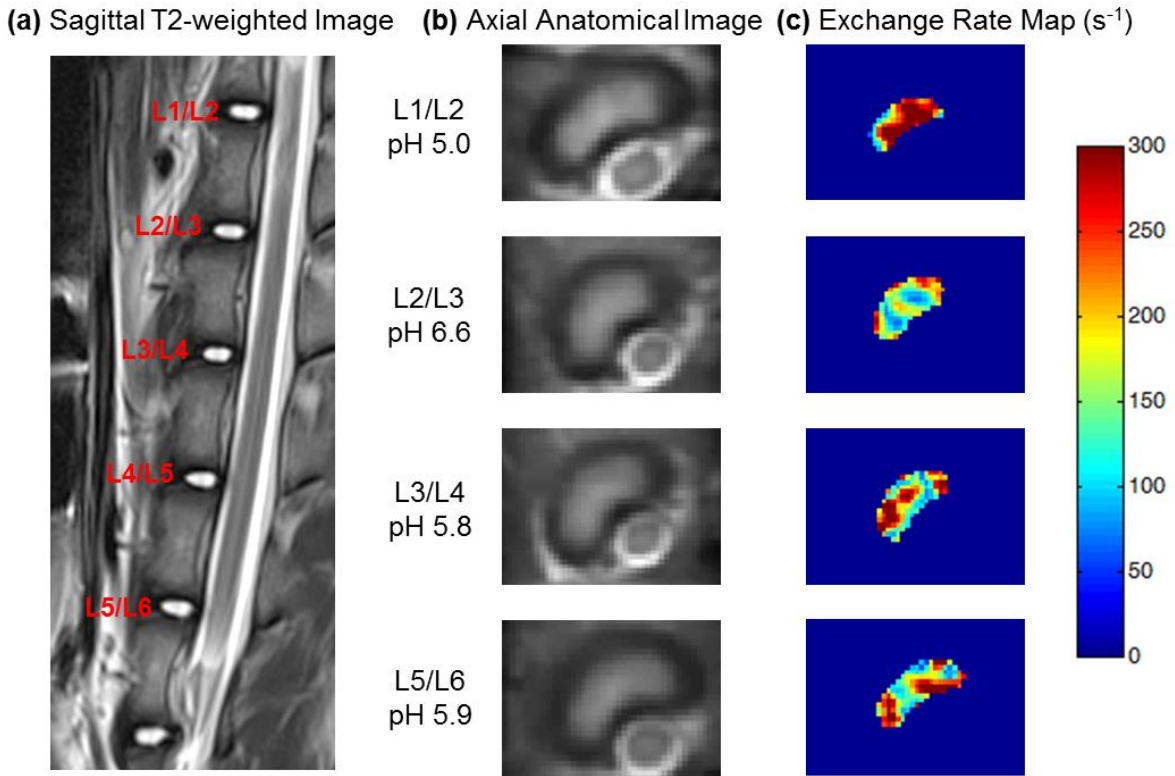


Figure 4.3 Representative images of IVDs and corresponding exchange rate maps in one mini-pig. (a) T2-weighted image in the sagittal plane. (b) Axial anatomical images of corresponding IVDs. (c) Exchange rate maps of corresponding IVDs. The IVDs with lower pH tend to have higher exchange rate.

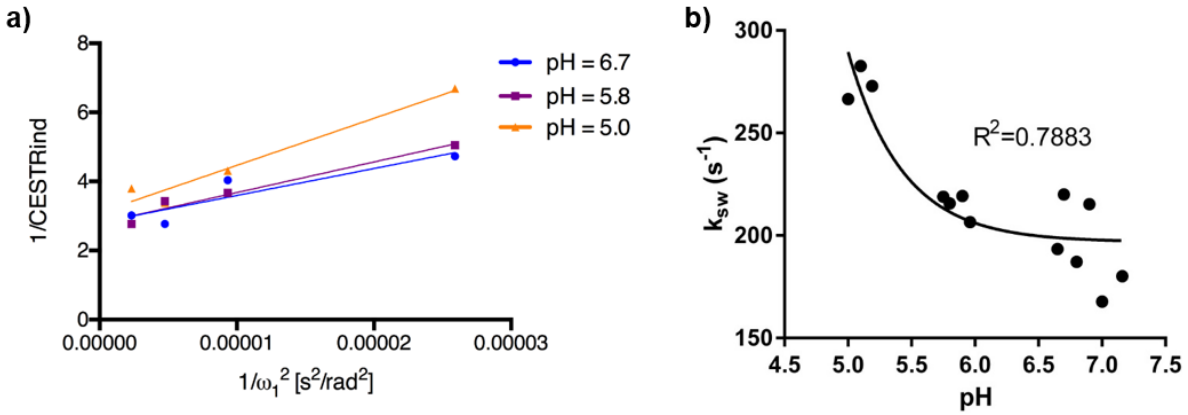


Figure 4.4 (a) Ω -plots analysis of representative IVDs with varying pH values (5.0, 5.8 and 6.7). **(b)** The chemical exchange rate as a function of pH in the animal studies.

4.6 Discussion

In this study, we investigated the feasibility of qCEST technique to detect pH changes in IVDs in vivo on a 3T MR scanner. Phantom studies showed that the approximations used in qCEST analysis hold true for GAG and the exchange rate determined from qCEST analysis is dependent on pH levels of GAG solutions. The relationship between the exchange rate and pH was further studied in the porcine spine studies. The results showed the exchange rate can be described as a function of pH using acid catalyzed proton chemical exchange formula. To our knowledge, this is the first in vivo study to show the validity of qCEST analysis using tissue pH meter as reference.

Previous studies have investigated the pH dependence of gagCEST. Even though the GAG concentration can be corrected using $T_{1\rho}$, water relaxation parameters T_1 and T_2 still contribute to the gagCEST signal (8). qCEST analysis, on the other hand, has been shown to detect pH changes independent of T_1 , T_2 and concentration in numerical simulations and in phantom studies (60,106). It is a more reliable approach to measure pH changes in the IVD, because T_1 and T_2 change significantly after disc degeneration (114). In this in vivo study, we

established a relationship between exchange rates and pH levels, which can be potentially applied in future studies to translate exchange rates to pH levels.

Pulsed CEST saturation pulses were used because this study was performed on a 3.0 Tesla clinical MR scanner. Pulsed qCEST analysis is even more complicated because of the constant changing RF irradiation amplitude. Pulsed CEST experiments normally report the irradiation power as the equivalent cw B_1 field strength. However, the proton exchange in pulsed CEST experiments is rather complicated. Simply integrating the equivalent cw B_1 field strength will cause errors in estimating the exchange rate and labile proton ratio. Meissner et al. came up with an analytical solution for pulsed CEST experiment (106). This enables more accurate quantitative results of pulsed CEST experiments.

It should be noted that because of the simplification of the in vivo situation there could be some potential systemic error in estimating the exchange rate. One error source is MT effects are not considered. This will lead to the underestimation of CEST effects, especially when the RF irradiation amplitude is higher, which means the slope can be also underestimated. Therefore, the estimation of exchange rate is underestimated because MT effects are not considered. Another error source is the approximation of the Gaussian-shaped saturation pulses. Even though we have made some corrections as discussed above, the performance of the Gaussian-shaped pulses is not fully simulated, especially in the case of intermediate to fast chemical exchange.

In this study, we explored the relationship between exchange rates and pH levels in both phantom studies and in vivo animal studies. However, the results are not exactly the same. One reason is these two studies were performed at different temperatures ($\sim 20^\circ\text{C}$ for phantom studies and $\sim 38^\circ\text{C}$ for animal studies). Another possible reason is the GAG protons in the IVD experience a more complicated environment. In addition to CEST effects, MT effects are also present in the IVD from semi-solid components such as macromolecules, which could affect the qCEST analysis (59). As discussed above, because we didn't consider MT effects in our model, there is systemic

error of underestimating the exchange rate in the in vivo studies, which explains the discrepancy between phantom and animal studies.

A potential limitation of this study is the long scan time (30~40 min for one IVD). Regular CEST experiments are relatively slow, because of long TR, multiple averages, etc. In addition to that, qCEST analysis also requires (a) long RF saturation time (6s in our study) to achieve the steady state and (b) multiple CEST experiments with varying RF irradiation amplitudes to perform the Ω -plots. Compressed sensing and parallel imaging techniques can be utilized to accelerate qCEST experiments (115).

It is known that CEST imaging is prone to B_1 inhomogeneity. Not knowing the exact B_1 field may cause errors in the estimation of exchange rate k_{sw} . In this work, we performed a pilot study and found B_1 field is relatively homogenous within the small ROI (nucleus pulposus) for all discs. That's why we did not acquire B_1 map for every IVD. It should be noted though, B_1 inhomogeneity issues need to be carefully considered in qCEST imaging to avoid potential errors.

The manipulation of pH levels in the IVDs by injecting Na-Lactate mimics the degeneration condition only to a limited extent. In addition to pH change, disc degeneration is also correlated with a loss of GAG and water content in the nucleus pulposus (116). GAG loss will significantly lower the CEST values (7) and the dehydration process will cause the change of MR relaxation parameters (117,118). In order to better simulate the degeneration situation, qCEST experiments could be performed in the disc degenerative porcine model (119) and in patients with discogenic pain (8).

4.7 Conclusions

Our work demonstrates the feasibility of in vivo qCEST analysis of GAG in IVDs. The validation study shows that the exchange rate determined from qCEST analysis is closely correlated with pH value, and can be used to non-invasively measure pH in IVDs. qCEST

technique has the potential to provide additional information on IVD physiology and help gain insight into the pathogenesis of low back pain and its underlying degenerative processes.

CHAPTER 5: Detection of Low Back Pain Using Novel MRI-Based Biomarker in a Porcine Model of Disc Degeneration

5.1 Background

Nearly everyone at some point has back pain that interferes with work, routine daily activities, or recreation. It occurs most often between ages 30 and 50, due in part to the aging process but also as a result of genetic predisposition, mechanical injuries and a sedentary life style (92,120). The risk of experiencing low back pain increases with age. Americans spend at least 50 billion dollars each year on low back pain, the most common cause of job-related disability and a leading contributor to missed work (121). Low back pain may reflect nerve or muscle irritation, bone lesions, or result from injury or trauma to the back. However, IVD degeneration is believed to be the major source for chronic back pain, and over 90% of surgical spine procedures are performed because of consequences of this degenerative process (116). Current diagnostic approaches include CT and MRI, which provide detailed soft tissue imagery, but in its current usage fail to differentiate between a pathologically painful IVD and physiologically aging IVD that does not generate pain (122,123).

In adults, the IVD is avascular and its nutrition depends on diffusion via the annulus fibrosus and the adjacent vertebral endplates(124). Typically, nucleus pulposus cells obtain energy by anaerobic glycolysis, leading to the production of lactic acid, which is then expelled from the IVD by diffusion. In degenerated IVDs, due to changes in blood supply, sclerosis of the subchondral bone or endplate calcification, the supply of glucose and clearance of lactate drops, thereby leading to a sharp drop in pH within the IVD (125,126). The pH of human IVDs ranges between 7.1 in healthy IVDs, down to values that reach below 6 in degenerated IVDs (111,127). Therefore, a recent hypothesis was made that low pH values within the degenerated IVDs are the cause of discogenic low back pain (9,98).

As discussed in Chapter 4, recent advances in MRI technologies allowed researchers to non-invasively assess changes in pH within the body. Of particular note, chemical exchange saturation transfer (CEST) has been studied to measure pH-dependent signal changes (13,101-103). This technique exploits the chemical exchange, which is pH-sensitive, between water protons and solute protons in certain molecules. Previous studies have applied CEST to detect pH changes in the IVD in pigs (9) and human patients (8). However, CEST signal is rather complicated and has multiple contributing factors. To negate these confounding factors, quantitative CEST (qCEST) was developed to measure the exchange rate, independently from T_1 , T_2 and solute concentration (59,60,104,105). In Chapter 4, it has been shown that the exchange rate measured using qCEST is closely correlated with pH values in the IVD and qCEST is feasible for in vivo pH change detection within IVDs on a clinical 3T MR scanner (128).

In the present study, we hypothesized that discogenic pain is caused by a pH drop within the degenerating IVD, and thus can be detected using qCEST in a clinically-relevant, large animal model of IVD degeneration (porcine). Changes in the expression profile of several pain markers were also examined in vivo in relation to the degenerative processes and changes in pH within the IVD.

5.2 Method

5.2.1 Study Design

The objective of our study was to develop a pH-level dependent MR imaging approach to diagnose low back pain. Our pre-specified hypothesis was that pain in the degenerating IVDs is caused at least partially due to an intra-discal acidic environment, and this pH drop can be detected non-invasively using qCEST imaging. Nine healthy female skeletally mature Yucatan minipigs (S&S Farms; Average age 1.5 years, 35–40 kg) were included in this study. The sample size used was estimated to achieve a power of 0.8 and $\alpha = 0.05$ using one-way ANOVA. qCEST was investigated for its capacity to detect any pH changes within the IVDs, and see whether this

change can be correlated to pain marker upregulation. For this purpose, we created an IVD degeneration model in a large, clinically-relevant animal model by puncturing the annulus fibrosus with a 14 G needle, thus creating four degenerating IVDs per minipig (Fig. 1). Then, the minipigs went through MRI scan at 2, 6 and 10 weeks after degeneration. At each time-point, three pigs were randomly euthanized in order to directly measure the pH within the IVD using pH meter, and the degenerated IVDs were harvested for gene expression analysis, histology and immunofluorescence. IVD degeneration was evaluated using imaging parameters and histology. Pain was detected using gene expression and immunofluorescence, and was compared qCEST measurements within the IVDs. Animals that developed acute procedural complications such as nerve damage or signs of distress during follow-up that compromised animal welfare were eliminated from the study.

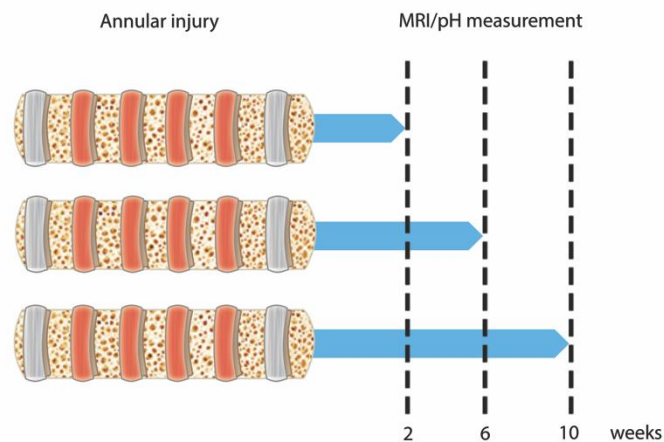


Figure 5.1 IVD degeneration timeline. Minipigs underwent annular injury in four IVD levels to induce degeneration (denoted by red color). Following degeneration, animals were randomly divided into 3 groups and scanned at 2, 6 and 10 weeks. At each time point, one of the groups was sacrificed and the pH within the injured IVDs was measured. The IVDs were harvested for gene analyses and histology.

5.2.2 IVD Degeneration Animal Model

All animal procedures were approved by the Cedars-Sinai Medical Center institutional review board for animal experiments. The IVD degeneration model was created with modifications from a previously established method (129). Following an 18- hour preoperative fast, each minipig

was sedated using intramuscular acepromazine (0.25 mg/kg), ketamine (20 mg/kg), and atropine (0.02–0.05 mg/kg). The animal was then administered propofol (2 mg/kg) intravenously and endotracheal intubation was performed. Anesthesia was maintained using 1– 3.5% inhaled isoflurane for the duration of the procedure. In order to induce IVD degeneration, a single annular injury was performed, as it was found the most reliable and reproducible method compared to nucleus aspiration or injection of apoptotic agents (119). Under fluoroscopic guidance, a 14 G Verteport needle (Stryker, Kalamazoo, MI) was used to penetrate and injure the annulus fibrosus of the IVD parallel to the endplate via a posterolateral approach. This procedure was repeated at four target levels: L1/L2, L2/L3, L3/L4 and L4/L5.

5.2.3 In vivo MRI

Imaging experiments were performed on a 3T clinical scanner (Magnetom Verio; Siemens Healthcare, Erlangen, Germany). Animals were placed in the right decubitus position with body array coils centered on the posterior aspect spinous process. Throughout the imaging procedures, anesthesia was maintained with isoflurane (1%– 3.5%).

CEST MRI was performed using a two-dimensional reduced field of view TSE CEST sequence (TR/TE 1/4 10,500/ 10 ms, two averages, single shot). For each IVD, images were acquired in the axial plane with a slice thickness of 3 mm, field of view of $140 \times 40 \text{ mm}^2$, and spatial resolution of $1.1 \times 1.1 \text{ mm}^2$. CEST saturation module consists of 39 Gaussian-shaped pulses, with a duration $t_p = 80 \text{ ms}$ for each pulse and an interpulse delay $t_d = 80 \text{ ms}$ (duty cycle = 50%, total saturation duration $T_s = 6240 \text{ ms}$) at saturation flip angle 900° , 1500° , 2100° , and 3000° (B_1 amplitudes = flip angle/ (gt_p) = 0.73, 1.22, 1.71, and $2.45 \mu\text{T}$). Z-spectrum was acquired with 10 different saturation frequencies at ± 1.6 , ± 1.3 , ± 1.0 , ± 0.7 , and $\pm 0.4 \text{ ppm}$. The scan time of the CEST experiment for each IVD was approximately 40 min. The B_0 field was corrected using a water saturation shift referencing (WASSR) map (5).

T₁ mapping was performed using an inversion recovery TSE sequence with seven varying TI (50, 150, 350, 700, 1050, 1400, and 2000 ms). Other imaging parameters are: TR/TE = 6000/12 ms; FOV = 280 × 280 mm²; spatial resolution = 1.1 × 1.1 × 3 mm³.

T₂ mapping was performed using a TSE sequence with varying echo delays (TE = 12, 25, 50, 99, 199 and 397ms; TR = 6000 ms). Other imaging parameters are: TR = 6000 ms; FOV = 280 × 280 mm²; spatial resolution = 1.1 × 1.1 × 3 mm³.

T_{1ρ} mapping was performed using a rFOV TSE sequence with varying spin lock times (TSL = 0, 10, 40 and 80 ms). The spin-lock frequency is 300 Hz. Other imaging parameters are: TR/TE = 3500/9.1 ms; 1 average; FOV = 140 × 40 mm²; spatial resolution = 1.1 × 1.1 × 3 mm³). Image analysis was performed with custom-written programs in MATLAB (MathWorks, Natick, Massachusetts, USA) as previously reported (128).

5.2.4 IVD pH Measurement

Measurements of the pH inside the IVD were done immediately following animals' sacrifice. The spine was surgically exposed and a custom-made needle-shaped tissue pH probe (Warner Instruments, Hamden, Connecticut, USA) was inserted to the nucleus pulposus of the injured IVDs through a fine-cut incision of the annulus fibrosus.

5.2.5 Gene Expression Analysis

A quantitative RT-PCR was conducted on degenerated IVDs harvested at 2, 6 and 10 weeks after degeneration. Total RNA was extracted from the annulus fibrosus and the nucleus pulposus by using RNeasy Mini kit (Qiagen GmbH, Hilden, Germany) according to the manufacturer's protocol. RNA was retrotranscribed using random primers and reverse transcriptase (Promega Corp., Madison, WI, USA). Quantitative real-time PCR was performed with the aid of ABI7500 Prism system (Applied Biosystems, Foster City, CA). The genes studied were Bradykinin receptor B1 (BDKRB1; Ss03389804_s1), calcitonin gene-related peptide (CGRP; Ss03386432_uH) and catechol-O-methyltransferase (COMT; Ss04247881_g1) to detect pain

marker upregulation, interleukin-6 (IL-6) to examine the inflammatory response and brain-derived neurotrophic factor (BDNF) to determine nerve growth. 18s was used as a housekeeping gene control.

5.2.6 Histological Analysis and Immunofluorescence Imaging

Histological analysis was performed on degenerated IVDs harvested at 2, 6 and 10 weeks after degeneration. The IVDs were sectioned and stained using hematoxylin and eosin for morphological analysis, as previously described (130). For immunofluorescent staining, tissues were deparaffinized, and the antigens were retrieved by incubation in preheated Target Retrieval Solution (Dako, Carpinteria, CA) for 45 minutes in 37 °C. Nonspecific antigens were blocked by applying blocking serum– free solution (Dako). Slides were stained with primary antibodies against BDKRB1, CGRP, COMT, IL-6 and BDNF. The primary antibodies were applied to the slides and incubated in 4 °C overnight, washed off using PBS, and the slides were incubated with secondary antibodies for 1 hour in room temperature, after which they were washed off with PBS (Supplementary table S1). Slides were then stained with 4',6-diamidino-2-phenylindole dihydrochloride (1 µg/ml) for 5 minutes in the dark, after which they were again washed three times with PBS. A VectaMount mounting medium (Vector Laboratories, Burlingame, CA) was applied to the tissue. The slides were imaged using a four-channel Laser Scanning Microscope 780 (Zeiss, Pleasanton, CA) with ×20 magnification, z-stacking, and 5 × 5 tile scanning. For zoom-in images, a single z-stacked image was generated. All samples were scanned using the same gain and exposure settings.

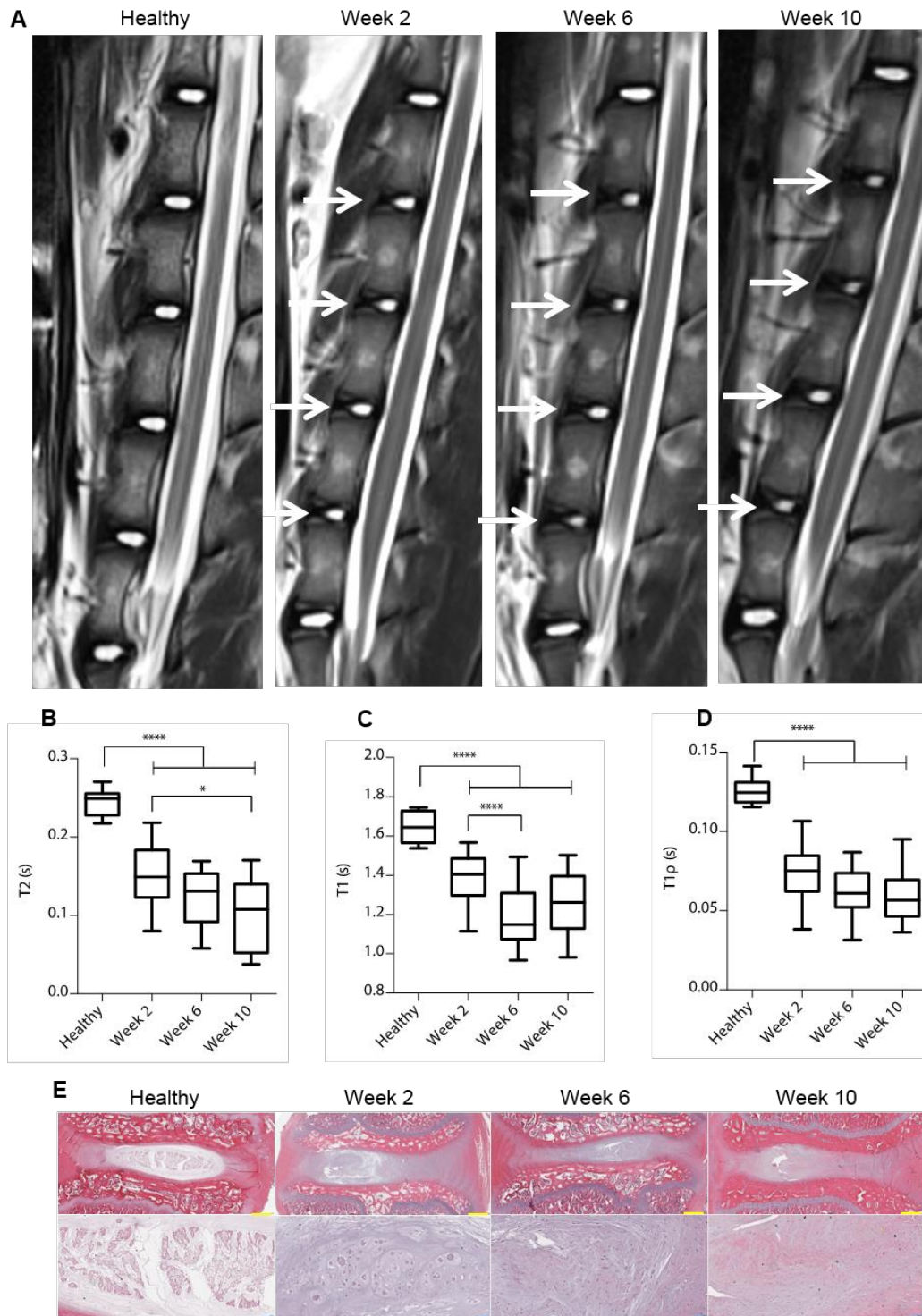


Figure 5.2 IVD degeneration following intra-discal puncture.

5.2.7 Statistical Analysis

GraphPad Prism 5.0f software (GraphPad Prism, San Diego, CA) was used to analyze the data. Results are presented as means \pm SE. Data analysis was conducted using a repeated measures one-way ANOVA or a two-way ANOVA with Tukey's multiple comparison post hoc test. To assess significance, $p < 0.05$ was considered statistically significant.

5.3 Results

5.3.1 Induction of IVD Degeneration

Minipigs underwent surgery during which the annulus fibrosus of four IVDs (L1/2-L4/5) were punctured to induce degeneration (Fig. 5.1). The progress of IVD degeneration was monitored using MRI, with a clear decrease in the intensity of the T_2 -weighted signal in punctured IVDs compared to healthy IVDs (Fig. 5.2A). A two-fold decrease in water content within the punctured IVDs was evident as soon as 2 weeks after induction of degeneration compared to healthy porcine IVDs based on T_2 -weighted mappings ($p < 0.0001$; Fig. 5.2B). The water content was further reduced 10 weeks after induction of degeneration compared to week 2 ($p < 0.05$). In addition, a significant reduction of T_1 signal from 1.6 to 1.4 was noticeable at 2 weeks after induction of degeneration compared to healthy controls ($p < 0.0001$; Fig. 5.2C). Further reduction of T_1 signal to 1.2 was measured 6 weeks after induction of degeneration ($p < 0.0001$). $T_{1\rho}$ mapping revealed two-fold reduction in signal as soon as 2 weeks after induction of degeneration ($p < 0.0001$; Fig. 5.2D). Overall, these quantitative signals show the rapidly progressive degenerative status of the punctured IVDs (131,132). Histology revealed an abnormal IVD structure and cell matrix following puncture, with extensive fibrosis and formation of cell clusters in the nucleus pulposus, typical of degenerated IVDs (Fig. 5.2E)(133).

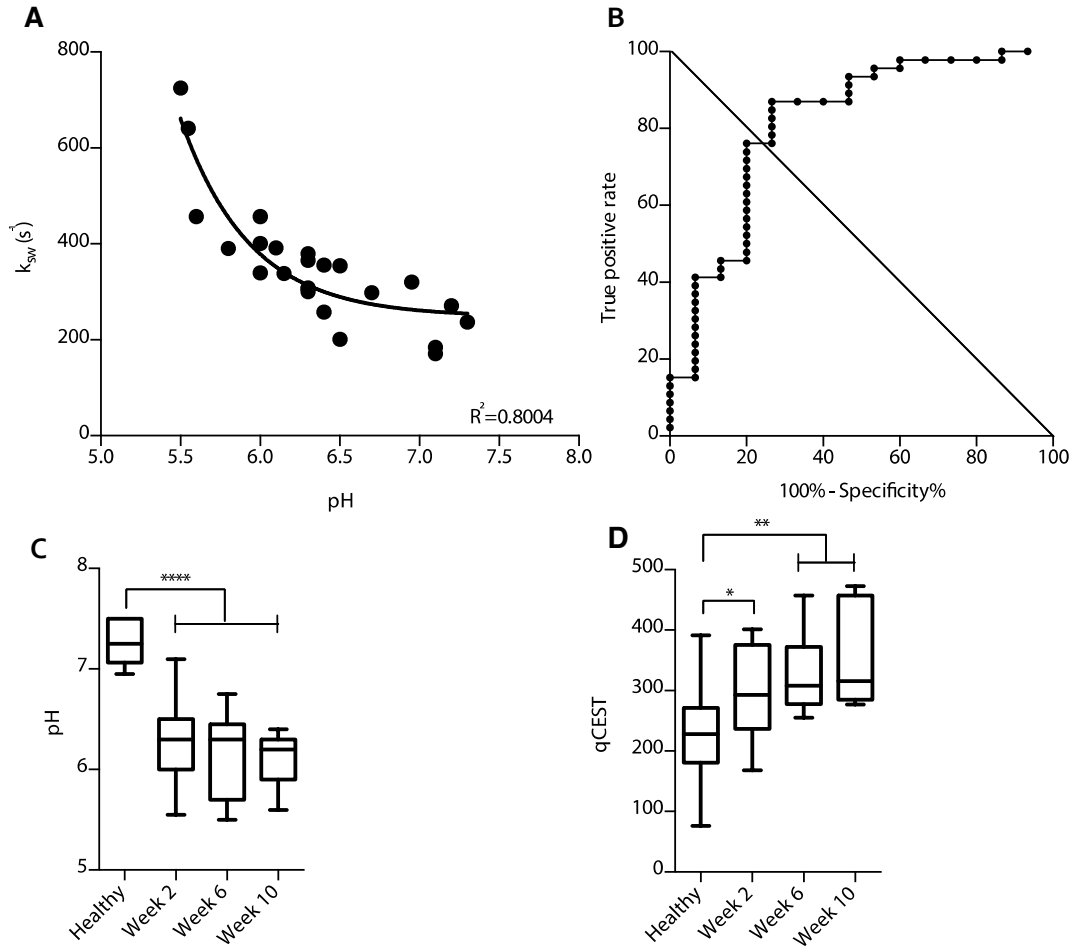


Figure 5.3 pH and qCEST changes following IVD degeneration. (A) Correlation between the qCEST signal represented by the exchange rate between solute pool and water pool (k_{sw}) and the pH measured within the IVD following animal sacrifice. (B) ROC curve analysis of qCEST signaling for the detection of degenerating IVDs. (C) pH and (D) qCEST measurements within the degenerating IVDs at 2, 6 and 10 weeks after degeneration. (n=12 per experimental group; *p < 0.05, **p < 0.01, ****p = 0.0001; qCEST= quantitative chemical exchange saturation transfer).

5.3.2 MR Signal Correlates with Intra-Discal pH in Degenerated IVDs

In addition to measuring the degenerative status of the IVDs, qCEST signals were acquired from the degenerative IVDs. These values were correlated to their correspondent pH readings that were measured directly from the IVDs (Fig. 5.3A). Strong correlation was observed between the qCEST signal and pH of the degenerated IVDs ($R^2 = 0.8004$; $p < 0.0001$). The available qCEST readings at weeks 2, 6 and 10 were classified as either healthy or degenerated and used to create an ROC curve (area under the curve = 0.813, $p = 0.0003$) with 81.3%

sensitivity and 76.1% specificity (Fig. 5.3B). Significant pH drop from 7.2 to 6.3 was measured in IVDs as soon as 2 weeks after injury ($p = 0.0001$, Fig. 5.3C). This reduction in pH was maintained until week 10. In accordance with the pH drop, the acquired qCEST signal significantly increased 2 weeks after injury ($p < 0.05$, Fig. 5.3D). Further increase in signal was observed at 6 and 10 weeks ($p < 0.01$), demonstrating high sensitivity of the MR protocol to small changes in pH that were not statistically significant by physical measurements.

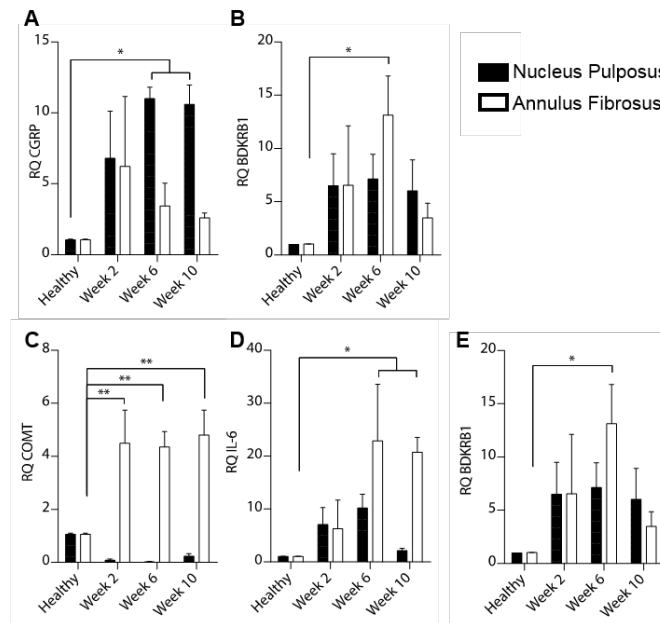


Figure 5.4 Pain and inflammatory markers upregulation in degenerating IVDs. Quantitative RT-PCR analysis of (A-C) pain-related genes (CGRP, BDKRB1 and COMT), (D) IL-6 and (E) BDNF harvested from the annulus fibrosus and nucleus pulposus of degenerated IVDs at 2, 6 and 10 weeks after induction of degeneration.

5.3.3 MR Signal Correlates with Pain-Markers in Degenerated IVDs

Next, we evaluated the expression of pain-related factors in the degenerated IVDs. Harvested degenerated IVDs underwent gene expression analysis of RNA that was extracted from the nucleus pulposus and annulus fibrosus. Specifically, we evaluated the expression of bradykinin receptor B1 (BDKRB1), calcitonin gene-related peptide (CGRP) and catechol-O-methyltransferase (COMT). A 10-fold increase in CGRP expression was observed in the nucleus pulposus 6 and 10 weeks after degeneration ($p < 0.05$, Fig. 5.4A). A 13-fold increase in BDKRB1

expression was observed in the annulus fibrosus 6 weeks after degeneration ($p < 0.05$), while a non-significant decrease was observed 10 weeks after degeneration ($p = 0.1367$, Fig. 5.4B). There was a 4-fold increase in COMT expression in the annulus fibrosus at 2, 6 and 10 weeks after degeneration ($p < 0.01$, Fig. 5.4C). In addition, expression of IL-6, which is involved with inflammatory processes, were also assessed following degeneration. IL-6 expression analysis revealed 20-fold increase in the annulus fibrosus at 6 and 10 weeks after degeneration ($p < 0.05$, Fig. 5.4D). We also evaluated the expression of brain-derived neurotrophic factor (BDNF), which is involved with nerve growth. A 22-fold increase in BDNF expression in the annulus fibrosus was observed at 6 weeks after degeneration ($p < 0.05$, Fig. 5.4E). Surprisingly, a non-significant downregulation was observed in the annulus fibrosus 10 weeks after degeneration ($p = 0.0925$), while a significant 18-fold increase was observed in the nucleus pulposus during that time ($p < 0.05$). Finally, the measured qCEST signals were paired with the expression levels of the aforementioned markers derived from the same IVDs, resulting in strong linear correlations ($p < 0.0001$ for all pairings; Fig. 5.5). Combined with our previous results, this data demonstrates that an increase in qCEST signal is correlated with an upregulation of several pain markers within the IVDs, and therefore enables detection of painful IVDs.

5.4 Discussion

In this study, we used MRI to detect discogenic low back pain in a minipig model of IVD degeneration. We showed that degeneration was achieved by 10 weeks following injury, as detected by MRI and histology. A significant pH drop was observed during the degenerative process, as well as a significant increase in the qCEST signal. These changes were detected as early as 2 weeks after injury. qCEST signals were well-correlated with pH measurements obtained directly from the degenerated IVDs. Gene analysis revealed upregulation of several pain markers in degenerated IVDs, and this upregulation was strongly correlated to the increase in qCEST signal at various time points.

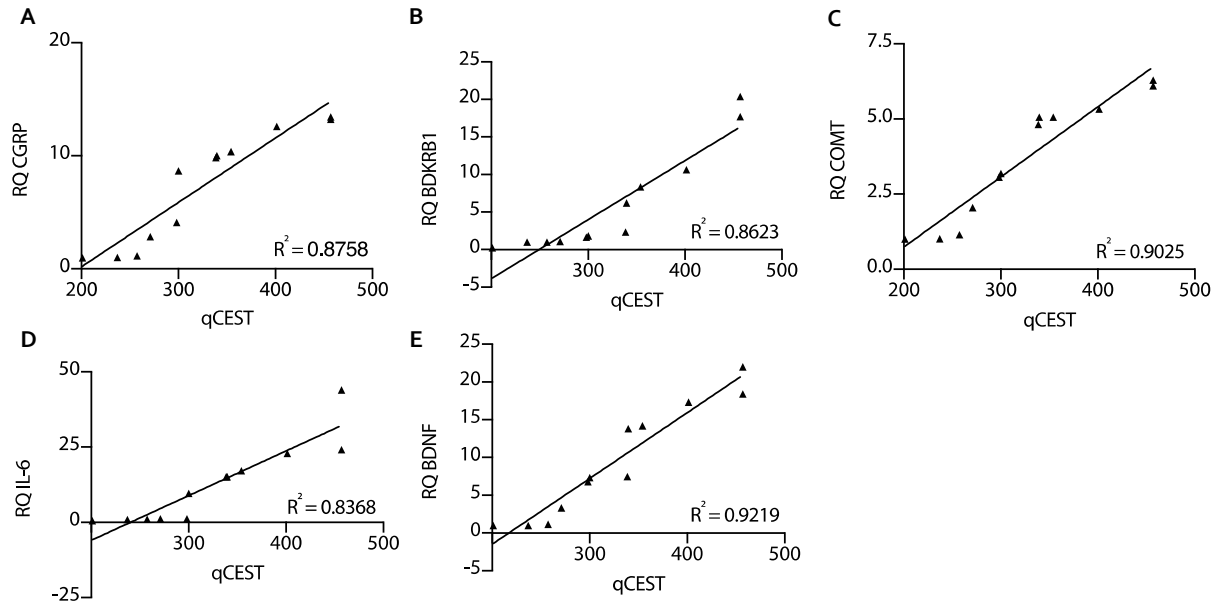


Figure 5.5 Linear correlation between qCEST and biomarkers in degenerating IVDs. Correlation curves between qCEST signal and corresponding expression of (A) CGRP, (B) BDKRB1, (C) COMT, (D) IL-6 and (E) BDNF extracted from degenerated and healthy IVDs.

Quantitative MR sequences offer new objective markers of evaluation of healthy and injured IVDs. Conventional quantitative protocols of T_1 -, T_2 -relaxation, and more recently $T_{1\rho}$ mapping, are well-established in the literature and allow detection of pathological changes within the IVDs(122,134-137). Of particular interest, $T_{1\rho}$ was compared to discography as a quantitative biomarker of low back pain(138). This study demonstrated that loss of proteoglycans, as shown by reduced $T_{1\rho}$ signal, can be used to detect painful IVDs. However, its moderate correlation to discography stems from the relatively low specificity of the method, as loss of proteoglycans is a common feature of IVD degeneration and doesn't necessarily correlate to pain symptoms (126). In addition, performing the discography procedure immediately before the MRI raises the question whether contrast injection might have affected the measured $T_{1\rho}$ signal within the IVD due to increased water content. Newer methods utilizing gagCEST imaging protocols to evaluate GAG content were also tested to detect low back pain. Wada *et al.* showed that there is a correlation between gagCEST signal and Pfirrmann score in patients with low back pain ($r = -0.675$) (139). A similar work utilizing the same approach showed weaker correlation in patients ($r = -0.449$) (7).

While no direct correlation to pain scoring was shown in both works, gagCEST signal is affected from several other factors, including T_1 and T_2 relaxation and collagen content, making this approach less reliable (26,112). Although loss of GAGs occurs early in degenerative processes of the IVD and can therefore be used as a marker of IVD degeneration (126), no causative relationship has been shown between GAGs depletion and discogenic low back pain.

One hypothesis to explain the pathogenesis of low back pain is low pH in the IVD. Several works have shown that cells isolated from degenerated IVDs over-express and secrete several pain-related and neurotrophic factors that enhance nerve growth, including BDNF and nerve growth factor (NGF) (140-142). In addition, conditioned medium from degenerate IVD cells promoted increased neurite outgrowth in nerve cells (140). There is evidence that in degenerative IVDs, the number of nerve fibers at the outer layer of the annulus fibrosus increases and nerve fibers grow into the inner parts of the annulus and occasionally even into the nucleus pulposus, parts that are otherwise not innervated in healthy individuals (143-145). The drop in pH could irritate the locally infiltrated nerve fibers, which in turn trigger discogenic pain. In our degeneration model, we observed over-expression of BDNF in the annulus fibrosus 6 weeks after degeneration, followed by expression of BDNF in the nucleus pulposus at 10 weeks. This pattern of inward expression suits the reports that observed nerve fiber penetration into the nucleus pulposus. A recent study showed that acidic pH directly causes the increase in several pro-inflammatory, neurotrophic and pain-related factors in cultured human nucleus pulposus cells, including IL-6 and BDNF, in a similar fashion to our findings (146). This upregulation may be responsible for the in-growth of nerve fibers into the degenerate IVDs, and low pH is a contributing factor to this process.

Acid sensing ion channels (ASICs), extracellular receptors that respond to low pH, were found to be upregulated after exposure to acidic environment in nucleus pulposus cells and regulate biological activity of the cells (147-149). ASIC3 was found to protect IVD cells from apoptosis in low pH conditions (149). In the same study, it was shown that NGF is required to

maintain a basal level of ASIC3, thus it is conceivable that IVD cells secrete nerve growth factor to protect themselves from the acidic environment in the IVD and indirectly activate pain fibers in this process. Several works inhibited the activity of ASICs in nucleus pulposus cells, showing reduction in the expression of pro-inflammatory, neurotrophic and pain related factors in acidic environment (146,150). Hence, although the mechanism remains elusive, these findings indicate a close relationship between low pH and discogenic pain.

One of the biggest challenges in using animals to study IVD degeneration relates to pain perception. Gruber *et al.* conducted a genome-wide analysis from IVD specimens of human patients to examine key pain-related genes associated with discogenic pain (151). Similar to our findings, his work showed upregulation of CGRP, COMT and BDKRB1 in pathological IVD specimens, which was confirmed by positive immunohistochemical stainings in the annulus. These pain-related factors mediate hyperalgesia in chronic inflammation (152), stimulate sensory nerves in inflamed tissues (153), and participate in metabolism of pain neurotransmitters, including noradrenalin, adrenaline and dopamine (154). CGRP upregulation was also observed in an acute injury model of the IVD, and is affected by the expression of neurotrophic genes (155). Thus, our findings serve as a biological clue that our degeneration model causes discogenic pain in the experimental animals.

Other studies have attempted to evaluate pH as a measure for diagnosing discogenic low back pain. Zuo *et al.* demonstrated the feasibility of acquiring localized ^1H spectra on a 3.0T scanner on intact bovine and human cadaveric IVDs to quantify lactate, which causes low pH (156). Translating this technique to in vivo spectroscopy suffers from several limitations. As stated by the authors, it is difficult to differentiate lactate from the lipid peaks, because their resonance frequencies are close. Another limitation is inadequate quantification of metabolites in IVDs within the collapsed space. A later study from the same group characterized IVD in vivo by spectroscopy (157). A significant elevated water/proteoglycan area ratio was found in IVDs with positive discography. In vivo MRS is challenging because of low SNR, physiological motion, and bone

susceptibility induced line broadening, making the assessment of lactate imprecise. Another study found a non-linear dependence of the CEST effect of GAG on pH in porcine IVD specimens (9). However, the study was performed ex vivo at 7.0T MRI and the effectiveness of the method on clinical MR systems (1.5 or 3.0T) has not been shown.

While we followed the animals for up to 10 weeks after degeneration, the degenerative processes in humans can take many years and may persist for a long time before causing pain. In this study, we observed a pH drop with up-regulation of several pain markers in all of the injured IVDs which persisted for 10 weeks. A long-term study is required to fully assess the validity of this approach under chronic conditions of IVD degeneration. In addition, as opposed to our findings, IVD degeneration doesn't always lead to discogenic pain in patients, with many of them being asymptomatic. We would expect that by 10 weeks the acute changes caused by the method of degeneration induction would dissipate, contributing our findings to the degenerative processes alone. Seeing as our degeneration method led to positive pain markers in all specimens, perhaps some of our findings can be also partially attributed to the method of degeneration induction. Future studies should evaluate and compare these findings to human patients suffering from progressive degenerative IVD disease.

Overall, these results show great promise for future human studies, as this approach can be implemented on clinical MRI systems. qCEST technique can be used to provide additional information on IVD physiology and detect pH changes associated with early degeneration, thus provide early diagnosis to patients. This approach has the potential to allow earlier interventions for IVD degeneration and prevention of chronic low back pain.

CHAPTER 6: CEST-Fingerprinting: Towards Full Quantification of Exchange Rate in the Presence of Magnetization Transfer Effects

6.1 Background

CEST imaging is based on the chemical exchange between solute protons and water protons. The chemical exchange rate is affected by pH and temperature. Therefore, CEST signal is pH-sensitive. Previous studies have applied CEST imaging to detect acidosis-based ischemic penumbra (13,22,103) and tumor acidosis (158-160). However, CEST contrast can be affected by multiple confounding factors, including solute concentration, water relaxation parameters T_1 and T_2 . Some of these parameters also change dramatically in the process of disease. In some cases, the change of CEST signal has multiple origins (161,162).

Attempts have been made to quantify CEST effect by measuring the exchange rate and proton fraction ratio (the ratio of solute protons and water protons). These methods repeat the CEST experiments multiple times with different CEST saturation time or CEST saturation power and fit the exchange rate and proton fraction ratio to the Bloch-McConnell equation. Due to the complexity of the equation, fitting to the numerical solutions can be computationally expensive. Previous methods were developed based on the approximate analytical solutions, including QUEST and QUESP (58), ratiometric CEST (105,163,164) and quantitative CEST with omega plot (59,60,106,108). These methods have been applied in some preclinical studies (33,59,128).

However, there are still some challenges to accurately and efficiently quantify CEST effects. (a) The scan time is too long. This is because the long TR is needed for full longitudinal magnetization recovery and long CEST saturation time is needed for the chemical exchange to reach steady state of chemical exchange to satisfy the approximate analytical solution. (b) Some of the approximations have limited applicability. For lower fields such as 3T scanners, or protons with small chemical shift, these approximations might not hold true, which could potentially lead

to some error (58,60,106). (c) The accuracy of the current CEST quantification methods will be affected by the competing MT effects in in vivo studies(58,106). However, MT correction remains a challenging problem in CEST imaging.

MR fingerprinting is a new method that provides an alternative way to perform multi-parametric mapping (165). Instead of using a repeated, serial acquisition of data to fit to a particular equation, it uses a pseudorandomized acquisition to create unique signal evolutions for different tissue properties. The acquired signal will be matched to a pre-defined dictionary to determine the best-fit parameters. This means MR fingerprinting can detect the signal changes of a complex multi-parametric system without the need of explicit analytical solutions.

Similar ideas can be applied in CEST imaging, where CEST saturation time and saturation power are pseudorandomized to generate unique CEST signal evolution. The acquired signal can be matched to a pre-defined dictionary instead of fitting to the Bloch-McConnell equation. This can potentially address the challenges mentioned above. (a) Scan time can be significantly reduced. This is because CEST fingerprinting is not based on the analytical solution. This eliminates the need for long TR and long CEST saturation time. (b) CEST fingerprinting can be applied in more systems with more accurate measurements. This is because there are no approximations in the dictionary generation or the signal matching process. (c) MT effects can be addressed in the framework of CEST fingerprinting. The simulated dictionary can serve as signal curve when there are no MT effects. Comparing the dictionary to the acquired signal provides a chance to correct for MT effects.

In this study, we proposed CEST fingerprinting technique for exchange rate quantification in the presence of MT effects. This technique utilized CEST saturation with varying saturation power B_1 amplitude and saturation time to create uniqueness of signal evolution for different exchange rates. Preliminary studies were performed in phantoms.

6.2 Method

6.2.1 Pulse Sequence Design

Fig. 6.1a illustrates the acquisition sequence diagram of CEST fingerprinting. In each subsequent acquisition block, identified by acquisition index, the parameters of CEST preparation modules, RF irradiation power B_1 and CEST saturation time, are varied in a pseudorandom pattern. The readout was performed in the gap between CEST saturation blocks and the gap time is fixed.

Fig. 6.1b and 6.1c represent example series of the RF irradiation power B_1 and CEST saturation time. B_1 ranges from 0 to 2 μT , while CEST saturation time ranges from 0 - 1.5 s. The B_1 and saturation time series shown here are optimized for the amine protons of creatine used in the phantom studies when the field strength is 3T. For any molecule or any system, the sequence parameters can be determined with the following optimization process. (i) B_1 was randomly chosen in the range with minimal spillover effects; (ii) For each acquisition index, according to the corresponding B_1 , CEST saturation time was determined as when the CEST signal has reached certain ratio (for example, 0.5) of the steady state CEST signal. This optimization process ensures that enough CEST signal can be generated in an efficient way because CEST signal grows most rapidly in the beginning of CEST saturation.

To show the generality of CEST fingerprinting, Gaussian-shaped saturation pulses are used in this study. However, CEST fingerprinting can also be easily applied to continuous-wave saturation pulses, which are mostly used in small-animal scanners.

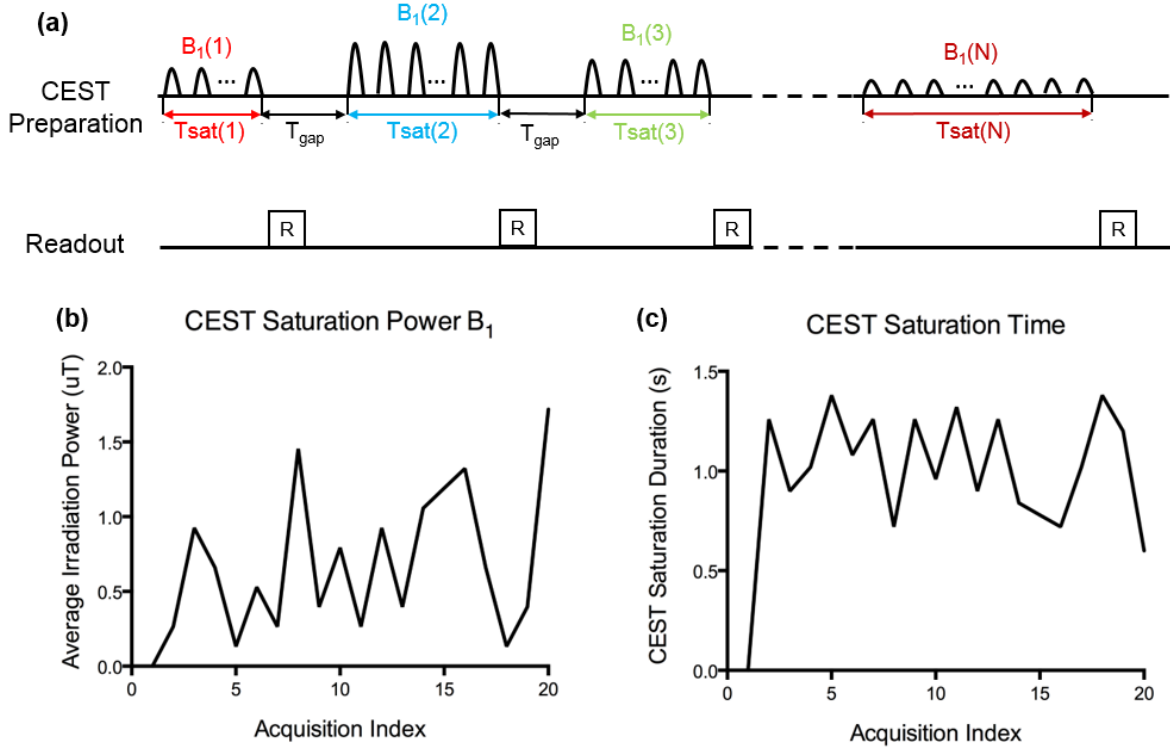


Figure 6.1 CEST fingerprinting sequence pattern. (a) Acquisition sequence diagram. In each subsequent acquisition block, RF irradiation power B_1 and duration of the CEST preparation module are varied in a pseudorandom pattern. (b, c) Examples of average RF irradiation power B_1 and CEST saturation used in this study.

6.2.2 Dictionary

With known T_1 and T_2 values, dictionary was simulated following two-pool Bloch-McConnell equations.

$$\begin{aligned} \dot{\vec{M}} &= \mathbf{A} \cdot \vec{M} + \vec{C}, \quad \mathbf{A} = \begin{bmatrix} \mathbf{L}_w - f_r \mathbf{K} & +\mathbf{K} \\ +f_r \mathbf{K} & \mathbf{L}_s - \mathbf{K} \end{bmatrix} \\ \mathbf{L}_i &= \begin{bmatrix} -R_{2i} & -\Delta\omega_{0i} & 0 \\ +\Delta\omega_i & -R_{2i} & +\omega_1 \\ 0 & -\omega_1 & -R_{1i} \end{bmatrix}, \quad i = w, s \\ \mathbf{K} &= \begin{bmatrix} k_{sw} & 0 & 0 \\ 0 & k_{sw} & 0 \\ 0 & 0 & k_{sw} \end{bmatrix} \\ \vec{C} &= [0 \quad 0 \quad R_{1w}M_{0w} \quad 0 \quad 0 \quad R_{1w}M_{0s}] \end{aligned} \quad [6.1]$$

M_{0w} and M_{0s} are the equilibrium magnetization for water protons and solute protons, respectively. f_r is the labile proton fraction ratio M_{0s}/M_{0w} . k_{sw} is the exchange rate between the solute protons to water protons. R_{1w} , R_{2w} , R_{1s} and R_{2s} are the relaxation parameters for water protons and solute protons, respectively. ω_1 is the RF irradiation amplitude. $\Delta\omega_{0w}$ and $\Delta\omega_{0s}$ is the frequency offset from water resonance and solute resonance δ_s , respectively.

Dictionary was simulated at the resonant frequency of solute protons ($\Delta\omega = \delta_s$). For each T1, T2 combination, a total of 500 signal time courses, each with 20 time points, with different exchange rates from 10 s^{-1} to 500 s^{-1} with an interval of 10 s^{-1} were simulated for the dictionary. Reference dictionary was defined as the entry simulated at the opposite frequency ($\Delta\omega = -\delta_s$).

6.2.3 MT Correction

Fig. 6.2 illustrates the framework of MT correction with CEST fingerprinting. Fig. 6.2a compares the reference dictionary (dictionary simulated at the opposite frequency $\Delta\omega = -\delta_s$) and the reference signal (data acquired at the opposite frequency $\Delta\omega = -\delta_s$). In a perfect water-solute 2-pool system (such as phantom group 1), the reference signal matches the reference dictionary. However, in the presence of MT effects, the reference signal is smaller than the reference dictionary. Comparing the two signal curves, MT effects can be quantified, as shown in Fig. 6.2b. Assuming MT effects is symmetric, the corrected dictionary with MT effects can be generated (shown in Fig. 6.2d) by adding the quantified MT signal to the dictionary with varying exchange rates k_{sw} (shown in Fig. 6.2c).

Mathematically, the MT corrections described above is based on the probabilistic model for Z-spectrum assuming CEST, MT and DS are non-mutually exclusive events (12). L_i refers to the signal of CEST, MT or DS.

$$Z(\Delta\omega) = 1 - \left(\sum_{i=1}^3 L_i(\Delta\omega) - \sum_{i=1, j>i}^3 (L_i(\Delta\omega) \times L_j(\Delta\omega)) + \prod_{i=1}^3 L_i(\Delta\omega) \right) \quad [6.2]$$

MT corrections can be separated into the following steps.

Step 1: Estimate the MT signal by comparing the reference signal with reference dictionary (Fig. 6.2a to Fig. 6.2b). The reference signal corresponds to Z and reference dictionary corresponds to DS signal. CEST signal is 0 at this step.

Step 2: Estimate CEST signal and from dictionary (Fig. 6.2c). In this scenario, reference dictionary corresponds to DS signal and the dictionary corresponds to Z in Eq. 6.2. MT signal is 0 at this step.

Step 3: Combine CEST signal, DS signal and MT signal determined from the previous steps following Eq. 6.2.

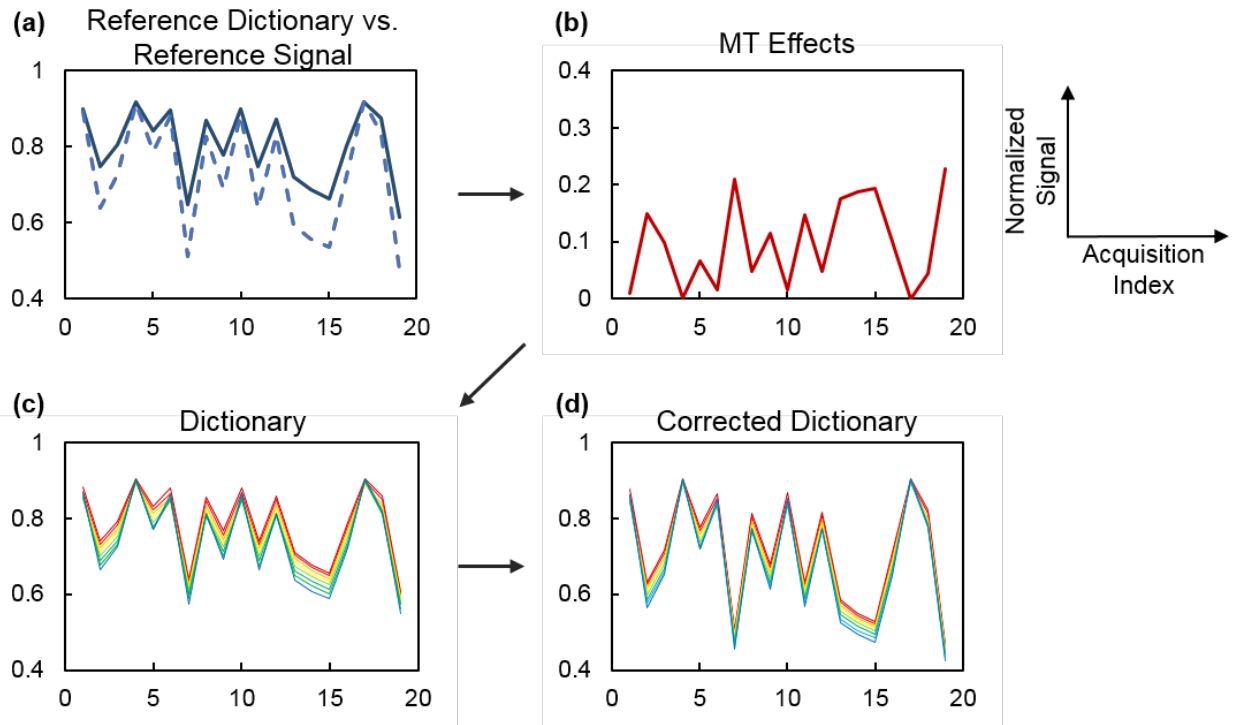


Figure 6.2 Framework of MT correction. (a) Reference dictionary (solid) and reference signal (dashed) are different in presence of MT effects. (b) MT effects can be quantified comparing the reference dictionary and reference signal. (c) Dictionary is generated by simulating 2-pool Bloch-McConnell equations. (d) Corrected dictionary can be generated by adding (b) MT effects to (c) dictionary.

6.2.4 Signal Matching

Signal matching was performed between the CEST signal and CEST dictionary. CEST signal was calculated by subtracting the label signal ($\Delta\omega = +\delta_s$) from the reference signal ($\Delta\omega =$

$-\delta_s$). CEST dictionary was calculated by subtracting the corrected dictionary from the corrected reference dictionary.

For each T_1 , T_2 combination, one dictionary entry that has the highest vector dot-product with the CEST signal was selected. In this case the labile proton fraction ratio is just a multiplicative constant which will not affect the matching result.

6.2.5 Phantom Preparation

Three groups of phantoms containing creatine monohydrate (Sigma-Aldrich, St. Louis, MO, USA) were prepared. For group 1, pH was varied and other parameters were similar. For group 2, agarose was added to induce MT effects. For group 3, the relaxation parameters T_1 , T_2 and the creatine concentration were also varied. The details of the phantoms are listed in Table 6.1. T_1 and T_2 were varied by adding nickel chloride (Sigma-Aldrich, St. Louis, MO, USA) and agarose (Sigma-Aldrich, St. Louis, MO, USA).

Table 6.1 Composition of the Three Phantom Groups

Group	T_1 (ms)	T_2 (ms)	Agarose	Creatine Concentration (mM)	pH
1	786	709	0	60	6.96
1	1299	1099	0	60	6.85
1	902	875	0	60	6.45
1	974	774	0	60	7.27
1	1226	1133	0	60	6.76
2	1037	136	1.5%	60	6.70
2	1059	133	1.5%	60	7.18
2	1056	136	1.5%	60	7.10
2	1022	140	1.5%	60	6.77
2	1035	130	1.5%	60	7.49
3	1721	140	1.5%	60	6.96
3	1389	143	1.5%	60	6.94
3	1042	116	2%	60	6.72
3	449	137	1%	60	7.45
3	1069	133	1.5%	100	7.06

3	1071	135	1.5%	30	7.06
---	------	-----	------	----	------

6.2.6 MRI Acquisition

Phantom experiments were performed at 20°C on a 3T clinical scanner (Magnetom Verio; Siemens Healthcare, Erlangen, Germany) with a standard 32-channel head receiver coils. CEST fingerprinting and pulsed qCEST were performed for comparison. For both methods, images were acquired with saturation frequency offsets at ± 2.6 ppm, ± 2.3 ppm, ± 2.0 ppm, ± 1.7 ppm and ± 1.4 ppm. All images were acquired with a slice thickness of 5 mm, field of view of 150 x 150 mm², resolution of 2.3 x 2.3 mm² and imaging matrix of 64 x 64. B₀ field was corrected using WASSR method.

The total scan time of CEST fingerprinting method was approximately 10 min. Images were acquired with single-shot FLASH readout (flip angle: 15°, iPAT: 2, number of segments: 48, number of averages: 1, TE: 1.5 ms). The gap time between two CEST saturation blocks was fixed to be 1000 ms. CEST preparation module consists of 30-ms Gaussian saturation pulses (flip angle ranging from 100° to 1500°) with 50% duty cycle. For each saturation frequency offset, 20 images with varying CEST saturation power B₁ and saturation time (as shown in Fig. 6.1b and 6.1c) were acquired. This was repeated for all different CEST saturation frequency offsets.

The total scan time of pulsed qCEST method was approximately 50 min. Images were acquired with single-shot TSE readout (flip angle: 180°, iPAT: 2, echo train length: 48, number of averages: 3, TR: 16000 ms, TE: 7 ms). CEST preparation module consists of fifty 80-ms Gaussian-shaped pulses with 50% duty cycle (total saturation time 8000 ms). CEST experiments were repeated with different saturation flip angle 900°, 1500°, 2100° and 2800°.

T₁-weighted MR images were acquired by an inversion recovery TSE sequence with 10 different inversion delays (TI = 50-2500 ms; TR/TE = 6000/12 ms). T₂-weighted MR images were acquired by a TSE sequence with varying echo delays (TE = 12-400 ms; TR = 6000 ms).

6.2.7 Data Analysis

Post processing was performed with custom-written programs in Matlab (The Mathworks, Natick, MA, USA). The resonant frequency of creatine protons is +2.0 ppm. Reference signal (-2.0 ppm) and label signal (+2.0 ppm) were calculated with B_0 field correction and normalized with a reference image acquired with no CEST saturation pulses. The dictionary simulation and signal matching was performed as described above to determine the exchange rate k_{sw} . These calculations were performed pixel-by-pixel and by region of interest (ROI). The T_1 maps and T_2 maps were obtained by pixel-by-pixel logarithmic fit of the signal equation.

6.3 Result

Fig. 6.3a shows the simulated CEST signal with different exchange rates ranging from 10 s^{-1} to 400 s^{-1} for tissues with T_1 of 1000 ms and T_2 of 120 ms using the sequence patterns shown in Fig. 6.1b and 6.1c. Fig. 6.3b shows an acquired CEST signal curve from one the phantoms and its match to the CEST dictionary. Note the signal curves is normalized to one in these figures.

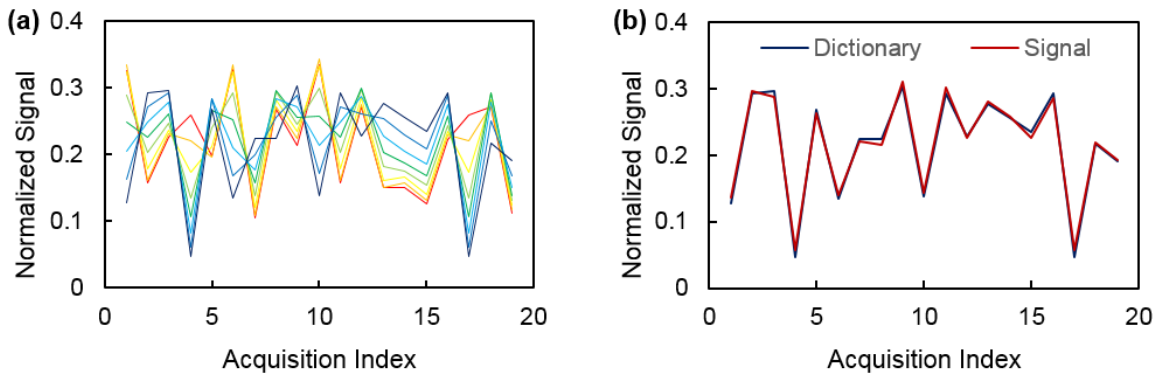


Figure 6.3 Signal properties and matching results from phantom study. (a) Simulated CEST signal with different exchange rates. **(b)** Measured CEST signal and the corresponding dictionary match.

Pixel-wise mapping of chemical exchange rate k_{sw} of all phantom groups were shown in Fig. 6.4. For group 1, both CEST fingerprinting and pulsed qCEST methods can provide homogenous exchange rate maps. However, for group 2 and group 3 with MT effects, there is

more noise in the exchange rate maps generated by pulsed qCEST method. This is because long CEST saturation pulses used in pulsed qCEST method will cause large MT effects. The CEST-weighted images acquired by pulsed qCEST method have reduced SNR because of the MT effects.

The relationship between exchange rate k_{sw} and pH was shown in Fig. 6.5 for both CEST fingerprinting and pulsed qCEST methods. All phantom vials were presented, with group 1 in red, group 2 in blue and group 3 in green. The error bars represent the standard deviation of the exchange rates within the ROI of each tube. The dark gray dashed lines in Fig. 6.5 represent the fitted curve of exchange rate as a function of pH. For CEST fingerprinting method, the exchange rate can be described as $k_{sw} = 1.35 \times 10^{\text{pH}-5} - 18.14$ ($R^2 = 0.9614$). For pulsed qCEST method, the exchange rate can be described as $k_{sw} = 1.25 \times 10^{\text{pH}-5} + 145.70$ ($R^2 = 0.6784$). The results were compared with exchange rates reported by Goerke et al. shown in red dashed line in Fig. 6.5 (166). It can be seen that the exchange rates measured by CEST fingerprinting method are very close to the literature values.

In summary, CEST fingerprinting method can provide more accurate and more efficient measurements of exchange rates in the presence of MT effects.

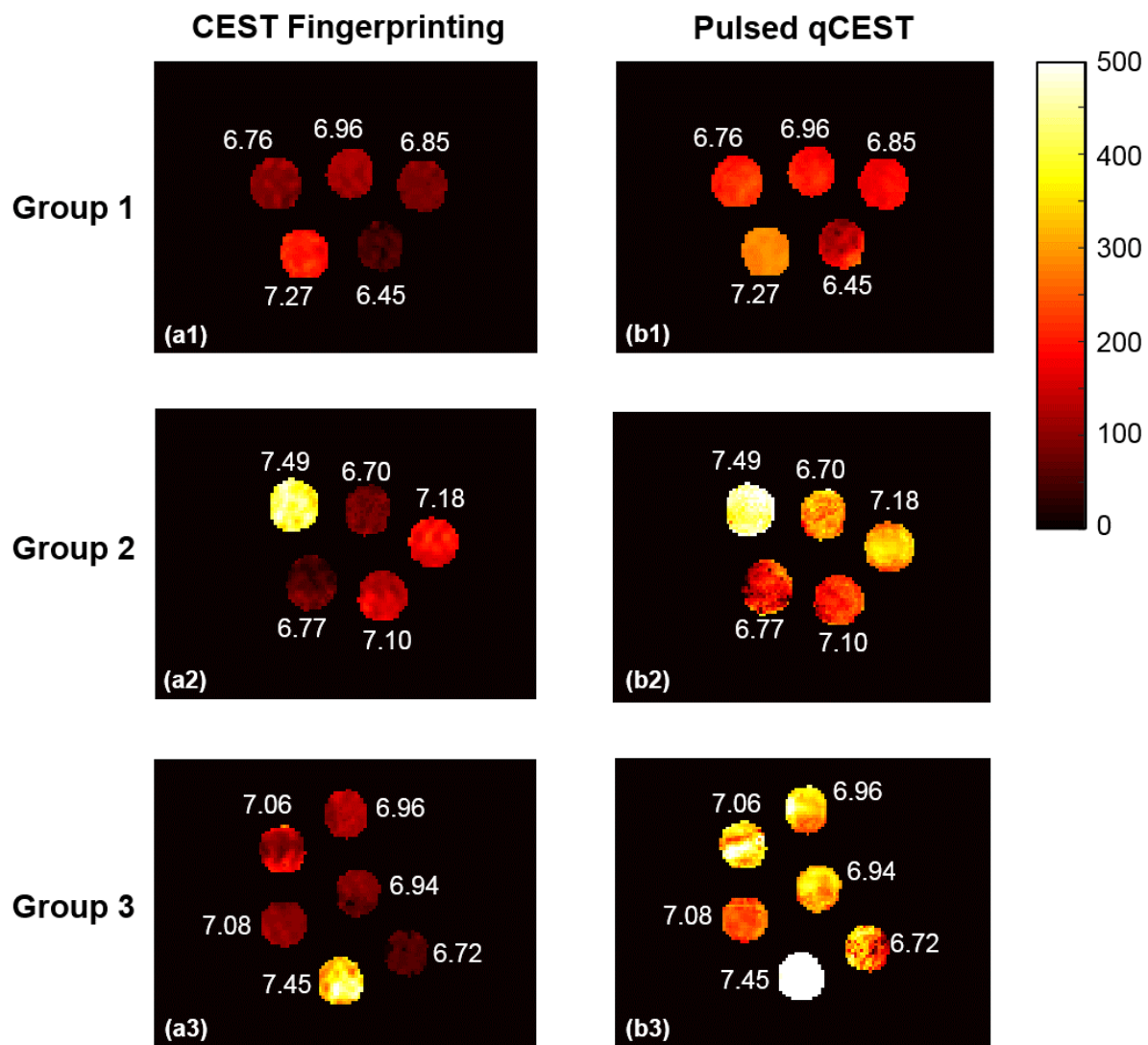


Figure 6.4 Exchange rate maps of the phantom studies.

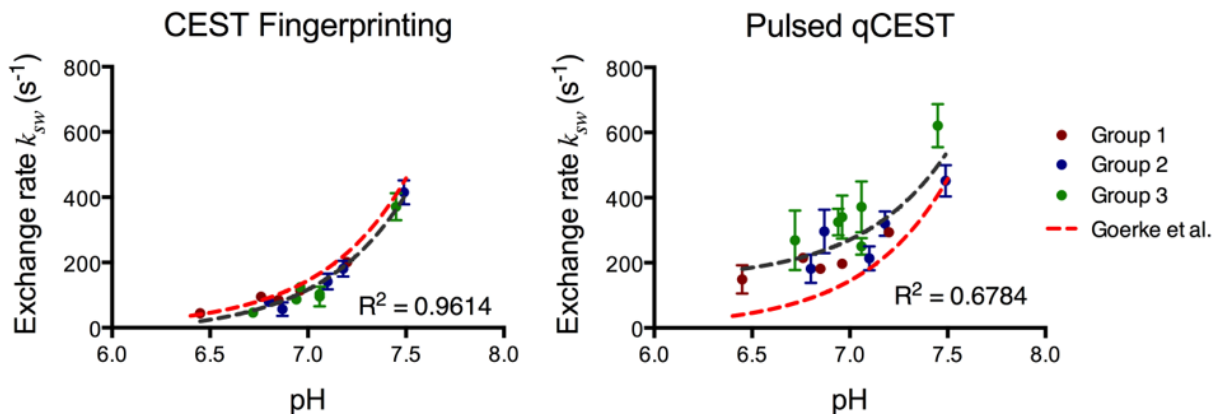


Figure 6.5 Chemical exchange rate as a function of pH. The error bars represent standard deviation of the exchange rate within the ROI of each tube. The dark gray dashed line represents the fitted curve of exchange rate as a function of pH. This was compared with the exchange rates reported by Goerke et al. at 20°C shown in red dashed line (166).

6.4 Discussion

In this work, MR fingerprinting concept was introduced for exchange rate quantification in CEST imaging. The phantom studies demonstrated that CEST fingerprinting can measure the exchange rate more efficiently and more accurately compared to previous CEST quantification methods.

6.4.1 CEST Fingerprinting

In CEST fingerprinting framework, CEST saturation power and saturation time were varied in the CEST preparation module. Similar ideas were also used in previous studies (167-169). The random pattern of CEST sequence parameters will generate unique signal evolution, which makes the technique more robust to noise. In addition, the oscillatory signal curve contains more informative points as compared to conventional CEST quantification methods which always reach a steady state level for chemical exchange after some finite amount of saturation time.

Another key element of CEST fingerprinting framework is dictionary simulation and signal matching. In conventional CEST quantification methods, the signal is fitted to the approximated analytical solution of BM equations. However, this adds some restrictions to the CEST

experiments. Long saturation time is required for the chemical exchange to reach steady state and long TR is required for full longitudinal recovery. However, with the signal curve directly matched to a pre-defined dictionary, the restrictions described above can be removed. In this study, the CEST saturation time T_{sat} is 1000-2000 ms and the TR is 2000-3000 ms while in the conventional CEST quantification methods, T_{sat} is at least 4000 ms and the TR is normally 8000 ms or more. This explains why CEST fingerprinting is more efficient than conventional CEST quantification methods.

Long CEST saturation pulses of the conventional CEST quantification methods were designed to make sure the chemical exchange between water protons and solute protons has reached steady state. However, MT effects were also increased at the same time. In most of the cases, MT signal change is much bigger than the CEST signal increase benefited from the long CEST saturation pulses. Therefore, long CEST saturation pulses reduce the SNR significantly when MT effects are present. As shown in Fig. 6.4b, for pulsed qCEST method, the exchange rate maps of group 2 and 3 (with agarose) are noisier than the exchange rate map of group 1 (without agarose). In CEST fingerprinting, because CEST saturation duration is not too long (1000-2000 ms), this is less of an issue.

CEST fingerprinting has very subtle signal change compared to MRF due to the nature of CEST imaging. In most *in vivo* studies, the CEST signal is less than 5%. This means CEST fingerprinting will not be as robust to noise as compared to MRF. Therefore, in the framework, highly undersampled image acquisition was not adopted and the sequence parameters were optimized to make sure there was enough CEST signal so that the signal curve can be matched to the dictionary correctly.

6.4.2 MT Correction

In this study, MT correction was performed using dictionary as a no-MT reference. MT signal was estimated by comparing the reference signal and reference dictionary. Reference

signal and reference dictionary represent the signal and dictionary at the opposite solute resonant frequency $-\delta_s$. Without CEST effects, the difference between the reference signal and reference dictionary is solely from MT effects. MT signal can then be quantified. With the assumption of symmetric MT effects, the MT signal estimated at $-\delta_s$ can be used to correct the MT effects at $+\delta_s$.

There are also other ways to perform MT corrections without the need for reference data. These methods use the wide-offset data ($|\Delta\omega| > 7$ ppm) to fit for the MT model. The fitted parameters were used to correct for MT effects at solute resonant frequency (27,170). There are also attempts to correct for MT effects using 3-pool CEST fingerprinting. However, these methods all require multi-parametric fitting/matching. Due to complexity of the model, the fitting/matching process could be challenging and multiple points are acquired for MT correction.

6.4.3 Potential Impacts

In this work, we presented the proof-of-concept implementation of CEST fingerprinting. However, the framework can be extended to quantify other proton-exchange contrast mechanisms, including chemical exchange sensitive spin-lock (CESL) (171-173), bSSFPX (174) and magnetization transfer (175). The sequences of these techniques are similar to CEST sequences in the way that they all use off-resonance saturation pulses. More broadly, the framework presented in this study can serve as an example of how to apply MRF concept for contrast mechanisms that use preparation pulses to achieve the contrast, such as diffusion. By varying the preparation parameters and matching the signal to a pre-defined dictionary, the efficiency can be improved because more informative points can be acquired in a faster way.

6.4.4 Moving to in vivo Studies

Our study demonstrated CEST fingerprinting in vitro. Further investigation is needed to validate this work in vivo. However, there are more complicated completing effects in vivo. One of major challenge is the NOE effects resonant at ~ -3 ppm. It can be quite challenging to get the

correct reference data for protons that resonate between +2 ppm to +4 ppm without the contamination from NOE effects. For these protons, other MT corrections methods that do not require reference data need to be used as described above.

In addition to that, there are normally more than one group of solute protons in vivo. For example, there are amide protons of proteins and peptides that resonate at +3.5 ppm and amine protons of glutamine that resonate at +3.0 ppm in the brain. The resonant frequencies of the two groups of protons are very close, which means the CEST effects of the two solute pools might be affected by each other. However, it is possible to use multi-pool Bloch-McConnell equations to simulate in vivo situation to achieve more accurate quantification.

6.5 Conclusions

In this work, CEST fingerprinting was proposed for exchange rate quantification. Phantom studies demonstrated that CEST fingerprinting was more efficient (5x faster) compared to pulsed qCEST because there is no need for long saturation time and long TR. It is also shown that the proposed CEST fingerprinting technique can quantify exchange rate more accurately in the presence of MT effects.

CHAPTER 7: Conclusions and Future Work

7.1 Summary of the Work

CEST is an emerging magnetic resonance metabolic imaging technique. In this dissertation, the major focus is to make the CEST imaging technique more efficient and more accurate. Specifically, three areas of improvement were made in this work.

7.1.1 Cardiac CEST

The major challenge of cardiac CEST is the scan time and the reliability. In Chapter 2, a clinically affordable scan time (~ 5 min/slice depending on the navigator acceptance rate) was achieved by optimized data acquisition scheme, advanced motion correction methods and improved signal analysis. Validation studies were performed in chronic myocardial infarction animal model using LGE as reference. It was shown that the infarct region has lower CEST signal compared to remote myocardium. Spatially, the hypointense regions in the CEST contrast maps closely match the bright areas in the LGE images. In Chapter 3, the cardiac CEST technique with dual-echo readout was proposed to further improve the reliability of the technique. This method allows simultaneous acquisition of B_0 map and CEST weighted images for each saturation frequency to address the B_0 field variations induced by respiratory motion. In the results, the proposed cardiac CEST technique with dual-echo readout is shown to have improved repeatability compared to the previous method.

In summary, the cardiac CEST technique has the potential to provide information on metabolic abnormalities for cardiac diseases.

7.1.2 pH Assessment in the IVD

The major challenge of CEST application in the IVD is how to quantify the exchange rate from the complex CEST model which involves multiple confounding factors. qCEST imaging protocol was developed based on the observation that CEST effect can be represented as a linear

function of $1/B_1^2$. Multiple CEST experiments with varying B_1 amplitudes were performed for omega plot analysis to estimate the exchange rate. In Chapter 4, the qCEST imaging protocol was validated in a preclinical porcine model. The pH values inside the IVD was manipulated by injecting Na-Lactate. It is shown that the exchange rate measured by qCEST technique is highly correlated with the pH value measured using tissue pH-meter. In Chapter 5, qCEST technique was applied in an animal model with induced disc degeneration. Direct pH measurement inside the degenerated IVDs revealed a significant pH drop after degeneration, which correlated with a significant increase in the exchange rate measured by qCEST. In addition, gene analysis of harvested degenerated IVDs revealed significant up-regulation of pain, nerve- and inflammatory-related markers at 6 and 10 weeks after degeneration. A strong positive correlation was observed between expression of pain markers and increase in the exchange rate.

Collectively, these findings demonstrate that this approach can be used to measure pH in vivo within the IVD and has the potential to be used as a novel non-invasive method for the diagnosis of discogenic pain.

7.1.3 CEST Fingerprinting

CEST fingerprinting was introduced to achieve more efficient and more accurate exchange rate quantification, to address the limitations of the qCEST technique. Instead of using a repeated, serial acquisition of data to fit to a particular equation such as qCEST technique, CEST fingerprinting utilizes CEST saturation with varying saturation power B_1 amplitude and saturation time to create uniqueness of signal evolution for different exchange rates. The acquired signal was matched directly to a pre-defined dictionary. MT effects can also be addressed in the framework of CEST fingerprinting. The simulated dictionary can serve as signal curve when there are no MT effects. Comparing the dictionary to the acquired signal provides a chance to correct for MT effects. Phantom studies demonstrated that CEST fingerprinting was more efficient (5x faster) compared to pulsed qCEST because there is no need for long saturation time and long

TR. It is also shown that the proposed CEST fingerprinting technique can quantify exchange rate more accurately in the presence of MT effects.

7.2 Future Directions

In general, the future direction for CEST field is to further reduce the scan time and to interpret CEST images for specific clinical applications.

7.2.1 Scan Time Reduction

CEST fingerprinting has already shown to the ability perform CEST quantification more efficiently. However, there is more potential to further improve the data acquisition efficiency. The current CEST fingerprinting framework acquires hundreds of images with different saturation frequency offsets, CEST saturation power and saturation time. With the recently developed low rank tensor reconstruction technique, it is possible to explore the redundancy of the data structure and extend the current 2D single-slice imaging to 3D imaging.

The scan time can also be reduced by addressing the motion more efficiently. As presented in Chapter 2 and 3, cardiac and respiratory motion was currently minimized by using ECG trigger and navigator gating. However, it is also possible to acquire CEST-weighted data constantly, and with additional self-gating lines, the data can be categorized into different motion bins. This can be achieved with either steady-state CEST(176) or bSSFPX(174). These two methods both acquire data at very short interval, which is enough to capture the cardiac and respiratory motion. This can reduce the scan time because of constant data acquisition instead of using dead wait time. Potentially, a 3D cardiac CEST technique can be developed.

7.2.2 Clinical Validations

In general, some of the CEST imaging techniques are mature for clinical applications. However, it is not yet clear how clinical diagnosis can benefit from CEST imaging. There are some ongoing studies to interpret CEST signal for clinical applications such brain tumor.

More specifically, for cardiac CEST, the first step is to perform histopathology studies to show that cardiac CEST signal is correlated with Cr concentration in the myocardium. Cr concentration in the ex vivo myocardium can be measured using perchloric acid (PCA) extraction method. Cardiac CEST technique can also be applied to clinical patients such as diabetic patient cohort and coronary microvascular dysfunction patient cohort because it has been previously shown that these patients have reduced myocardial metabolic activity. The patient studies can be performed to evaluate if cardiac CEST can serve as an additional information, or even an early marker for clinical diagnosis.

In this dissertation, CEST fingerprinting was only tested in phantom studies. Further investigation is needed to validate this technique in vivo. The potential applications include penumbra detection for stroke patients and tumor monitor/ treatment.

Reference

1. Ward KM, Aletras AH, Balaban RS. A New Class of Contrast Agents for MRI Based on Proton Chemical Exchange Dependent Saturation Transfer (CEST). *J Magn Reson* 2000;143:79–87. doi: 10.1006/jmre.1999.1956.
2. Ward KM, Balaban RS. Determination of pH using water protons and chemical exchange dependent saturation transfer (CEST). *Magn Reson Med* 2000;44:799–802. doi: 10.1002/1522-2594(200011)44:5<799::AID-MRM18>3.0.CO;2-S.
3. van Zijl PCM, Yadav NN. Chemical exchange saturation transfer (CEST): what is in a name and what isn't? *Magn Reson Med* 2011;65:927–948. doi: 10.1002/mrm.22761.
4. Ling W, Regatte RR, Navon G, Jerschow A. Assessment of glycosaminoglycan concentration in vivo by chemical exchange-dependent saturation transfer (gagCEST). *PNAS* 2008;105:2266–2270. doi: 10.1073/pnas.0707666105.
5. Singh A, Haris M, Cai K, Kassey VB, Kogan F, Reddy D, Hariharan H, Reddy R. Chemical exchange saturation transfer magnetic resonance imaging of human knee cartilage at 3 T and 7 T. *Magn Reson Med* 2012;68:588–594. doi: 10.1002/mrm.23250.
6. Saar G, Zhang B, Ling W, Regatte RR, Navon G, Jerschow A. Assessment of glycosaminoglycan concentration changes in the intervertebral disc via chemical exchange saturation transfer. *NMR Biomed* 2012;25:255–261. doi: 10.1002/nbm.1741.
7. Haneder S, Apprich SR, Schmitt B, Michaely HJ, Schoenberg SO, Friedrich KM, Trattnig S. Assessment of glycosaminoglycan content in intervertebral discs using chemical exchange saturation transfer at 3.0 Tesla: preliminary results in patients with low-back pain. *Eur Radiol* 2013;23:861–868. doi: 10.1007/s00330-012-2660-6.
8. Liu Q, Tawackoli W, Pelled G, et al. Detection of low back pain using pH level-dependent imaging of the intervertebral disc using the ratio of R1 ρ dispersion and -OH chemical exchange saturation transfer (RROC). *Magn Reson Med* 2015;73:1196–1205. doi: 10.1002/mrm.25186.
9. Melkus G, Grabau M, Karampinos DC, Majumdar S. Ex vivo porcine model to measure pH dependence of chemical exchange saturation transfer effect of glycosaminoglycan in the intervertebral disc. *Magn Reson Med* 2014;71:1743–1749. doi: 10.1002/mrm.24838.
10. Kogan F, Haris M, Debrosse C, Singh A, Nanga RP, Cai K, Hariharan H, Reddy R. In vivo chemical exchange saturation transfer imaging of creatine (CrCEST) in skeletal muscle at 3T. *Journal of Magnetic Resonance Imaging* 2014;40:596–602. doi: 10.1002/jmri.24412.
11. Kogan F, Haris M, Singh A, Cai K, Debrosse C, Nanga RPR, Hariharan H, Reddy R. Method for high- resolution imaging of creatine in vivo using chemical exchange saturation transfer. *Magn Reson Med* 2014;71:164–172. doi: 10.1002/mrm.24641.
12. Haris M, Singh A, Cai K, et al. A technique for in vivo mapping of myocardial creatine kinase metabolism. *Nat Med* 2014;20:209–214. doi: 10.1038/nm.3436.
13. Zhou J, Payen J-F, Wilson DA, Traystman RJ, van Zijl PCM. Using the amide proton signals

of intracellular proteins and peptides to detect pH effects in MRI. *Nat Med* 2003;9:1085–1090. doi: 10.1038/nm907.

14. Zhou J, Blakeley JO, Hua J, Kim M, Laterra J, Pomper MG, van Zijl PCM. Practical data acquisition method for human brain tumor amide proton transfer (APT) imaging. *Magn Reson Med* 2008;60:842–849. doi: 10.1002/mrm.21712.

15. Togao O, Yoshiura T, Keupp J, et al. Amide proton transfer imaging of adult diffuse gliomas: correlation with histopathological grades. *Neuro Oncol* 2014;16:441–448. doi: 10.1093/neuonc/not158.

16. Jia G, Abaza R, Williams JD, et al. Amide proton transfer MR imaging of prostate cancer: A preliminary study. *Journal of Magnetic Resonance Imaging* 2011;33:647–654. doi: 10.1002/jmri.22480.

17. Dula AN, Arlinghaus LR, Dortch RD, Dewey BE, Whisenant JG, Ayers GD, Yankeelov TE, Smith SA. Amide proton transfer imaging of the breast at 3 T: Establishing reproducibility and possible feasibility assessing chemotherapy response. *Magn Reson Med* 2013;70:216–224. doi: 10.1002/mrm.24450.

18. Togao O, Hiwatashi A, Yamashita K, et al. Grading diffuse gliomas without intense contrast enhancement by amide proton transfer MR imaging: comparisons with diffusion- and perfusion-weighted imaging. *Eur Radiol* 2017;27:578–588. doi: 10.1007/s00330-016-4328-0.

19. Mehrabian H, Desmond KL, Soliman H, Sahgal A, Stanis GJ. Differentiation between Radiation Necrosis and Tumor Progression Using Chemical Exchange Saturation Transfer. *Clin. Cancer Res.* 2017;clincanres.2265.2016. doi: 10.1158/1078-0432.CCR-16-2265.

20. Park KJ, Kim HS, Park JE, Shim WH, Kim SJ, Smith SA. Added value of amide proton transfer imaging to conventional and perfusion MR imaging for evaluating the treatment response of newly diagnosed glioblastoma. *Eur Radiol* 2016;26:4390–4403. doi: 10.1007/s00330-016-4261-2.

21. Jiang S, Yu H, Wang X, et al. Molecular MRI differentiation between primary central nervous system lymphomas and high-grade gliomas using endogenous protein-based amide proton transfer MR imaging at 3 Tesla. *Eur Radiol* 2016;26:64–71. doi: 10.1007/s00330-015-3805-1.

22. Sun PZ, Benner T, Copen WA, Sorensen AG. Early Experience of Translating pH-Weighted MRI to Image Human Subjects at 3 Tesla. *Stroke* 2010;41:S147–S151. doi: 10.1161/STROKEAHA.110.595777.

23. Sun PZ, Wang E, Cheung JS. Imaging acute ischemic tissue acidosis with pH-sensitive endogenous amide proton transfer (APT) MRI--correction of tissue relaxation and concomitant RF irradiation effects toward mapping quantitative cerebral tissue pH. *NeuroImage* 2012;60:1–6. doi: 10.1016/j.neuroimage.2011.11.091.

24. Tietze A, Blicher J, Mikkelsen IK, Ostergaard L, Strother MK, Smith SA, Donahue MJ. Assessment of ischemic penumbra in patients with hyperacute stroke using amide proton transfer (APT) chemical exchange saturation transfer (CEST) MRI. *NMR Biomed* 2014;27:163–174. doi: 10.1002/nbm.3048.

25. Guo Y, Zhou IY, Chan S-T, Wang Y, Mandeville ET, Igarashi T, Lo EH, Ji X, Sun PZ. pH-

sensitive MRI demarcates graded tissue acidification during acute stroke - pH specificity enhancement with magnetization transfer and relaxation-normalized amide proton transfer (APT) MRI. *NeuroImage* 2016;141:242–249. doi: 10.1016/j.neuroimage.2016.07.025.

26. Kim J, Wu Y, Guo Y, Zheng H, Sun PZ. A review of optimization and quantification techniques for chemical exchange saturation transfer MRI toward sensitive in vivo imaging. *Contrast Media Mol Imaging* 2015;10:163–178. doi: 10.1002/cmml.1628.

27. Heo HY, Zhang Y, Jiang S, Lee DH, Zhou J. Quantitative assessment of amide proton transfer (APT) and nuclear overhauser enhancement (NOE) imaging with extrapolated semisolid magnetization transfer reference (EMR) signals: II. Comparison of three EMR models and application to human brain glioma at 3 Tesla. *Magn Reson Med* 2016;75:1630–1639. doi: 10.1002/mrm.25795.

28. Chan K W Y, McMahon MT, Kato Y, Liu G, Bulte JWM, Bhujwala ZM, Artemov D, van Zijl PCM. Natural D- glucose as a biodegradable MRI contrast agent for detecting cancer. *Magn Reson Med* 2012;68:1764–1773. doi: 10.1002/mrm.24520.

29. Walker-Samuel S, Ramasawmy R, Torrealdea F, et al. In vivo imaging of glucose uptake and metabolism in tumors. *Nat Med* 2013;19:1067–1072. doi: 10.1038/nm.3252.

30. Xu X, Chan K W Y, Knutsson L, et al. Dynamic glucose enhanced (DGE) MRI for combined imaging of blood-brain barrier break down and increased blood volume in brain cancer. *Magn Reson Med* 2015;74:1556–1563. doi: 10.1002/mrm.25995.

31. Xu X, Yadav NN, Knutsson L, et al. Dynamic Glucose-Enhanced (DGE) MRI: Translation to Human Scanning and First Results in Glioma Patients. *Tomography* 2015;1:105–114. doi: 10.18383/j.tom.2015.00175.

32. Longo DL, Michelotti F, Consolino L, Bardini P, Digilio G, Xiao G, Sun PZ, Aime S. In Vitro and In Vivo Assessment of Nonionic Iodinated Radiographic Molecules as Chemical Exchange Saturation Transfer Magnetic Resonance Imaging Tumor Perfusion Agents. *Investigative Radiology* 2016;51:155–162. doi: 10.1097/RLI.0000000000000217.

33. Longo DL, Sun PZ, Consolino L, Michelotti FC, Uggeri F, Aime S. A general MRI-CEST ratiometric approach for pH imaging: demonstration of in vivo pH mapping with iobitridol. *J. Am. Chem. Soc.* 2014;136:14333–14336. doi: 10.1021/ja5059313.

34. Longo DL, Bartoli A, Consolino L, Bardini P, Arena F, Schwaiger M, Aime S. In Vivo Imaging of Tumor Metabolism and Acidosis by Combining PET and MRI-CEST pH Imaging. *Cancer Res* 2016;76:6463–6470. doi: 10.1158/0008-5472.CAN-16-0825.

35. Anemone A, Consolino L, Longo DL. MRI-CEST assessment of tumour perfusion using X-ray iodinated agents: comparison with a conventional Gd-based agent. *Eur Radiol* 2016;1–10. doi: 10.1007/s00330-016-4552-7.

36. Gilad AA, McMahon MT, Walczak P, Winnard PT, Raman V, van Laarhoven HWM, Skoglund CM, Bulte JWM, van Zijl PCM. Artificial reporter gene providing MRI contrast based on proton exchange. *Nature Biotechnology* 2007;25:217–219. doi: 10.1038/nbt1277.

37. Liu G, Bulte JWM, Gilad AA. CEST MRI Reporter Genes. In: *Magnetic Resonance*

Neuroimaging. Vol. 711. Methods in Molecular Biology. Totowa, NJ: Humana Press; 2010. pp. 271–280. doi: 10.1007/978-1-61737-992-5_13.

38. Farrar CT, Buhrman JS, Liu G, Kleijn A, Lamfers MLM, McMahon MT, Gilad AA, Fulci G. Establishing the Lysine-rich Protein CEST Reporter Gene as a CEST MR Imaging Detector for Oncolytic Virotherapy. *Radiology* 2015. doi: 10.1148/radiol.14140251.

39. García-Figueiras R, Baleato-González S, Padhani AR, Oleaga L, Vilanova JC, Luna A, Cobas Gómez JC. Proton magnetic resonance spectroscopy in oncology: the fingerprints of cancer? *Diagn Interv Radiol* 2016;22:75–89. doi: 10.5152/dir.2015.15009.

40. Martín Noguerol T, Sánchez-González J, Martínez Barbero JP, García-Figueiras R, Baleato-González S, Luna A. Clinical Imaging of Tumor Metabolism with ¹H Magnetic Resonance Spectroscopy. *Magnetic Resonance Imaging Clinics of North America* 2016;24:57–86. doi: 10.1016/j.mric.2015.09.002.

41. Faller KME, Lygate CA, Neubauer S, Schneider JE. ¹H-MR spectroscopy for analysis of cardiac lipid and creatine metabolism. *Heart Fail Rev* 2013;18:657–668. doi: 10.1007/s10741-012-9341-z.

42. Ende G. Proton Magnetic Resonance Spectroscopy: Relevance of Glutamate and GABA to Neuropsychology. *Neuropsychol Rev* 2015;25:315–325. doi: 10.1007/s11065-015-9295-8.

43. Bustillo JR. Use of proton magnetic resonance spectroscopy in the treatment of psychiatric disorders: a critical update. *Dialogues Clin Neurosci* 2013;15:329–337. doi: 10.1111/jnc.12398/full.

44. Zhang N, Song X, Bartha R, Beyea S, D'Arcy R, Zhang Y, Rockwood K. Advances in high-field magnetic resonance spectroscopy in Alzheimer's disease. *Curr Alzheimer Res* 2014;11:367–388.

45. Lam F, Ma C, Clifford B, Johnson CL, Liang Z-P. High- resolution ¹H- MRSI of the brain using SPICE: Data acquisition and image reconstruction. *Magn Reson Med* 2016;76:1059–1070. doi: 10.1002/mrm.26019.

46. Ma C, Lam F, Johnson CL, Liang Z-P. Removal of nuisance signals from limited and sparse ¹H MRSI data using a union- of- subspaces model. *Magn Reson Med* 2016;75:488–497. doi: 10.1002/mrm.25635.

47. Kemp GJ, Ahmad RE, Nicolay K, Prompers JJ. Quantification of skeletal muscle mitochondrial function by ³¹P magnetic resonance spectroscopy techniques: a quantitative review. *Acta Physiologica* 2015;213:107–144. doi: 10.1111/apha.12307.

48. Beer M, Seyfarth T, Sandstede J, Landschütz W, Lipke C, Köstler H, Kienlin von M, Harre K, Hahn D, Neubauer S. Absolute concentrations of high-energy phosphate metabolites in normal, hypertrophied, and failing human myocardium measured noninvasively with (³¹P)-SLOOP magnetic resonance spectroscopy. *J Am Coll Cardiol* 2002;40:1267–1274.

49. Bottomley PA, Wu KC, Gerstenblith G, Schulman SP, Steinberg A, Weiss RG. Reduced Myocardial Creatine Kinase Flux in Human Myocardial Infarction An In Vivo Phosphorus Magnetic Resonance Spectroscopy Study. *Circulation* 2009;119:1918–1924. doi:

10.1161/CIRCULATIONAHA.108.823187.

50. Dawson DK, Neil CJ, Henning A, Cameron D, Jagpal B, Bruce M, Horowitz J, Frenneaux MP. Tako-Tsubo Cardiomyopathy: A Heart Stressed Out of Energy? *JACC Cardiovasc Imaging* 2015;8:985–987. doi: 10.1016/j.jcmg.2014.10.004.

51. Bottomley PA, Weiss RG. Noninvasive localized MR quantification of creatine kinase metabolites in normal and infarcted canine myocardium. *Radiology* 2001;219:411–418. doi: 10.1148/radiology.219.2.r01ma39411.

52. Månsson S, Johansson E, Magnusson P, Chai C-M, Hansson G, Petersson JS, Ståhlberg F, Golman K. ¹³C imaging—a new diagnostic platform. *Eur Radiol* 2006;16:57–67. doi: 10.1007/s00330-005-2806-x.

53. Brindle KM, Bohndiek SE, Gallagher FA, Kettunen MI. Tumor imaging using hyperpolarized ¹³C magnetic resonance spectroscopy. *Magn Reson Med* 2011;66:505–519. doi: 10.1002/mrm.22999.

54. Rider OJ, Tyler DJ. Clinical implications of cardiac hyperpolarized magnetic resonance imaging. *Journal of Cardiovascular Magnetic Resonance* 2013;15:93. doi: 10.1186/1532-429X-15-93.

55. Gallagher FA, Kettunen MI, Day SE, et al. Magnetic resonance imaging of pH in vivo using hyperpolarized ¹³C-labelled bicarbonate. *Nature* 2008;453:940–943. doi: 10.1038/nature07017.

56. Nelson SJ, Ozhinsky E, Li Y, Park IW, Crane J. Strategies for rapid in vivo ¹H and hyperpolarized ¹³C MR spectroscopic imaging. *J Magn Reson* 2013;229:187–197. doi: 10.1016/j.jmr.2013.02.003.

57. Adamson E, Ludwig K, Mummy D, Fain SB. Magnetic resonance imaging with hyperpolarized agents: methods and applications. *Phys Med Biol* 2017. doi: 10.1088/1361-6560/aa6be8.

58. McMahon MT, Gilad AA, Zhou J, Sun PZ, Bulte JWM, van Zijl PCM. Quantifying exchange rates in chemical exchange saturation transfer agents using the saturation time and saturation power dependencies of the magnetization transfer effect on the magnetic resonance imaging signal (QUEST and QUESP): Ph calibration for poly- L- lysine and a starburst dendrimer. *Magn Reson Med* 2006;55:836–847. doi: 10.1002/mrm.20818.

59. Zaiss M, Xu J, Goerke S, Khan IS, Singer RJ, Gore JC, Gochberg DF, Bachert P. Inverse Z-spectrum analysis for spillover-, MT-, and T1 -corrected steady-state pulsed CEST-MRI--application to pH-weighted MRI of acute stroke. *NMR Biomed* 2014;27:240–252. doi: 10.1002/nbm.3054.

60. Wu R, Xiao G, Zhou IY, Ran C, Sun PZ. Quantitative chemical exchange saturation transfer (qCEST) MRI - omega plot analysis of RF-spillover-corrected inverse CEST ratio asymmetry for simultaneous determination of labile proton ratio and exchange rate. *NMR Biomed* 2015;28:376–383. doi: 10.1002/nbm.3257.

61. Ingwall JS, Weiss RG. Is the Failing Heart Energy Starved? On Using Chemical Energy to Support Cardiac Function. *Circulation Research* 2004;95:135–145. doi: 10.1161/01.RES.0000137170.41939.d9.

62. Dzeja PP, Redfield MM, Burnett JC, Terzic A. Failing energetics in failing hearts. *Curr Cardiol Rep* 2000;2:212–217. doi: 10.1007/s11886-000-0071-9.
63. Reimer KA, Jennings RB, Tatum AH. Pathobiology of acute myocardial ischemia: Metabolic, functional and ultrastructural studies. *American Journal of Cardiology* 1983;52:72–81. doi: 10.1016/0002-9149(83)90180-7.
64. Bottomley PA, Weiss RG. Non-invasive magnetic-resonance detection of creatine depletion in non-viable infarcted myocardium. *The Lancet* 1998;351:714–718. doi: 10.1016/S0140-6736(97)06402-7.
65. Nakae I, Mitsunami K, Omura T, et al. Proton magnetic resonance spectroscopy can detect creatine depletion associated with the progression of heart failure in cardiomyopathy. *J Am Coll Cardiol* 2003;42:1587–1593.
66. Santulli G. Epidemiology of cardiovascular disease in the 21st century: updated numbers and updated facts. *JCvD* 2013;1:1–2.
67. Pagidipati NJ, Gaziano TA. Estimating Deaths From Cardiovascular Disease: A Review of Global Methodologies of Mortality Measurement. *Circulation* 2013;127:749–756. doi: 10.1161/CIRCULATIONAHA.112.128413.
68. Heidenreich PA, Trogon JG, Khavjou OA, et al. Forecasting the future of cardiovascular disease in the United States: a policy statement from the American Heart Association. *Circulation* 2011;123:933–944. doi: 10.1161/CIR.0b013e31820a55f5.
69. Starling RC, Hammer DF, Altschuld RA. Human myocardial ATP content and in vivo contractile function. *Mol Cell Biochem* 1998;180:171–177. doi: 10.1023/A:1006876031121.
70. Wyss M, Kaddurah-Daouk R. Creatine and Creatinine Metabolism. *Physiological Reviews* 2000;80:1107–1213.
71. Neubauer S. The Failing Heart — An Engine Out of Fuel. *N Engl J Med* 2007;356:1140–1151. doi: 10.1056/NEJMr063052.
72. Essop MF, Opie LH. Metabolic therapy for heart failure. *Eur Heart J* 2004;25:1765–1768. doi: 10.1016/j.ehj.2004.08.019.
73. Lopaschuk GD, Rebeyka IM, Allard MF. Metabolic Modulation A Means to Mend a Broken Heart. *Circulation* 2002;105:140–142. doi: 10.1161/hc0202.102238.
74. Morrow DA, Givertz MM. Modulation of Myocardial Energetics Emerging Evidence for a Therapeutic Target in Cardiovascular Disease. *Circulation* 2005;112:3218–3221. doi: 10.1161/CIRCULATIONAHA.105.581819.
75. Weiss RG, Maslov M. Normal myocardial metabolism: fueling cardiac contraction. *Adv Stud Med* 2004.
76. Nascimben L, Ingwall JS, Pauletto P, Friedrich J, Gwathmey JK, Saks V, Pessina AC, Allen PD. Creatine Kinase System in Failing and Nonfailing Human Myocardium. *Circulation* 1996;94:1894–1901. doi: 10.1161/01.CIR.94.8.1894.

77. Ingwall JS, Atkinson DE, Clarke K, Fетters JK. Energetic correlates of cardiac failure: Changes in the creatine kinase system in the failing myocardium. *Eur Heart J* 1990;11:108–115. doi: 10.1093/eurheartj/11.suppl_B.108.
78. Ventura Clapier R, Garnier A, Veksler V. Energy metabolism in heart failure. *The Journal of Physiology* 2004;555:1–13. doi: 10.1113/jphysiol.2003.055095.
79. Bottomley PA, Weiss RG. Non-invasive magnetic-resonance detection of creatine depletion in non-viable infarcted myocardium. *The Lancet* 1998;351:714–718. doi: 10.1016/S0140-6736(97)06402-7.
80. Neubauer S, Horn M, Cramer M, et al. Myocardial Phosphocreatine-to-ATP Ratio Is a Predictor of Mortality in Patients With Dilated Cardiomyopathy. *Circulation* 1997;96:2190–2196. doi: 10.1161/01.CIR.96.7.2190.
81. Haris M, Nanga RPR, Singh A, Cai K, Kogan F, Hariharan H, Reddy R. Exchange rates of creatine kinase metabolites: feasibility of imaging creatine by chemical exchange saturation transfer MRI. *NMR Biomed* 2012;25:1305–1309. doi: 10.1002/nbm.2792.
82. Vandsburger M, Vandoorne K, Oren R, Leftin A, Mpofu S, Delli Castelli D, Aime S, Neeman M. Cardio-chemical exchange saturation transfer magnetic resonance imaging reveals molecular signatures of endogenous fibrosis and exogenous contrast media. *Circ Cardiovasc Imaging* 2015;8:e002180. doi: 10.1161/CIRCIMAGING.114.002180.
83. Pumphrey A, Yang Z, Ye S, et al. Advanced cardiac chemical exchange saturation transfer (cardioCEST) MRI for in vivo cell tracking and metabolic imaging. *NMR Biomed* 2016;29:74–83. doi: 10.1002/nbm.3451.
84. Pumphrey AL, Ye S, Yang Z, Simkin J, Gensel JC, Abdel-Latif A, Vandsburger MH. Cardiac Chemical Exchange Saturation Transfer MR Imaging Tracking of Cell Survival or Rejection in Mouse Models of Cell Therapy. *Radiology* 2016;152766. doi: 10.1148/radiol.2016152766.
85. Sanbe A, Tanonaka K, Hanaoka Y, Katoh T, Takeo S. Regional energy metabolism of failing hearts following myocardial infarction. *J. Mol. Cell. Cardiol.* 1993;25:995–1013. doi: 10.1006/jmcc.1993.1113.
86. Lee S-T, White AJ, Matsushita S, et al. Intramyocardial injection of autologous cardiospheres or cardiosphere-derived cells preserves function and minimizes adverse ventricular remodeling in pigs with heart failure post-myocardial infarction. *J Am Coll Cardiol* 2011;57:455–465. doi: 10.1016/j.jacc.2010.07.049.
87. Myronenko A, Xubo Song. Intensity-Based Image Registration by Minimizing Residual Complexity. *Medical Imaging, IEEE Transactions on* 2010;29:1882–1891. doi: 10.1109/TMI.2010.2053043.
88. Zaiss M, Schmitt B, Bachert P. Quantitative separation of CEST effect from magnetization transfer and spillover effects by Lorentzian-line-fit analysis of z-spectra. *J Magn Reson* 2011;211:149–155. doi: 10.1016/j.jmr.2011.05.001.
89. Bottomley PA, Lee Y, Weiss RG. Total creatine in muscle: imaging and quantification with proton MR spectroscopy. *Radiology* 1997;204:403–410. doi: 10.1148/radiology.204.2.9240527.

90. Cerqueira MD, Weissman NJ, Dilsizian V, Jacobs AK. Standardized myocardial segmentation and nomenclature for tomographic imaging of the heart a statement for healthcare professionals from the cardiac imaging Committee of the Council on Clinical Cardiology of the American Heart Association. *Circulation* 2002;105:539–542. doi: 10.1161/hc0402.102975.
91. Buchthal SD, Hollander den JA, Merz CN, Rogers WJ, Pepine CJ, Reichek N, Sharaf BL, Reis S, Kelsey SF, Pohost GM. Abnormal myocardial phosphorus-31 nuclear magnetic resonance spectroscopy in women with chest pain but normal coronary angiograms. *N Engl J Med* 2000;342:829–835. doi: 10.1056/NEJM200003233421201.
92. Knox J, Orchowski J, Scher DL, Owens BD, Burks R, Belmont PJ. The incidence of low back pain in active duty United States military service members. *Spine* 2011;36:1492–1500. doi: 10.1097/BRS.0b013e3181f40ddd.
93. GBD 2015 Risk Factors Collaborators. Global, regional, and national comparative risk assessment of 79 behavioural, environmental and occupational, and metabolic risks or clusters of risks, 1990-2015: a systematic analysis for the Global Burden of Disease Study 2015. *Lancet* 2016;388:1659–1724. doi: 10.1016/S0140-6736(16)31679-8.
94. Dagenais S, Caro J, Haldeman S. A systematic review of low back pain cost of illness studies in the United States and internationally. *The Spine Journal* 2008;8:8–20. doi: 10.1016/j.spinee.2007.10.005.
95. Weisman MH, Witter JP, Reveille JD. The prevalence of inflammatory back pain: population-based estimates from the US National Health and Nutrition Examination Survey, 2009–10. *Annals of the Rheumatic Diseases* 2013;72:369–373. doi: 10.1136/annrheumdis-2012-201403.
96. Freemont AJ. The cellular pathobiology of the degenerate intervertebral disc and discogenic back pain. *Rheumatology (Oxford)* 2009;48:5–10. doi: 10.1093/rheumatology/ken396.
97. Carragee EJ, Don AS, Hurwitz EL, Cuellar JM, Carrino JA, Carrino J, Herzog R. 2009 ISSLS Prize Winner: Does discography cause accelerated progression of degeneration changes in the lumbar disc: a ten-year matched cohort study. *Spine* 2009;34:2338–2345. doi: 10.1097/BRS.0b013e3181ab5432.
98. Liang C-Z, Li H, Tao Y-Q, Zhou X-P, Yang Z-R, Li F-C, Chen Q-X. The relationship between low pH in intervertebral discs and low back pain: a systematic review. *Arch Med Sci* 2012;8:952–956. doi: 10.5114/aoms.2012.32401.
99. Liang C, Li H, Tao Y, Shen C, Li F, Shi Z, Han B, Chen Q. New hypothesis of chronic back pain: low pH promotes nerve ingrowth into damaged intervertebral disks. *Acta Anaesthesiol Scand* 2013;57:271–277. doi: 10.1111/j.1399-6576.2012.02670.x.
100. Keshari KR, Lotz JC, Link TM, Hu S, Majumdar S, Kurhanewicz J. Lactic Acid and Proteoglycans as Metabolic Markers for Discogenic Back Pain. *Spine* 2008;33:312–317. doi: 10.1097/BRS.0b013e31816201c3.
101. Sun PZ, Murata Y, Lu J, Wang X, Lo EH, Sorensen AG. Relaxation-compensated fast multislice amide proton transfer (APT) imaging of acute ischemic stroke. *Magn Reson Med* 2008;59:1175–1182. doi: 10.1002/mrm.21591.

102. Sun PZ, Zhou J, Sun W, Huang J, van Zijl PCM. Detection of the ischemic penumbra using pH-weighted MRI. *J Cereb Blood Flow Metab* 2007;27:1129–1136. doi: 10.1038/sj.jcbfm.9600424.
103. Zhou J, van Zijl PCM. Defining an Acidosis-Based Ischemic Penumbra from pH-Weighted MRI. *Transl Stroke Res* 2011;3:76–83. doi: 10.1007/s12975-011-0110-4.
104. Sun PZ, Wang Y, Dai Z, Xiao G, Wu R. Quantitative chemical exchange saturation transfer (qCEST) MRI - RF spillover effect-corrected omega plot for simultaneous determination of labile proton fraction ratio and exchange rate. *Contrast Media Mol Imaging* 2014;9:268–275. doi: 10.1002/cmml.1569.
105. Wu R, Longo DL, Aime S, Sun PZ. Quantitative description of radiofrequency (RF) power-based ratiometric chemical exchange saturation transfer (CEST) pH imaging. *NMR Biomed* 2015;28:555–565. doi: 10.1002/nbm.3284.
106. Meissner J-E, Goerke S, Rerich E, Klika KD, Radbruch A, Ladd ME, Bachert P, Zaiss M. Quantitative pulsed CEST-MRI using Ω -plots. *NMR Biomed* 2015;28:1196–1208. doi: 10.1002/nbm.3362.
107. Sun PZ, Xiao G, Zhou IY, Guo Y, Wu R. A method for accurate pH mapping with chemical exchange saturation transfer (CEST) MRI. *Contrast Media Mol Imaging* 2015. doi: 10.1002/cmml.1680.
108. Dixon WT, Ren J, Lubag AJM, Ratnakar J, Vinogradov E, Hancu I, Lenkinski RE, Sherry AD. A concentration-independent method to measure exchange rates in PARACEST agents. *Magn Reson Med* 2010;63:625–632. doi: 10.1002/mrm.22242.
109. Lee J-S, Xia D, Jerschow A, Regatte RR. In vitro study of endogenous CEST agents at 3 T and 7 T. *Contrast Media Mol Imaging* 2016;11:4–14. doi: 10.1002/cmml.1652.
110. Kim M, Gillen J, Landman BA, Zhou J, van Zijl PCM. Water saturation shift referencing (WASSR) for chemical exchange saturation transfer (CEST) experiments. *Magn Reson Med* 2009;61:1441–1450. doi: 10.1002/mrm.21873.
111. Nachemson A. Intradiscal measurements of pH in patients with lumbar rhizopathies. *Acta Orthop Scand* 1969. doi: 10.3109/17453676908989482.
112. Liu Q, Jin N, Fan Z, Natsuaki Y, Tawackoli W, Pelled G, Bae H, Gazit D, Li D. Reliable chemical exchange saturation transfer imaging of human lumbar intervertebral discs using reduced- field- of- view turbo spin echo at 3.0 T. *NMR Biomed* 2013;26:1672–1679. doi: 10.1002/nbm.3001.
113. Englander SW, Downer NW, Teitelbaum H. Hydrogen exchange. *Annu Rev Biochem* 1972;41:903–924. doi: 10.1146/annurev.bi.41.070172.004351.
114. Antoniou J, Pike GB, Steffen T, Baramki H, Poole AR, Aebi M, Alini M. Quantitative magnetic resonance imaging in the assessment of degenerative disc disease. *Magn Reson Med* 1998;40:900–907. doi: 10.1002/mrm.1910400616.
115. Heo HY, Zhang Y, Lee DH, Jiang S, Zhao X, Zhou J. Accelerating chemical exchange saturation transfer (CEST) MRI by combining compressed sensing and sensitivity encoding

techniques. *Magn Reson Med* 2016;n/a–n/a. doi: 10.1002/mrm.26141.

116. An HS, Anderson PA, Haughton VM, Iatridis JC. Introduction: disc degeneration: summary. *Spine* 2004;29:2677–2678. doi: 10.1097/01.brs.0000147573.88916.c6.

117. Takashima H, Takebayashi T, Yoshimoto M, Terashima Y, Tsuda H, Ida K, Yamashita T. Correlation between T2 relaxation time and intervertebral disk degeneration. *Skeletal Radiol* 2012;41:163–167. doi: 10.1007/s00256-011-1144-0.

118. Wang Y-XJ, Zhao F, Griffith JF, Mok GSP, Leung JCS, Ahuja AT, Yuan J. T1rho and T2 relaxation times for lumbar disc degeneration: an in vivo comparative study at 3.0-Tesla MRI. *Eur Radiol* 2013;23:228–234. doi: 10.1007/s00330-012-2591-2.

119. Kim KS, Yoon ST, Li J, Park JS, Hutton WC. Disc Degeneration in the Rabbit: A Biochemical and Radiological Comparison Between Four Disc Injury Models. *Spine* 2005;30:33. doi: 10.1097/01.brs.0000149191.02304.9b.

120. Lefevre-Colau M-M, Fayad F, Rannou F, Fermanian J, Coriat F, Mace Y, Revel M, Poiraudreau S. Frequency and Interrelations of Risk Factors for Chronic Low Back Pain in a Primary Care Setting. *PLOS ONE* 2009;4:e4874. doi: 10.1371/journal.pone.0004874.

121. Asıcıoglu O, Güngördük K, Yildirim G, Aslan H, Günay T. Maternal and perinatal outcomes of eclampsia with and without HELLP syndrome in a teaching hospital in western Turkey. *Journal of Obstetrics and Gynaecology* 2014. doi: 10.3109/01443615.2014.881791.

122. Majumdar S, Link TM, Steinbach LS, Hu S, Kurhanewicz J. Diagnostic Tools and Imaging Methods in Intervertebral Disk Degeneration. *Orthopedic Clinics of North America* 2011;42:501–511. doi: 10.1016/j.ocl.2011.07.007.

123. Kang CH, Kim YH, Lee S-H, Derby R, Kim JH, Chung KB, Sung DJ. Can magnetic resonance imaging accurately predict concordant pain provocation during provocative disc injection? *Skeletal Radiol* 2009;38:877–885. doi: 10.1007/s00256-009-0709-7.

124. Raj PP. Intervertebral Disc: Anatomy- Physiology- Pathophysiology- Treatment. *Pain Practice* 2008;8:18–44. doi: 10.1111/j.1533-2500.2007.00171.x.

125. Menkin V. Biochemical Mechanisms in Inflammation. *British Medical Journal* 1960;1:1521. doi: 10.1002/nbm.1742.

126. Urban JPG, Smith S, Fairbank JCT. Nutrition of the Intervertebral Disc. *Spine* 2004;29:2700. doi: 10.1097/01.brs.0000146499.97948.52.

127. Ichimura K, Tsuji H, Matsui H, Makiyama N. Cell Culture of the Intervertebral Disc of Rats: Factors Influencing Culture, Proteoglycan, Collagen, and Deoxyribonucleic Acid Synthesis. *Clinical Spine Surgery* 1991;4:428.

128. Zhou Z, Bez M, Tawackoli W, et al. Quantitative chemical exchange saturation transfer MRI of intervertebral disc in a porcine model. *Magn Reson Med* 2016;76:1677–1683. doi: 10.1002/mrm.26457.

129. Mizrahi O, Sheyn D, Tawackoli W, Ben-David S, Su S, Li N, Oh A, Bae H, Gazit D, Gazit Z.

Nucleus pulposus degeneration alters properties of resident progenitor cells. *The Spine Journal* 2013;13:803–814. doi: 10.1016/j.spinee.2013.02.065.

130. Sheyn D, Yakubovich DC, Kallai I, et al. PTH Promotes Allograft Integration in a Calvarial Bone Defect. *Molecular ...* 2013. doi: 10.1021/mp400292p.

131. Trattnig S, Stelzeneder D, Goed S, Reissegger M, Mamisch TC, Paternostro-Sluga T, Weber M, Szomolanyi P, Welsch GH. Lumbar intervertebral disc abnormalities: comparison of quantitative T2 mapping with conventional MR at 3.0 T. *Eur Radiol* 2010;20:2715–2722. doi: 10.1007/s00330-010-1843-2.

132. Auerbach JD, Johannessen W, Borthakur A, Wheaton AJ, Dolinskas CA, Balderston RA, Reddy R, Elliott DM. In vivo quantification of human lumbar disc degeneration using T(1rho)-weighted magnetic resonance imaging. *Eur Spine J* 2006;15 Suppl 3:S338–44. doi: 10.1007/s00586-006-0083-2.

133. Zhao C-Q, Wang L-M, Jiang L-S, Dai L-Y. The cell biology of intervertebral disc aging and degeneration. *Ageing Res. Rev.* 2007;6:247–261. doi: 10.1016/j.arr.2007.08.001.

134. Chatani K, Kusaka Y, Mifune T, Nishikawa H. Topographic Differences of ¹H-NMR Relaxation Times (T13 T2) in the Normal Intervertebral Disc and Its Relationship to Water Content. *Spine* 1993;18:2271.

135. Chiu EJ, Newitt DC, Segal MR, Hu SS, Lotz JC, Majumdar S. Magnetic Resonance Imaging Measurement of Relaxation and Water Diffusion in the Human Lumbar Intervertebral Disc Under Compression In Vitro. *Spine* 2001;26:E437.

136. Boos N, Dreier D, Hilfiker E, Schade V, Kreis R, Hora J, Aebi M, Boesch C. Tissue characterization of symptomatic and asymptomatic disc herniations by quantitative magnetic resonance imaging. *Journal of Orthopaedic Research* 1997;15:141–149. doi: 10.1002/jor.1100150121.

137. Blumenkrantz G, Zuo J, Li X, Kornak J, Link TM, Majumdar S. In vivo 3.0- tesla magnetic resonance T1p and T2 relaxation mapping in subjects with intervertebral disc degeneration and clinical symptoms. *Magn Reson Med* 2010;63:1193–1200. doi: 10.1002/mrm.22362.

138. Borthakur A, Maurer PM, Fenty M, Wang C, Berger R, Yoder J, Balderston RA, Elliott DM. T1p magnetic resonance imaging and discography pressure as novel biomarkers for disc degeneration and low back pain. *Spine* 2011;36:2190–2196. doi: 10.1097/BRS.0b013e31820287bf.

139. Wada T, Togao O, Tokunaga C, Funatsu R, Yamashita Y, Kobayashi K, Nakamura Y, Honda H. Glycosaminoglycan chemical exchange saturation transfer in human lumbar intervertebral discs: Effect of saturation pulse and relationship with low back pain. *Journal of Magnetic Resonance Imaging* 2017;45:863–871. doi: 10.1002/jmri.25397.

140. Richardson SM, Purmessur D, Baird P, Ben Probyn, Freemont AJ, Hoyland JA. Degenerate Human Nucleus Pulposus Cells Promote Neurite Outgrowth in Neural Cells. *PLOS ONE* 2012;7:e47735. doi: 10.1371/journal.pone.0047735.

141. Purmessur D, Freemont AJ, Hoyland JA. Expression and regulation of neurotrophins in the

nondegenerate and degenerate human intervertebral disc. *Arthritis Res. Ther.* 2008;10:R99. doi: 10.1186/ar2487.

142. Navone SE, Marfia G, Canzi L, Ciusani E, Canazza A, Visintini S, Campanella R, Parati EA. Expression of neural and neurotrophic markers in nucleus pulposus cells isolated from degenerated intervertebral disc. *Journal of Orthopaedic Research* 2012;30:1470–1477. doi: 10.1002/jor.22098.

143. Freemont AJ, Peacock TE, Goupille P, Hoyland JA, O'Brien J, Jayson MI. Nerve ingrowth into diseased intervertebral disc in chronic back pain. *The Lancet* 1997;350:178–181.

144. Coppes MH, Marani E, Thomeer RT, Oudega M, Groen GJ. Innervation of annulus fibrosis in low back pain. *The Lancet* 1990;336:189–190.

145. Peng B, Wu W, Hou S, Li P, Zhang C, Yang Y. The pathogenesis of discogenic low back pain. *Bone & Joint Journal* 2005;87-B:62–67. doi: 10.1302/0301-620X.87B1.15708.

146. Gilbert HTJ, Hodson N, Baird P, Richardson SM, Hoyland JA. Acidic pH promotes intervertebral disc degeneration: Acid-sensing ion channel -3 as a potential therapeutic target. *Scientific Reports* 2016;6:37360. doi: 10.1038/srep37360.

147. Ohtori S, Inoue G, Koshi T, Ito T, Doya H, Saito T, Moriya H, Takahashi K. Up-Regulation of Acid-Sensing Ion Channel 3 in Dorsal Root Ganglion Neurons Following Application of Nucleus Pulposus on Nerve Root in Rats. *Spine* 2006;31:2048. doi: 10.1097/01.brs.0000231756.56230.13.

148. Cuesta A, del Valle ME, García-Suárez O, et al. Acid-sensing ion channels in healthy and degenerated human intervertebral disc. *Connective Tissue Research* 2014. doi: 10.3109/03008207.2014.884083.

149. Uchiyama Y, Cheng CC, Danielson KG, Mochida J, Albert TJ, Shapiro IM, Risbud MV. Expression of Acid- Sensing Ion Channel 3 (ASIC3) in Nucleus Pulposus Cells of the Intervertebral Disc Is Regulated by p75NTR and ERK Signaling. *Journal of Bone and Mineral Research* 2007;22:1996–2006. doi: 10.1359/jbmr.070805.

150. Liu J, Tao H, Wang H, et al. Biological Behavior of Human Nucleus Pulposus Mesenchymal Stem Cells in Response to Changes in the Acidic Environment During Intervertebral Disc Degeneration. *Stem Cells Dev.* 2017:scd.2016.0314. doi: 10.1089/scd.2016.0314.

151. Gruber HE, Hoelscher GL, Ingram JA, Hanley EN. Genome-wide analysis of pain-, nerve- and neurotrophin -related gene expression in the degenerating human annulus. *Molecular Pain* 2012 8:1 2012;8:63. doi: 10.1186/1744-8069-8-63.

152. Dray A, Perkins M. Bradykinin and inflammatory pain. *Trends in Neurosciences* 1993;16:99–104. doi: 10.1016/0166-2236(93)90133-7.

153. Donnerer J, Schuligoi R, Stein C. Increased content and transport of substance P and calcitonin gene-related peptide in sensory nerves innervating inflamed tissue: Evidence for a regulatory function of nerve growth factor in vivo. *Neuroscience* 1992;49:693–698. doi: 10.1016/0306-4522(92)90237-V.

154. Andersen S, Skorpen F. Variation in the COMT gene: implications for pain perception and

pain treatment. *Pharmacogenomics* 2009;10:669–684. doi: 10.2217/pgs.09.13.

155. Orita S, Ohtori S, Nagata M, et al. Inhibiting nerve growth factor or its receptors downregulates calcitonin gene-related peptide expression in rat lumbar dorsal root ganglia innervating injured intervertebral discs. *Journal of Orthopaedic Research* 2010;28:1614–1620. doi: 10.1002/jor.21170.

156. Zuo J, Saadat E, Romero A, Loo K, Li X, Link TM, Kurhanewicz J, Majumdar S. Assessment of intervertebral disc degeneration with magnetic resonance single-voxel spectroscopy. *Magn Reson Med* 2009;62:1140–1146. doi: 10.1002/mrm.22093.

157. Zuo J, Joseph GB, Li X, Link TM, Hu SS, Berven SH, Kurhanewicz J, Majumdar S. In vivo intervertebral disc characterization using magnetic resonance spectroscopy and T1 ρ imaging: association with discography and Oswestry Disability Index and Short Form-36 Health Survey. *Spine* 2012;37:214–221. doi: 10.1097/BRS.0b013e3182294a63.

158. Sheth VR, Li Y, Chen LQ, Howison CM, Flask CA, Pagel MD. Measuring in vivo tumor pH with CEST-FISP MRI. *Magn Reson Med* 2012;67:760–768. doi: 10.1002/mrm.23038.

159. Chen LQ, Howison CM, Jeffery JJ, Robey IF, Kuo PH, Pagel MD. Evaluations of extracellular pH within in vivo tumors using acidoCEST MRI. *Magn Reson Med* 2014;72:1408–1417. doi: 10.1002/mrm.25053.

160. Chen LQ, Randtke EA, Jones KM, Moon BF, Howison CM, Pagel MD. Evaluations of Tumor Acidosis Within In Vivo Tumor Models Using Parametric Maps Generated with AcidoCEST MRI. *Mol Imaging Biol* 2015;17:488–496. doi: 10.1007/s11307-014-0816-2.

161. Rerich E, Zaiss M, Korzowski A, Ladd ME, Bachert P. Relaxation-compensated CEST-MRI at 7 T for mapping of creatine content and pH – preliminary application in human muscle tissue in vivo. *NMR Biomed* 2015;28:1402–1412. doi: 10.1002/nbm.3367.

162. Xu J, Zaiss M, Zu Z, Li H, Xie J, Gochberg DF, Bachert P, Gore JC. On the origins of chemical exchange saturation transfer (CEST) contrast in tumors at 9.4 T. *NMR Biomed* 2014;27:406–416. doi: 10.1002/nbm.3075.

163. Sun PZ, Longo DL, Hu W, Xiao G, Wu R. Quantification of iopamidol multi-site chemical exchange properties for ratiometric chemical exchange saturation transfer (CEST) imaging of pH. *Phys Med Biol* 2014;59:4493. doi: 10.1088/0031-9155/59/16/4493.

164. Zu Z, Janve VA, Li K, Does MD, Gore JC, Gochberg DF. Multi-angle ratiometric approach to measure chemical exchange in amide proton transfer imaging. *Magn Reson Med* 2012;68:711–719. doi: 10.1002/mrm.23276.

165. Ma D, Gulani V, Seiberlich N, Liu K, Sunshine JL, Duerk JL, Griswold MA. Magnetic resonance fingerprinting. *Nature* 2013;495:187–192. doi: 10.1038/nature11971.

166. Goerke S, Zaiss M, Bachert P. Characterization of creatine guanidinium proton exchange by water-exchange (WEX) spectroscopy for absolute-pH CEST imaging in vitro. *NMR Biomed* 2014;27:507–518. doi: 10.1002/nbm.3086.

167. Song X, Gilad AA, Joel S, et al. CEST phase mapping using a length and offset varied

saturation (LOVARS) scheme. *Magn Reson Med* 2012;68:1074–1086. doi: 10.1002/mrm.23312.

168. Song X, Xu J, Xia S, Yadav NN, Lal B, Laterra J, Bulte JWM, van Zijl PCM, McMahon MT. Multi-echo Length and Offset VARied Saturation (MeLOVARS) method for improved CEST imaging. *Magn Reson Med* 2015;73:488–496. doi: 10.1002/mrm.25567.

169. Geades N, Hunt BAE, Shah SM, Peters A, Mougou OE, Gowland PA. Quantitative analysis of the z-spectrum using a numerically simulated look-up table: Application to the healthy human brain at 7T. *Magn Reson Med* 2016. doi: 10.1002/mrm.26459.

170. Heo HY, Zhang Y, Lee DH, Hong X, Zhou J. Quantitative assessment of amide proton transfer (APT) and nuclear overhauser enhancement (NOE) imaging with extrapolated semi-solid magnetization transfer reference (EMR) signals: Application to a rat glioma model at 4.7 Tesla. *Magn Reson Med* 2016;75:137–149. doi: 10.1002/mrm.25581.

171. Jin T, Kim S-G. Advantages of chemical exchange-sensitive spin-lock (CESL) over chemical exchange saturation transfer (CEST) for hydroxyl- and amine-water proton exchange studies. *NMR Biomed* 2014;27:1313–1324. doi: 10.1002/nbm.3191.

172. Jin T, Autio J, Obata T, Kim S-G. Spin-locking versus chemical exchange saturation transfer MRI for investigating chemical exchange process between water and labile metabolite protons. *Magn Reson Med* 2011;65:1448–1460. doi: 10.1002/mrm.22721.

173. Yuan J, Zhou J, Ahuja AT, Wang Y-XJ. MR chemical exchange imaging with spin-lock technique (CESL): a theoretical analysis of the Z-spectrum using a two-pool R1ρ relaxation model beyond the fast-exchange limit. *Phys Med Biol* 2012;57:8185–8200. doi: 10.1088/0031-9155/57/24/8185.

174. Zhang S, Liu Z, Grant A, Keupp J, Lenkinski RE, Vinogradov E. Balanced Steady-State Free Precession (bSSFP) from an effective field perspective: Application to the detection of chemical exchange (bSSFPX). *J Magn Reson* 2017;275:55–67. doi: 10.1016/j.jmr.2016.12.002.

175. Henkelman RM, Huang X, Xiang QS, Stanisz GJ, Swanson SD, Bronskill MJ. Quantitative interpretation of magnetization transfer. *Magn Reson Med* 1993;29:759–766. doi: 10.1002/mrm.1910290607.

176. Jones CK, Polders D, Hua J, Zhu H, Hoogduin HJ, Zhou J, Luijten P, van Zijl PCM. In vivo three-dimensional whole-brain pulsed steady-state chemical exchange saturation transfer at 7 T. *Magn Reson Med* 2012;67:1579–1589. doi: 10.1002/mrm.23141.